5-2024

Using Strainmeters to Characterize Enhanced Geothermal Systems

Clem Laffaille
claffai@g.clemson.edu

Using Strainmeters to Characterize Enhanced Geothermal Systems

A Thesis Presented to
The Graduate School of
Clemson University

In Partial Fulfillment
Of the Requirements for the Degree
Master of Science
Hydrogeology

By

Clemence Laffaille

May 2024

Accepted by:
Dr. Lawrence Murdoch, Committee Chair
Dr. Scott DeWolf
Dr. Ronald Falta

ABSTRACT

Enhanced Geothermal Systems (EGS) are attractive because they can generate electrical power without releasing carbon dioxide. However, they require well stimulation methods that are effective in hot, low permeability rock to increase the water circulation and heat extraction to rates that are fast enough to economically generate electric power. Monitoring and interpreting the deformation associated with hydraulic fracturing well stimulations and the heat recovery operations that follow promise to generate insights that can improve performance of EGS. Strainmeters have been used to characterize deformation during hydraulic fracturing and water pumping and recovery from aquifers, but temperatures at depth in geothermal systems are hot enough to damage current strainmeter technology. Furthermore, many geothermal sites are overlain by alluvium, which is poorly suited to high resolution strainmeters designed to be deployed in rock.

The objectives of this study are to evaluate the feasibility of developing strainmeters that can be deployed either at elevated temperatures, or in unconsolidated materials in order to improve applications of strain data in geothermal settings. The approach has been to conduct simulations to evaluate the expected strain signals and design and build prototypes that can measure those signals. Two strainmeter designs were then tested under controlled conditions in the lab and at shallow depths in the field. One of them is a *split-sleeve* design intended to be deployed around a casing during well completion, whereas the other design, called *direct-push* strainmeter, is a cylindrical design intended to be deployed by directly pushing into the ground. The split-sleeve strainmeter was fabricated from high-temperature composite material and then clamped onto a steel pipe representing a well casing. The strainmeter and pipe were heated to temperatures of 200°C and 230ºC while repetitive loadings were applied for two months. Four

strain sensors, three oriented axially and one oriented circumferentially, measured strain during bending of the pipe. Two direct-push strainmeters were cast from urethane resin to evaluate the effects of different internal configurations on their apparent elastic modulus. The direct-push strainmeters measured strain with Fiber Bragg Gratings (FBGs), and one of them included both FBGs and a Mach Zehnder interferometer. These instruments were tested in a laboratory pressure chamber to evaluate how well they could match the elastic modulus of soil, and additional tests were conducted to evaluate responses from different optical fiber strain sensors. A stainless-steel tensor strainmeter with four strain sensors was deployed by direct push into saprolite to evaluate how this deployment method affected strainmeter performance during well testing.

Results from the lab experiments show that the split-sleeve strainmeter was able to measure strains caused by transverse loads applied to a steel pipe while being heated at 200^{o}C to 230^{o}C for several months. The relative magnitudes of the measured strains are similar to the results from numerical simulations, which provides an independent validation of the measurements. These findings indicate that the split-sleeve design could be a viable approach for deploying strain or seismic sensors in geothermal reservoirs for extended periods.

Lab experiments with the direct-push strainmeter demonstrate that strains measured by FBGs correlate with optical phase data from a Mach-Zehnder interferometer. The relation between the two datasets demonstrates a new calibration method for the Mach-Zehnder interferometer. The lab data also show that the internal bonding of a threaded rod can increase the apparent elastic modulus of the urethane cylinder by more than two orders of magnitude, from 66 MPa to 9800 MPa. This large increase in apparent modulus caused by an embedded rod is explained using simulations where the urethane is assumed to have a Poisson's ratio of

ν=0.499. The tensor strainmeter deployed in the field by direct push was used to measure strain during six constant-rate pumping tests. The time series from the four channels are distinct from each other and are repeatable to within less than 20%. The vertical strain is consistently tensile during pumping, whereas the horizontal strains range from tensile to compressive—strains in one horizontal direction are consistently compressive during pumping, whereas the strains measured by a sensor at 90^o are consistently tensile, and strains measured by a sensor at 45^o are tensile at the start of pumping but then decrease and become compressive with time. These results are consistent with poroelastic simulations, and they were used to correctly estimate the permeability of the formation and the orientation of the instrument. This confirms that a strainmeter deployed by direct push into soft geologic materials can generate data during pumping tests that can be inverted to provide useful information.

ACKNOWLEDGEMENTS

I would like to thank my advisor, Dr. Murdoch, for his time and allowing me to be part of the FORGE project from which I learned a lot.

My thanks also go to Dr. Scott Dewolf who taught me a lot about optical fibers and how to work with them and Dr. Brady Flinchum who helped me write a code to analyze my data.

I'd like to thank the Department of Energy for providing the funding for the Utah FORGE Project DE-EE0007080.

I also would like to express my gratitude to my friends, Josh Parrish, and Max Gordon, who worked with me on this project. With their help, we were able to keep the project moving forward and achieve some important milestones.

Finally, I want to thank my friends and family who supported me from the moment I started at Clemson to now. Graduate school is not easy, and those people were there to cheer me up and encourage me whenever I needed it.

TABLE OF CONTENT

LIST OF TABLES/FIGURES

Chapter One: INTRODUCTION

The atmospheric CO_2 crisis is shaping the world we live in today. The Intergovernmental Panel on Climate Change (IPCC) predicts that the use of fossil fuels will need to be drastically reduced in the next few decades in order to limit CO_2-induced global warming to acceptable levels (<1.5 ˚C increase) (IPPC, 2014).

Efforts to tackle this crisis include the development of renewable energy technologies using wind, water, solar and geothermal, which can provide electric power without emitting CO_2. Hydroelectric plants have been used for many decades, and recent activities have focused on developing wind turbines and solar panels for generating electricity (IEA, 2023). Low temperature geothermal resources are widely used for heating and cooling buildings, but high temperatures ranging from 100° to 350°C (Breede et al, 2013) are required to generate electricity. Heat energy is typically extracted by circulating water between wells in hot rocks, but the permeability of most hot rocks is too low to circulate water fast enough to generate much power (Olasolo et al., 2016). A few geothermal facilities are currently able to access rocks that are both hot and permeable enough to extract thermal energy at economic rates, but these conditions rarely occur naturally. This has motivated the development of techniques to enhance the thermal power that can be recovered from geothermal resources (Tester et al., 2007; Norbeck et al., 2023).

GEOTHERMAL ENERGY: EGS DEVELOPMENT

Geothermal energy represented only 3.5% of the energy used in the United States in 2021 in all sectors (industrial, transport, residential, commercial) for heating system and electricity (IEA Geothermal, 2022). Most applications of geothermal energy use subsurface low

temperature resources for heating. Efforts to use more of the Earth's natural heat are underway with the development of innovative geothermal power plants to achieve 8.5% of energy production with geothermal resources by 2050 (IEA Geothermal, 2022). Several methods exist to recover underground heat for geothermal technologies.

Geothermal heat pump and direct district heating methods are subsurface heat collection systems using borehole heat exchangers (Galantino, 2020). Water, or another working fluid, is pumped in pipes buried in the subsurface in contact with the soil or bedrock. The pipes transfer heat between the working fluid and the rock. It flows back to a heat exchanger that can extract the heat from the water to produce hot or cold air (Bourne-Webb et al., 2016). Boreholes heat exchangers are installed under a building directly and require subsurface temperatures of 20ºC or less while a direct district heating system delivers thermal energy to several buildings over a larger area and require temperatures between 40 and 80ºC (Gallup, 2009; Galantino, 2020).

Power plants that utilize liquid-dominated geothermal reservoirs produce electricity by tapping thermal energy of the bedrock between 80 and 130ºC for a binary cycle power plant and between 130 and 200ºC for a flash steam power plant. Binary cycle power plants inject a water at a sufficient flow rate-to collect heat from permeable bedrock (Tester et al., 2006). The warm water is pumped out and injected into a heat exchanger that is used to vaporize a low-boiling point fluid such as isobutane, pentane, n-isobutane and n-isopentane (Ziółkowski et al., 2021). The expanding vapor turns a turbine, which is connected to a generator to convert the mechanical energy into electricity. Flash-steam power plants use the hot water produced from the geothermal reservoir to generate the vapor that turns a turbine, thereby avoiding the use of a low-boiling point fluid (Ziółkowski et al., 2021). Existing technologies make it possible to extract heat at depths between 3km and 8 km, typically in areas where igneous intrusions have been emplaced

relatively recently (Tester et al., 2006). The places where geothermal heat is already exploited to generate electricity for commercial purposes have rocks that are permeable enough to sustain flow rates between wells that are greater than 50 L/s (Jung, 2013).

Power plants that utilize vapor-dominated geothermal reservoirs use wells to collect steam from bedrock reaching temperatures greater than 200 ºC. A valve in the production well limits the inflow and outflow of steam to maintain a reservoir pressure lower than the hydrostatic pressure causing steam from the reservoir to flow up the wells (Aoyama et al; 2022). The steam is used to turn turbines connected to a generator (Assad et al., 2021) and is then condensed to form liquid water and is injected back into the reservoir. The electricity yield in vapor-dominated geothermal power plants reach up to 1500 MWe (Zarrouk et al., 2014) but those power plants have a high maintenance cost due to the corrosion of the turbines and pipes over time (Gallup, 2009).

The geothermal energy sector is growing and attracting new ideas (IEA Geothermal, 2022). Methods are being developed to make geothermal energy accessible to more places and affordable by reducing the need to drill deep boreholes, repurposing already existing wells and minimizing the cost of infrastructures installation (Moore, 2020; Norbeck et al., 2023). Those methods open a door to new potential fields for geothermal power plants. However, generating electricity from heat does not only depend on the available technologies. The heat recovery rate of geothermal plants depends on their environment. Initial rock temperature, accessible volume of rock, total fracture surface area, permeability of the rock volume are some of the main factors influencing geothermal power plants production capacity (Jung, 2013).

There is a nearly infinite supply of heat at temperatures high enough (> 150°C) to efficiently generate electricity nearly everywhere at sufficient depth (Tester et al., 2006).

However, the permeability is quite low at most places that are hot enough to generate electrical power. This restricts the rate at which water that can flow through the formation, and this limits the thermal power that can be recovered and the electrical power that can be generated. To remediate this problem, geothermal reservoirs are created by hydraulically fracturing hot, low permeability rocks (Olasolo et al., 2016). A few pilot projects are already undergoing evaluation (EIA Geothermal, 2022). So far, the pilots have shown that if the temperature difference at the injection well and production well as well as the pressure drop are maintained at a certain level relative to the initial conditions, EGS are economically viable and sustainable.

A key factor affecting the performance of EGS is the volume of rock and fracture surface area available for heat exchange. The aperture, width and length of the fractures, and the fracture density will play important roles in the thermal power that can be recovered (Lee et al, 2022). Fractures may already occur in the rocks forming the EGS, but they can be narrow and sparse and this limits the thermal power. Hydraulic fractures are then made to increase the fracture density and aperture, and to increase the rate at which water can be circulated through the hot rock. During hydraulic fracturing, fluid is injected into a perforated section of a well (Detournay, 2016). This nucleates a hydraulic fracture that propagates away from the well. Sand or other types of proppant may be injected into the propagating fracture to hold it open and maintain a working aperture. The location of the hydraulically fractured zone can be estimated by analyzing the micro-seismicity created during propagation or with a numerical model (Zhai & Sharma, 2005). Once this zone is located, a second well is drilled to intersect the fractured zone**.** Water is injected into one of the wells, it circulates through the hydraulic fractures while being heated and then flows back up the production well (Podgorney et al., 2021). Hydraulic fracturing increases the ratio of flow rate/pressure drop between wells and the accessible surface area in the rock,

which increase the rate of heat recovery and the potential to generate electric power (Tester et al., 2006).

EGS have been studied for the past few decades (Breede et al., 2013) but have only become popular recently (Norbeck, 2023, Department of Energy, 2019). The availability of technologies to enhance the energy recoverability percentage in a low permeability crystalline bedrock explains this fast-growing interest in EGS. The projects are under development in Europe, Australia and the USA using different flow rate stimulation and in different type of bedrock (IEA Geothermal, 2022). Some of those projects are derived from past concluded EGS pilot projects that are now extended to a bigger scale. Pilot projects showed that even though EGS can be a promising source of energy, they also present some challenges (Department of Energy, 2019).

Some limitations with EGS are related to infrastructure risks, and concerns about these risks. Creating a highly fractured zone and injecting high pressurized water can induce seismicity (Jung, 2013). Monitoring microseismic activity is then mandatory to ensure public safety. Some people have also expressed concern that fluids used during the fracturing step could pollute groundwater resources (Breede et al., 2013). According to models and surveys (Breede et al., 2013), there is currently no evidence that injected fluids used for EGS have reached drinking water resources, so the risk currently appears to be minimal. Another concern is that water used to recover heat will also recover radioactive elements if the geothermal reservoir is formed by rocks containing such elements. This is observed at several locations and as a result the composition of the recovered fluid is constantly monitored, workers in geothermal plants wear special safety equipment, and radionuclides are filtered from the recovered fluids (Breede et al.,

2013). These measures have successfully prevented the release of radionuclides to the environment at EGS sites.

A priority with EGS is to ensure that flow can occur between two wells at a rate that creates enough thermal power to generate electricity economically. This requires a flow monitoring system and a study of the fracture systems before injection. The water flow rate and energy recovery rate are indicators of the EGS success (Held et al., 2014). If the water flow is too low, the power generation will be uneconomic. On the opposite, water flowing rapidly through a localized, high permeability zone may not stay in contact with the bedrock long enough to extract heat. An ideal configuration is to create a large zone where the permeability is uniform and large enough to sustain significant flow. The EGS performance relies mostly on the zone chosen for the project and the bedrock properties (Olasolo et al., 2016).

One way to improve EGS performance is to use carbon dioxide injection instead of water injection (Olasolo et al., 2016). This technique is still under development, but researchers estimate an energy extraction rate five times greater than with water due to CO_2 higher mobility permitting high fluid mass flow rates (Randolph et al., 2011). It would also prevent radioactive transport in water. One limitation with CO_2 as a working fluid is that it requires a high-pressure environment. Another way to improve the performance of EGS is to perform a detailed analysis of the geothermal reservoir. Characterizing the bedrock using gravity, LiDAR and 3D seismic reflection surveys as well as bedrock core collection and analysis and groundwater sampling helps ensure the efficiency of EGS (EGI, 2018). Some field studies and 2D models (Pruess, 2007; Held et al. 2014) give a good estimate of the permeability, flow rate, heat flow, porosity and fractures. Building a 3D model with a fine grid can improve data estimation and increase the

EGS success. Some models of hydraulic fracture propagation have been determined (Zhai & Sharma, 2005) but more precise methods exist today to locate the fractures.

CHARACTERIZATION OF ENHANCED GEOTHERMAL RESERVOIRS

Micro-seismicity occurs near the tip of a propagating hydraulic fracture, so monitoring the locations of micro-seismic events can be used to characterize the locations of hydraulic fractures. Other characterization methods include well tests to evaluate the flow rate and to estimate fracture properties. Water is injected into one well and pumped out into another well. Pressure is measured at other monitoring wells and used for interpretation (Breede et al., 2013). Another option is to measure the strain caused by the pressure change during well test.

Optical fiber strainmeters have been used to measure the strain during well tests (Murdoch et al., 2021). They can measure horizontal and/or vertical strains depending on their design. They can sense very small displacements and thus have a high resolution. Pressure changes in the subsurface cause strain in the enveloping rocks, and measurements of the strain signal can be inverted to estimate the pressure changes. This approach has been used to characterize an oil reservoir using modest pressure changes (<1MP) caused by injecting water during a well test (Murdoch et al., 2022; Murdoch et al., 2020).

Pressurizing a zone of hydraulic fractures used to form an enhanced geothermal system should create a strain field that is sensitive to the orientation, size, and permeability of the EGS system. If this strain field can be measured, it should be feasible to invert the data to estimate the orientation, size, permeability, and possibly other aspects of an EGS system. This has the potential to be a new method of monitoring geothermal systems that could improve their performance.

OPTICAL FIBER STRAINMETERS

Optical fiber strainmeters have been used to measure multiple components of strain in the subsurface (Murdoch et al. 2000, 2023). The sensors used in those instruments are capable of ultra-high resolution strain measurements, yet they require no power downhole and are immune to electro-magnetic interference. To understand how optical fiber strainmeters work it is useful to review the construction of optical fibers themselves and the sensors used to measure strain.

Optical fiber

Optical fibers consist of a core enveloped by a cladding and an outer coating. The core of single-mode optical fiber has a diameter of approximately 9 μm and is usually made from fused silica glass (Janani et al., 2023). The cladding is also usually made of fused silica with a lower index of refraction (light travels faster) that the core to keep light propagating in the higher index core via total internal reflection. The core and the cladding of the optical fiber are fragile and are protected from breaks and deterioration by one to two layers: (1) a coating and (2) an outer jacket (Janani et al., 2023). The coating, can be made with different materials like acrylic, silicone or polyimide (Janani et al., 2023; Chang et al., 2017). Its thickness varies from a few μm to several 100s of μm. Optical fiber can be bought with those two layers only but handling it requires caution. The third layer, the outer jacket, provides additional mechanical support and protects the fiber from its surroundings. It is usually made with polyethylene (Janani et al., 2023).

The basic function of optical fibers is to transmit light with minimal losses, but they can also be used to create sensors that measure a wide range of parameters. For this project, two

optical fiber sensor technologies were used to design strainmeters: (1) Fiber Bragg Grating sensors and (2) optical fiber interferometers.

Fiber Bragg Grating

Fiber Bragg Grating (FBG) sensors are durable compact size sensors etched within the core of the optical fiber. They are few millimeters long and several FBGs can be etched along one fiber (Campanella et al., 2018). FBGs are a periodic perturbations in the core of the fiber that modulates the refractive index of the fiber (Figure 1). The perturbation is called a *grating* and is formed by exposing an area of the photosensitive fiber to the desired pattern, usually caused by two interfering ultraviolet light waves (Campanella et al., 2018). Several types of grating exist and are characterized by the spacing between the patterns as well as their length and shape (Lee, 2003). Those parameters define the grating period, Λ and the modulation strength which affect the refractive index of the fiber, n_{eff} and the Bragg wavelength, which is the wavelength of the reflected light,λ_B (Campanella et al., 2018)

$$\lambda_B = 2n_{eff}\Lambda \quad (1)$$

FBGs function by injecting a pulse of light with a broad range of wavelengths into an optical fiber. When the pulse crosses the optical fiber, light at the $\lambda_B$is reflected and the rest are transmitted forward (Figure 1).

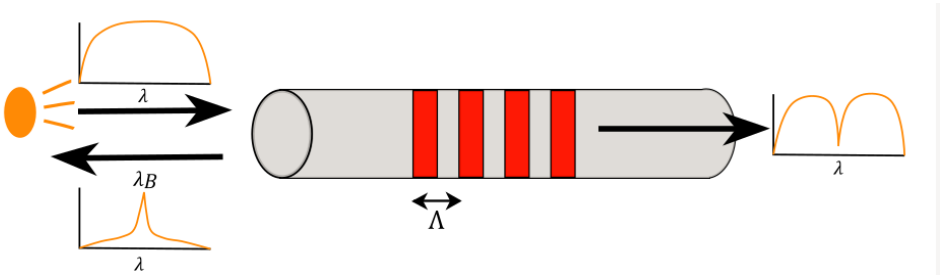

Figure 1. Conceptual model of a Fiber Bragg Grating sensor. The core of the fiber (in grey) contains perturbations in refractive index (red), called a grating. Perturbations in the grating are spaced a distance Λ apart. The incoming light includes a range of wavelengths, and a wavelength, λ_B, is reflected by the grating while the rest is transmitted. The spacing between the gratings defines the reflected wavelength according to (1).

The reflected wavelength depends on the spacing of grating, so displacement along the axis of the fiber that changes the grating spacing will change λ_B. Axial strain is the displacement between two points on the fiber normalized to the distance between the two points. Strain across the FBG can be determined using

$$\varepsilon = \frac{\Delta\lambda}{\lambda \times 0.79} \qquad (2)$$

where λ_i is the initial reflected wavelength, $\Delta\lambda$ is the change in reflected wavelength, and 0.79 is a constant resulting from Campanella et al (2018).

Optical fiber interferometry

Interferometry is the standard for making precise measurements of displacement since one interference fringe is proportional to the wavelength of the light used (several hundred nanometers to microns). This can be improved to sub-picometer displacements by using fractional fringe counting methods (Zumberge et al., 2004).

An interferometric sensor requires a light source that is divided into two beams when it enters the instrument. The beams take two different paths or interferometer arms, often denoted as reference and sensing, that some distance later recombine to form interference fringes, a pattern of high and low intensity corresponding to the relative phases of the two wavefronts (Hariharan, 2007). Figure 2 shows a common implementation of an optical fiber Michelson interferometer where the laser light enters one port of a 3x3 coupler and is divided light to propagate along two different paths that reflect off mirrors. The returning light from each interferometer arm recombines at the 3x3 to form interference fringes that exit the two remaining ports of the coupler whose intensities are measured by photodetectors. These detectors measure an intensity that is at a maximum if the two returning wavefronts interfere constructively, i.e , if the lengths of the two paths differ by an integer number of wavelengths (in-phase), and a minimum intensity if they interfere destructively, or differ by a half wavelength (out-of-phase).

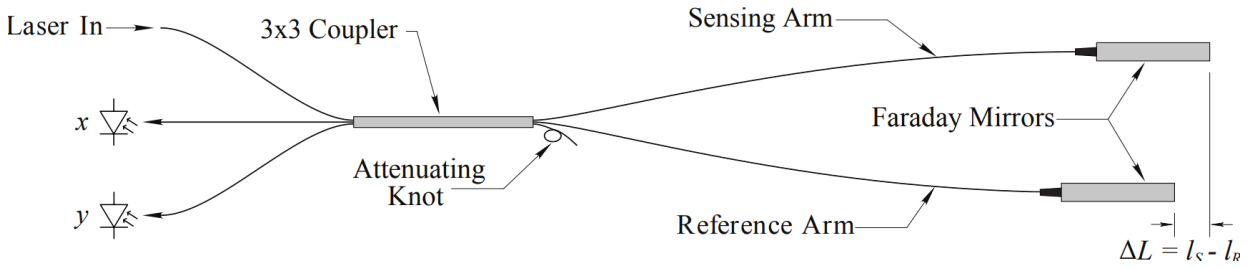

Figure 2. Diagram of a polarization insensitive optical fiber Michelson interferometer.

The change from constructive to destructive back to constructive interference as the lengths of the two paths vary with respect to one another is referred to as an interference fringe. In a Michelson interferometer this represents a displacement of one-half wavelength (since the light travels each path twice) or an optical phase difference between the two wavefronts of 2π radians. In an optical interferometer the optical phase change $\Delta\phi$ is related to the changes in the physical length, ΔL as: (DeWolf et al., 2015)

$$\Delta\phi = \frac{2\pi n}{\lambda}\Delta L \quad (3)$$

where λ is the wavelength of the light source and n the index of refraction of the optical fiber.

When strained, the observed optical phase change in a fiber is a combination of the mechanical elongation and the change in the optical properties, which can be described as (DeWolf et al., 2015)

$$\Delta\phi = \frac{2\pi\mu L_0}{\lambda}\epsilon \quad (4)$$

where L_0 is the unstrained fiber length and the gain factor μ = 1.16 accounts for the strain-optic effect (Bertholds and Dändliker, 1987). Changes in the state of interference can be measured as changes in intensity, I, by a photodetector which is related to the optical phase difference as (DeWolf et al., 2015)

$$I = I_0 \cos(\Delta\phi) \quad (5)$$

where I_0 maximum fringe intensity (i.e., perfect constructive interference).

Optical fiber Michelson interferometers are often built with a 3x3 fiber coupler and two Faraday mirrors reflecting the laser (Figure 2). These special mirrors are designed to eliminate the common problem of polarization fading in optical fiber interferometers wherein the orientation of the electric field vector is differentially altered along the two separate interferometer paths leading to poor interference contrast (Kersey et al., 1991). However, Faraday mirrors cannot be used for temperatures above 85°C as the magnets inside lose their effectiveness. Thus, it is currently infeasible to use a Michelson interferometer to measure strain at geothermal temperatures for prolonged time periods. A potential solution would be to use

Mach-Zehnder interferometers (MZI) instead to create a high resolution strainmeter since they use a pass-through topology and therefore only require an additional coupler and not Faraday mirrors.

An optical fiber MZI (Figure 3) is typically built with two optical fibers connected to a 2x2 or 3x3 input coupler on one side and to a 3x3 output coupler on the other (Zhang et al., 2021). One of the fibers is used as the reference arm that is ideally isolated from deformation whereas the other fiber is the measurement or sensing arm that is exposed to deformation. Only one fiber of the 2x2 input coupler is used to inject laser light into the interferometer where it is divided along the two paths. These two beams recombine at the 3x3 output coupler where a set of three phase shifted interference fringes emerge, however, only two are connected to photodetectors that are designated as x and y.

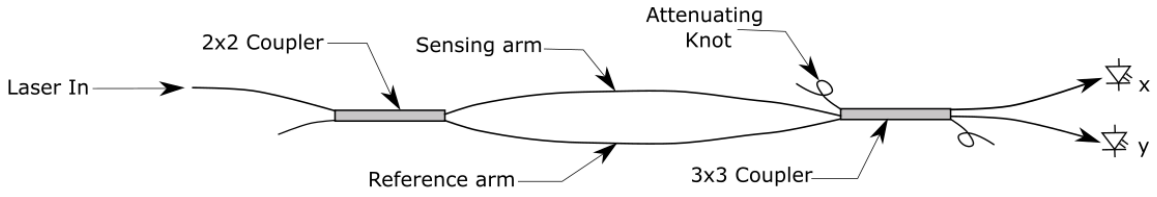

Figure 3. Diagram of an optical fiber Mach-Zehnder interferometer.

Both the optical fiber Michelson and Mach-Zehnder interferometers shown in Figures 2 and 3 employ 3x3 couplers to resolve the bi-directional phase ambiguity inherent to Eq. (5). This is because the change in the intensity measured by a single photodetector is the same whether the sensing arm lengthens or shortens by the same amount. This can be resolved by using a 3x3 coupler since it not only divides the amplitude of the light passing through, but also phase shifts each wave by 120° (Sheem, 1981) thereby providing additional information.

Expanding on Eq. (5), changes in the state of interference can be measured as changes in intensity measured by a photodetector x, which can be related to the optical phase difference as (DeWolf et al., 2015)

$$x = x_0 + a\cos(\Delta\phi + \phi_0) \tag{6}$$

where x_0 is an arbitrary DC offset, a is the maximum fringe intensity (i.e., at perfect constructive interference), and ϕ_0 is an arbitrary initial phase. A second phase shifted interference fringe is extracted from the adjacent port of the 3x3 coupler resulting in another relationship for the optical phase

$$y = y_0 + b\sin(\Delta\phi) \tag{7}$$

where y_0 and b are the analogous DC offset and amplitude as in the previous relationship. These sine and cosine expressions are the parametric equations of an ellipse that can be combined to solve for the optical phase, where the five shape parameters (a, b, x_0, y_0, and ϕ_0) are determined by linear least-squares (Zumberge et al., 2004). A real-time plot of these two phase-shifted interference fringe intensities sweep out a Lissajous pattern in the shape of an ellipse where the direction of the orbit of the instantaneous x,y value pair about this ellipse determines the direction of optical phase change, thereby resolving the directional phase ambiguity. This ellipse fitting and arctangent demodulation are performed in real time using a digital signal processing algorithm (Zumberge et al., 2004) to output the optical phase and therefore the strain in the sensing fiber relative to the reference.

EGS Research at Utah FORGE

Motivated by the need to improve the performance of EGS, the US Department of Energy (DOE) has funded a research program to evaluate and demonstrate new technologies at the Utah FORGE (Frontier Observatory for Research in Geothermal Energy) site.

The program includes field research in well drilling, well stimulation by hydraulic fracturing, well testing, heat production and novel methods for monitoring these processes (Moore, 2020). It also includes laboratory characterization and development of 3D models of EGS (Lee & Ghassemi, 2022).

The Utah FORGE site is in the southeast of the Great Basin in southwestern Utah. There are two geological units, the bottom unit is granite and other crystalline plutonic rocks, and it is overlain by unconsolidated alluvium (Podgorney et al., 2021). The temperature of the bedrock reaches 200°C at 2297 m depth (Xing et al., 2021) and it is approximately 225°C in a deeper well. Preliminary induced fractures have been created at the beginning of the project to study the stress field (Moore et al., 2019.). Hydraulic fractures were created from well 16A-78 in the spring of 2022, and a second well, 16B-78, was drilled to intersect those fractures. Additional hydraulic fractures will then be created between the two wells, and then hydraulic well tests will be conducted to evaluate the rate at which water can be circulated and heat extracted.

Problem Statement

Strain data could be an important new way to monitor EGS in general, and at the Utah FORGE site in particular, but this application is limited by the capabilities of current strainmeters (DeWolf et al., 2015). Some optical fibers and epoxies used to build strainmeters degrade at elevated temperatures typical of geothermal settings. For example, acrylate coatings

commonly used on telecom optical fibers are rated to 130°C and the glass transition temperature of many epoxies is in the range of 100 – 150°C. These materials are unsuitable for applications at temperatures of geothermal settings, 150—250°C. Optical fibers and epoxies that are rated for service at higher temperatures are known, but they have not been evaluated for use in strainmeters.

Moreover, optical fiber Michelson interferometers currently use Faraday mirrors to eliminate polarization fading. Faraday mirrors are currently unavailable for service temperatures above 85°C as the magnets inside lose their effectiveness. Thus, it may be infeasible to use a Michelson interferometer to measure strain at geothermal temperatures for prolonged time periods. It may be feasible to use Mach-Zehnder interferometers instead to create a high resolution strainmeter since they do not require Faraday mirrors, however, active polarization control may be needed.

Recent work has shown that strainmeters at shallow depths (less than 100 m) can detect strain signals from pressure changes in underlying reservoirs. (Murdoch et al., 2022). Temperatures at shallow depths are typically cooler than temperatures in geothermal reservoirs at depths of one to several km, so deploying strainmeters at shallow depths is one approach to avoiding the problem of having strainmeters function at high temperatures. However, many shallow settings are characterized by unconsolidated sediments. High resolution strainmeters are typically deployed in lithified rock and they are coupled to rock with expanding cement. Extensometers designed for unlithified materials have been deployed using direct-push drilling methods that use friction to couple the strainmeter to the formation (Murdoch et al, 2015). Preliminary testing has shown that this approach can be effective when using optical fiber FBG

sensors, but this approach has never been evaluated using high resolution optical fiber interferometers, like Michelson or Mach Zehnder interferometers.

OBJECTIVES

The objective of this project is to evaluate the feasibility of characterizing strains in geologic media at elevated temperatures and in unconsolidated materials in order to improve applications of strain data in geothermal, or other settings.

APPROACH

The objective of the thesis was met by designing prototype strainmeters and testing them under geothermal reservoir conditions. A split-sleeve strainmeter was designed and a prototype was built using composite materials and fiber optics designed for high temperature service. The device was then tested by applying small strains in an experimental apparatus at temperatures between 200 and 250°C. Strain measurements were made and analyzed to determine the feasibility of measuring strain data at reservoir temperatures. A direct-push strainmeter was designed and built around a urethane casting with two optical fiber measurement technologies: (1) Fiber Bragg Gratings (FBG) and (2) a Mach-Zehnder interferometer. The prototype was tested under hydrostatic pressure in the lab and during pumping tests in the field. These data were used to determine the feasibility of measuring strain in unconsolidated soil as well as evaluating novel methods for calibrating interferometers. Numerical models were developed and used to evaluate the strain measurements from the lab and field.

ORGANIZATION

The thesis is organized into six chapters. Chapter One is an introduction to Enhanced Geothermal Systems and strainmeters. Chapter Two describes the field sites used for

experiments. Chapter Three presents the work done to develop a high temperature split-sleeve strainmeter and describes the results of experiments and simulations used to evaluate the instrument. Chapter Four explains how a direct-push strainmeter was developed, the laboratory data obtained during calibration and field data to evaluate performance. It also includes simulations evaluating performance. Chapter Five is a discussion of the results and Chapter Six is the Conclusion.

Chapter Two: FIELD SITES

This research was conducted at the Utah FORGE site in Utah, and at the Clemson University Bull Farm Research site in South Carolina. The properties of the Utah FORGE site set the requirements for the development of optical fiber strainmeters. Some of the conditions at Utah FORGE are similar to the conditions at the Clemson site, so the Clemson site was used for preliminary testing.

UTAH FORGE SITE

The Utah FORGE site is near Milford, Utah 350 km south of Salt Lake City. It is in the southeastern Great Basin in an alluvial fan on the eastern edge of a basin adjacent to the Mineral Mountains.

An area approximately 5 km^2 and 5 km west of the Blundell geothermal power plant has been leased by the University of Utah for EGS research (Figure 4). Adjacent property owned by the U.S. government and managed by the Bureau of Land Management is also available for research after appropriate permits are secured.

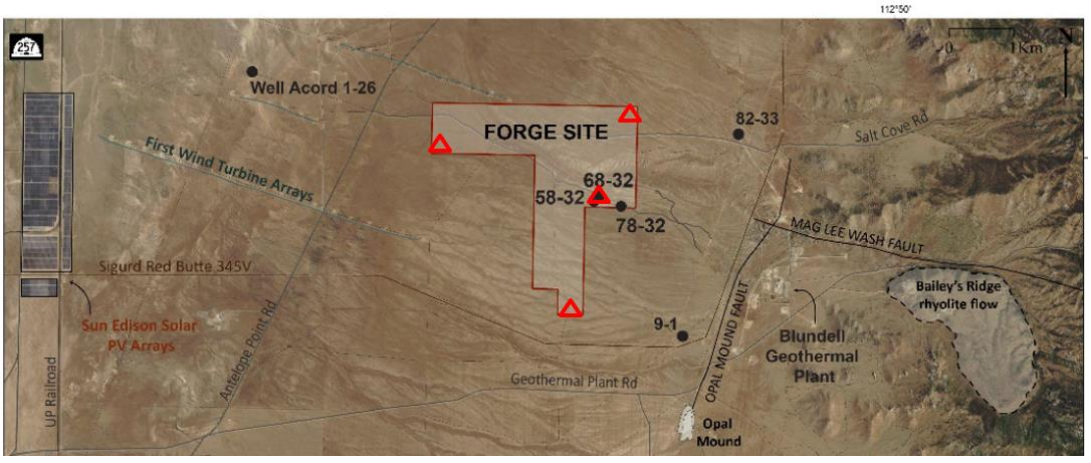

Figure 4. Utah FORGE field site (Moore, 2020). The red triangles represent the locations of the four strainmeters deployed.

The bedrock is mostly granitoid formed during the Miocene with younger rhyolite formations and is exposed 8 km east to the site. These formations crop out in the Mineral Mountains range and occur in core from the Utah FORGE site. Folded Precambrian gneiss also occurs in the mountain range (Podgorney et al, 2021). The bedrock is overlain by interlayered alluvium and volcanic deposits. The contact between the bedrock and alluvium dips approximately 30° to the west (Figure 5. Cross section of the Utah FORGE site. The well 58-32 is a pilot well. It was used to do underground investigation to learn about the fracture system and the bed rock properties (used with the permission of Utah FORGE).). This causes the thickness of the alluvium to range up to 1,200 m underlying the site (Podgorney et al, 2021).

The Great Basin and the Mineral Mountains range are both characterized by extensional tectonics causing north-south-trending normal faults in the site area. One of the faults is inferred to be the contact between the alluvium and underlying granitoid bedrock dipping to the west (Figure 5). Natural fractures occur where the bedrock is exposed in the mountains, and fractures also occur in cores from the site. Their length and spacings vary throughout the bedrock. The two major fault systems at Utah FORGE are characterized by (1) E-W strike with dip to the north and (2) NNE-SSW strike with dip to the west and normal displacement. These fault systems are inferred to have been formed during the middle Miocene due to uplift and tilting causing the normal fault to dip steeply to the west (EGI, 2018).

The state of stress at the Utah FORGE site was characterized using a Diagnostic Fracture Injection Test. The results indicate that the direction of minimum compression in the granite bedrock is horizontal and oriented ESE-WSW (EGI, 2018).

The state of stress data was used to design wellbores and hydraulic fractures at Utah FORGE. Hydraulic fractures typically form normal to the least principal compression direction,

and wellbores accessing hydraulic fractures are typically drilled in the direction of least principal compression. Measurements of the state of stress indicate that hydraulic fractures should be approximately vertical with a strike of North-South. The optimal orientation of horizontal wells that intersect the hydraulic fractures is parallel to the direction of least principal compressive stress.

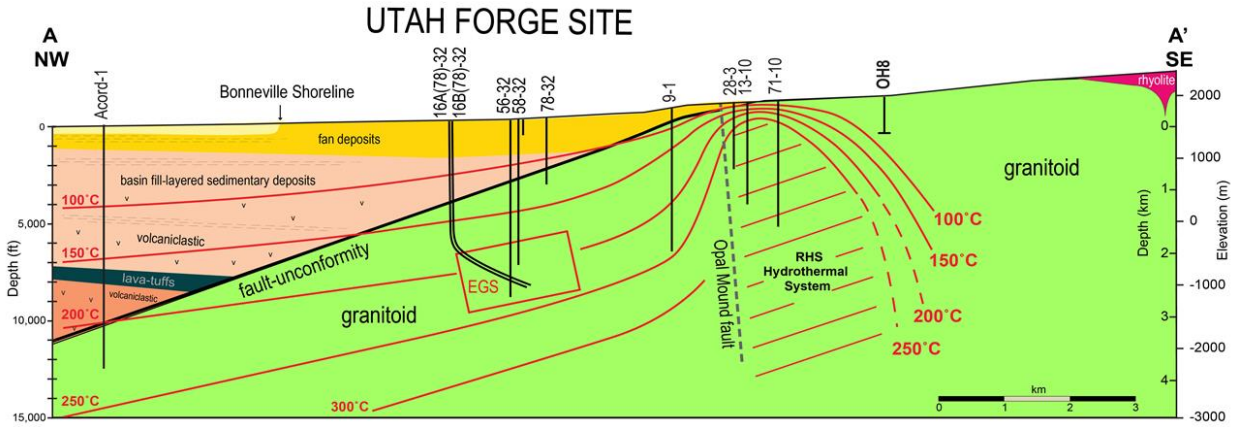

Figure 5. Cross section of the Utah FORGE site. The well 58-32 is a pilot well. It was used to do underground investigation to learn about the fracture system and the bed rock properties (used with the permission of Utah FORGE).

Well 16A(78)-32 was drilled to a vertical depth of 2.6 km and then is was curved to plunge of 65° and an azimuth of N15E (Podgorney et al, 2021). This well was used to create a few preliminary hydraulic fractures, and another well 16B(78)-32 was drilled approximately 100 m above 16A(78)-32.

Four strainmeters have already been deployed at the Utah FORGE site (red triangles in Figure 4). Each instrument contains four Michelson interferometers in a stainless-steel casing. The sensing fibers are wrapped around aluminum elliptical cylinders and the reference fibers are wrapped around cylindrical stainless-steel cylinders. Each elliptical cylinder is oriented in a different direction so the strainmeter measures strain tensors. The elliptical cylinders are in a

steel casing that is filled with epoxy and grouted in a borehole, so the strains acting outside of the casing are transmitted to the fibers inside without damaging them.

CLEMSON BULL FARM SITE

The Bull Farm Site is at the north end of the Clemson University Simpson Station near Pendleton, SC. The site is a 0.25 ha section of a 12-ha pasture used for grazing (Figure 6). The main vegetation is fescue grass and weeds typical for the area. The topography slopes gently to the northeast toward Little Garvin Creek, a second-order tributary that flows to Three and Twenty Creek.

The site has been used to develop and evaluate strain sensors, conduct hydraulic fracturing experiments and other research applications for more than 20 years. Two pumping wells and several monitoring wells are available at the site along with a variety of prototype strainmeters.

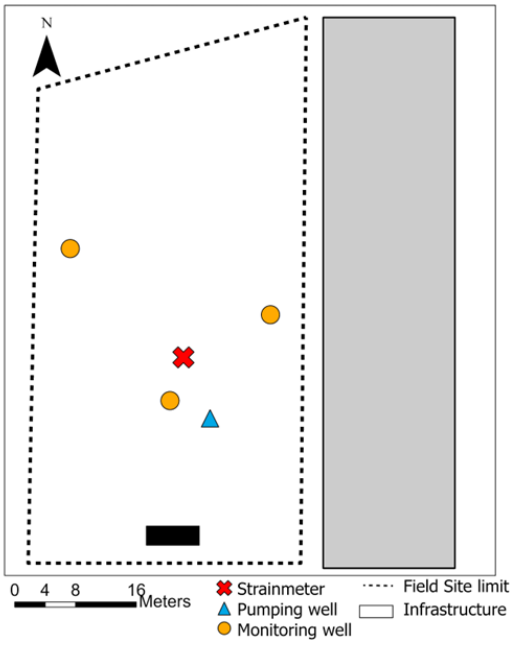

Figure 6. Map of the Clemson Bull Farm site. The 0.25 ha field is located next to a storage building represented in grey. Black rectangle is a storage shed.

Geology and Hydrogeology

The bedrock is Caesar's Head granite, a biotite-granitoid gneiss at a depth of about 30 m (Murdoch et al, 2006). Saprolite, an unconsolidated residuum of mostly clay, quartz and iron oxide, overlies the granite and is capped with a silty-clay soil approximately 2.5 m thick. The water table occurs at approximately 9 m depth, so the saturated thickness overlying the bedrock is approximately 20m (Figure 7).

The hydraulic conductivity of the saprolite was measured to be 2.4×10^{-5} m/s at 3 m depth (Murdoch et al., 2006). Constant-rate pumping tests indicate the hydraulic conductivity in the saturated zone is 1.3×10^{-6} m/s, more than an order of magnitude less than that of the top of the saprolite. The overlying soil layer is a poorly structured clay to sandy clay loam soil. The hydraulic conductivity is less than 10^{-9} m/s, according to measurements made with a Guelph permeameter (Murdoch et al., 2006).

The hydraulic head gradient indicates that groundwater flows to the northeast, towards Little Garvin Creek located 500 m east of the site (Figure 7).

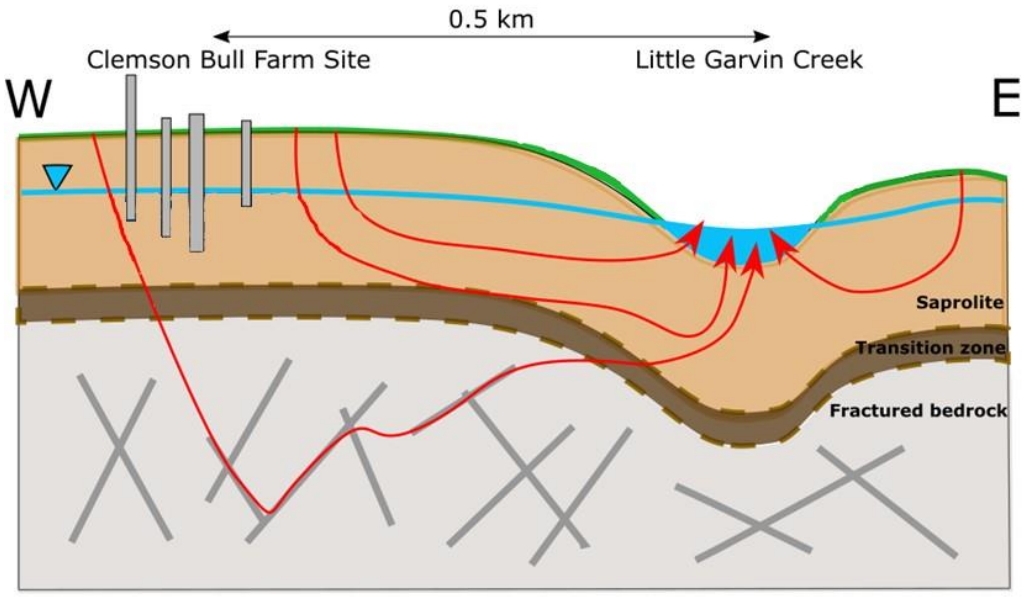

Figure 7. Schematic cross-section of the Clemson Bull Farm Site. The wells penetrate an unconfined aquifer in saprolite. Water flow is represented with red arrows.

Wells and Sensors

Two pumping wells, and five monitoring wells along with several dozen other sensors and borings are used for different projects. For this project four wells were used: SWL-4, SWL-5, SWL-7 and PW2 (Figure 8). The groundwater well PW2 (Pumping Well 2) contains a Berkeley JP Composite Seies downhole pump. The 4-inch diameter pump is 22 m deep in the well. The borehole is 30 m deep and was drilled with an 8-inch diameter air rotary bit. Bentonite and cement grout were used to complete the well with 4-inch PVC casing and screen. The screen extends from 10 m below the surface to the bottom of the well. The piezometers used for this project (SWL-4, SWL-5 and SWL-7) were installed using a 4-inch outer diameter solid stem auger and completed with 2-inch PVC casing and screen. SWL-4 is 13.7 m deep, and its screen extends from 12.2 m to 13.7 m depth. It is the furthest well from the pumping well at a radial distance of 20.9 m. SWL-5 is 18.2 m deep and its screen extends from 15.2 to 18.2 m depth. It is located 6.7 m from PW2. SWL-7 was drilled to a depth of 12 m and the screen is 1.5 m long.

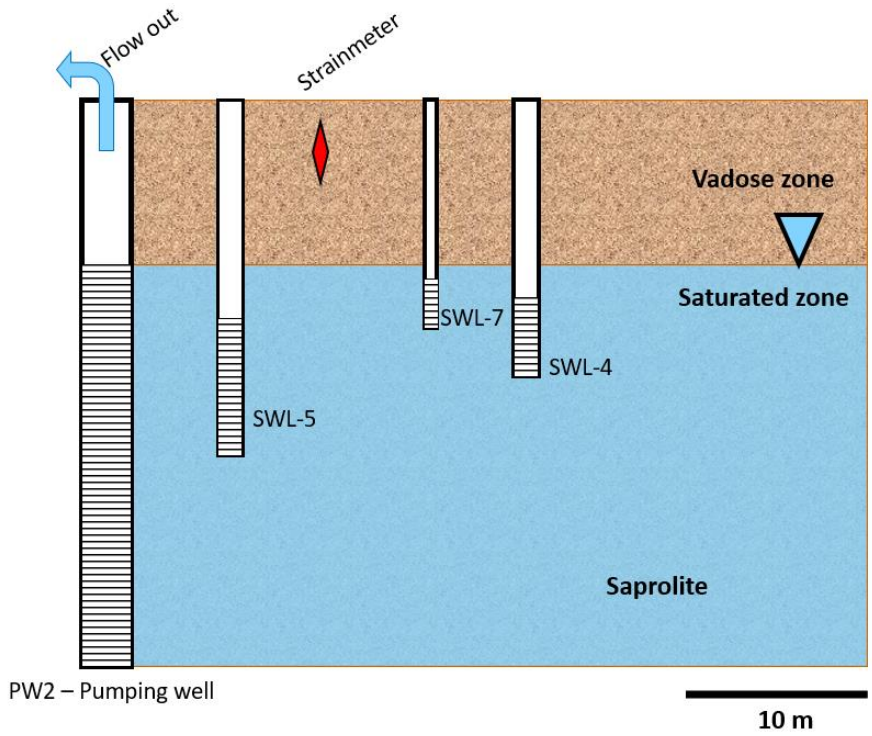

Figure 8. Conceptual model of the field site showing the strainmeter used during pumping test, the pumping well and the monitoring wells.

Changes in hydraulic head were measured with Onset HOBO U20L-04 transducers set 3 m below the water level in the well. The transducers have a span of 4 meters and a resolution of 0.14 cm of head. Strain was measured at strainmeter SMP1 located 10 m from the pumping well at a depth of 4.2 m (Figure 8).

Chapter Three: HIGH TEMPERATURE STRAINMETER

This chapter presents the work done to develop a strainmeter that can function at geothermal reservoir temperatures. Prototypes were designed, built, and refined. Tests in the laboratory were done to evaluate performance and longevity. Numerical models were built to interpret the strain signals measured during lab experiments.

DESIGN OBJECTIVES AND CONSTRAINTS

The design of the high temperature strainmeter was guided by objectives and constraints that were intended to make it useful for applications in geothermal reservoirs. The constraints include the strain components, strain resolution, range of operations temperature, deployment logistics and size.

Strain Components

A major advantage of using a strainmeter is that it can measure multiple components of strain. Distributed strain sensors created using optical fibers typically measure only one strain component, parallel to the axis of the fiber, although some techniques like the Baker Hughes WIRE sensor have some resolution of strain off the axis of the fiber (Murdoch et al. 2020). Optical fiber tensor strainmeters are typically cylindrical and they can currently measure three strain components normal to their axis, which is sufficient to resolve the strain tensor in the plane normal to axis. They can also measure strain parallel to their axis. Taken together, this is sufficient to measure the full strain tensor in a vertical borehole drilled to shallow depths on flat ground. This is because a principal strain component will be vertical under these conditions. As many as two other components, a total of six, are needed to measure the full strain tensor when the strainmeter is at an arbitrary orientation.

Each strain component contains information about the evolution of the deformation field in the subsurface, so including more strain components will increase the value of the dataset created by an instrument. The baseline goal of the high temperature strainmeter is to measure three components normal to, and one parallel to the axis of the instrument, similar to current tensor strainmeters. Intermediate prototypes could measure fewer components than this, but the goal is for the design to accommodate at least four strain components.

Strain resolution

The high temperature strainmeter needs to be capable of accurately resolving strains expected to occur in the vicinity of wells operating in geothermal reservoirs, and it also needs to resolve larger strains in the laboratory.

Field measurements

One approach to estimating the constraint for field measurements is based on observations during well tests at a site in the North Avant Field, Oklahoma. Strain rates at this location were approximately 1 to several nε/hr during well tests measured with instruments several hundred meters from the well (Murdoch et al, 2023). The strain rate during well tests at depths of a few 10s of meters in saprolite were in the range of hundreds to thousands nanostrain per hour. The faster rates occurred at wells within approximately 10 m of the pumping well and in saprolite, which is much softer than bedrock.

The strain field in the vicinity of hydraulic fractures at the Utah FORGE site was simulated by assuming the hydraulic fracture was a thin elliptical hole loaded by a driving pressure at a depth of 2.5 km (Figure 9). The dimension of the fracture was assumed to be 250 m high x 350 m horizontally, based on interpretation of microseismicity. The driving pressure in

the simulation was adjusted until the fracture displaced a volume of 500 m^3, which is the volume injected during a well stimulation operation conducted at the Utah FORGE site in April 2022. The elastic modulus of the site was assumed to be uniform and equal to 50 GPa, which is typical of the crystalline rocks underlying the site.

The strain field defined by the 1 nε contour extends up to the ground surface and spans a region more than 10 km across, according to the simulations (Figure 9). The pattern of each component is unique, and the patterns are sensitive to the orientation, size, driving pressure, and other aspects of the hydraulic fracture. This is encouraging because it indicates that it should be feasible to estimate properties of the hydraulic fracture using strains measured remotely. However, it indicates that strain magnitudes at shallow depths are likely to be in the 1 nε range at the end of a stimulation.

Currently available strainmeters are capable of resolving considerably less than 1 nε (Murdoch et al., 2023), but site conditions may cause the magnitude that can be detected to be greater than instrument capabilities. Indeed, measurements at the Utah FORGE site indicate ambient noise of approximately 1 nε over a period of approximately 1 hour, which is the duration of the hydraulic fracturing procedure. This indicates that the expected magnitude of the strain field at shallow depths is approximately the same as the ambient noise, which is discouraging because it indicates that the signal from hydraulic fracturing at 2.5 km depth is likely to be obscured by noise when measuring strain at shallow depths (Figure 9).

This result indicates that the maximum strain at the end of hydraulic fracturing would be on the order of με (10^{-6}) in the vicinity of the hydraulic fracture. It is assumed that a signal to noise ratio of 10 is needed to accurately measure the strain. A study of the strain time series

would be necessary for interpretation, which requires that the strain be resolved early and that it continues to be resolved throughout the hydraulic fracturing operation. The hydraulic fracturing operation spanned several hours, and assuming that the strain study needs to be done in the first few minutes requires that the strainmeter can resolve approximately 0.01 of the maximum strain. This implies that the high temperature strainmeter should be capable of resolving approximately 1 nε (10^{-6} x 0.01 x 0.1).

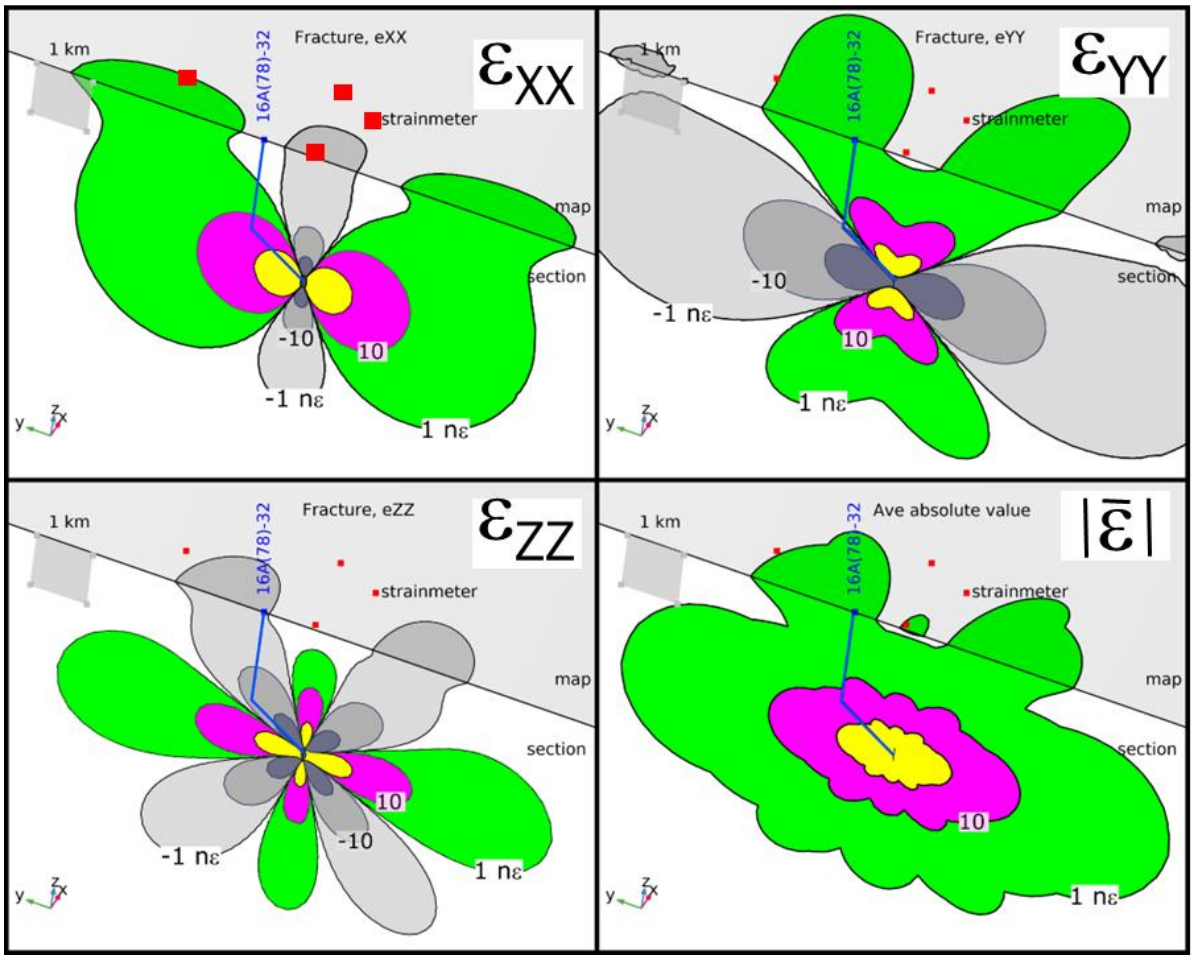

Figure 9. Normal components of the strain tensor field in the vicinity of a vertical hydraulic fracture at a depth of 2.5 km at the bottom of Well 16A(78)-32 at the Utah FORGE site. Color is positive, grey-scale is negative strain. Contour spacing is log scale—contours differ by factor of 10. Cross-section and map views, and locations of shallow strainmeters shown in red. The azimuth of the cross-section is approximately 110. Lower right panel is the mean of the absolute value of the normal strains

Lab-scale measurement system

The constraints on strain resolution outlined above are motivated by the anticipated requirements for field applications, but development work will be done in the laboratory first and additional constraints are needed for this application. Testing of high-temperature materials and packaging in the laboratory will likely create strains that are much larger and faster than strains caused by well testing. Moreover, the optical fiber configurations required for some high-resolution applications may be cumbersome to implement during development of high temperature instrument packages.

An additional constraint on strain measurement is a system that can resolve strains in the 1 to 10,000 με, and that can be implemented using a single fiber to facilitate applications in the laboratory.

Temperature range

The temperature of geothermal resources ranges from a few 10s of degrees above ambient air temperatures to magmatic temperatures approaching 1000°C, but the temperature of resources used to generate electricity are typically constrained within a narrower range. The temperature of EGS reservoirs used to produce electricity ranges from 100°C to 350°C, according to Breede et al, (2013). This temperature range is based on the efficiency of the different methods of generating electricity from heat. The lower temperature limit is based on the efficiency of a binary fluid Rankine-cycle generator. Rankine generators can generate electricity in the 80 to 100^{o}C range, but their efficiency increases as the temperature of the working fluid increases from 100 to 150^{o}C (Jimenez-Garcia et al. 2023). This creates economic challenges for

reservoirs with temperatures in the range of 100°C, and it likely was a factor in Jung's (2013) estimate of 150°C as the lower limit of an EGS reservoir that can create electricity economically.

Fervo Energy recently announced the completion of a 30-day-long EGS well test that demonstrated temperatures greater than 160°C and flow rates greater than 60 L/s, and these results are regarded as sufficient to economically generate electrical power.

Allowing water to flash directly to steam is more efficient than using a binary system with an organic liquid as the working fluid, but this requires higher temperatures than those used in binary systems. So called single-flash generators systems can be more efficient than Rankine-cycle system for temperatures in the 190 to 220°C range, whereas dual-flash systems are the most efficient using fluid in the range of 220 to 320°C (DiPippo, 2013). The temperature at the 16A(78)-32 well at Utah FORGE ranges from 175°C to 225°C (EGI, 2018).

These data indicate that a strainmeter designed for geothermal reservoirs should be capable of functioning at a minimum of 150°C, the lower limit where economic electricity generation is practical, according to Jung (2013). A strainmeter that would be deployed at the 16A well at FORGE should be capable of functioning at 225°C. An operational temperature of 300°C would allow a strainmeter to function in nearly all current geothermal wells. The temperature set points for functionality of the high temperature strainmeter will be 150°C as *required*, 225°C as *desired*, and 300°C as an *optimum goal*.

Deployment logistics

Strainmeters are deployed in boreholes to place them in the region where strain is occurring. The instrument needs to be coupled to the enveloping geologic formation so that strain within the formation is transferred to the strainmeter. Most strainmeters are cylindrical and

are coupled to the formation using expanding cement in the annulus between the cylinder and the borehole wall (Murdoch et al, 2019).

Rock temperatures sufficient to generate electric power typically occur at depths greater than 3 km (Jung, 2013), although the depths are slightly shallower in some locations, such as at Utah FORGE. Boreholes that reach these depths under hot conditions are expensive, with costs greater than several million dollars. It is impractical to drill boreholes strictly for monitoring applications, in most cases, so it is unreasonable to expect high temperature strainmeters to be deployed in dedicated boreholes. A more viable approach is to make use of boreholes drilled and completed as either water production/injection wells, or as monitoring wells that serve multiple technologies. This means that the strainmeter would be deployed in the annulus between the well casing and a borehole wall. An alternative would be to deploy an instrument with an axial hole at the bottom of a well casing. In either case, the instrument would be coupled to the formation when cement is pumped out the bottom and circulated up the annulus.

Optical fiber cables are routinely deployed in the annulus on the outside of casing, so deploying strainmeters on the outside of casing could be integrated with optical fiber deployment. This means that strainmeters would need to be configured onto the outside of casing as the casing is being lowered into a well during completion. Hourly costs during well completion are significant, so deploying a strainmeter should add minimal time to the completion process. Deploying a strainmeter in the annulus requires that the instrument be protected to avoid damage by the large forces generated during this process. Strong clamps and centralizers are used to hold optical fiber cable in place on the casing and to hold the casing away from the borehole wall during deployment, and these tools would also be available during strainmeter deployment.

Size constraints

The size of the strainmeter is constrained by the size of components that can be accommodated in the annulus of a borehole. The diameter of a wellbore that is free of obstructions should be 2-inches larger than the diameter of the casing, according to Roscoe Moss (1990). An obstruction in the annulus increases the required diameter of the borehole by an amount equal to twice the diameter of the obstruction. Increasing the diameter of the well bore increases the drilling cost, so changes in well diameter should be held to a minimum.

Including optical fiber cable and associated clamps introduces an obstruction that can require the diameter of the wellbore to be increased. Including optical fiber cable in the annulus has become common, and the associated additional costs have been accepted.

The goal is to limit the height of a strainmeter to the height of an optical fiber cable clamp. Optical fiber cable clamps will be required when deploying strainmeters, so this size constraint will avoid increasing the diameter, and cost of the boring beyond what is already required to accommodate clamps.

Several styles of devices are available to clamp and protect optical fiber to casing during deployment, and a mid-joint cable protector is a commonly used design that was available for inspection during this research. A mid-joint cable protector designed for a 5-1/2 inch casing consists of sheet metal several mm thick formed into rigid arcs and joined together with hinges. The cable protector is approximately 19 cm high (radial distance from the casing to the outside of the clamp) in most locations, but it is 21 cm high above a ridge that is used to clamp optical fiber cable. These heights will serve as the upper limits of the thickness of the strainmeter sleeve.

Thermal expansion

A strainmeter and a casing will both expand when heated from ambient to reservoir temperatures, and the difference in their expansion will affect the strainmeter performance. It was initially assumed the strainmeter would be mechanically coupled by tensioning onto casing. This implies that the strainmeter will loosen if the thermal expansion of the casing is less than that of the strainmeter. For example, if the coefficient of linear thermal expansion of the strainmeter is 2.2×10^{-5} 1/˚C and that of steel casing is 1.2×10^{-5} 1/˚C, then the hoop strain in the strainmeter will increase by their difference 1×10^{-5} 1/˚C. A temperature increase of 200˚C would cause a differential strain of 2×10^{-3}. The nominal circumference of a strainmeter built on a 2-inch pipe is 2.375 inches, or approximately 6 cm. This differential heating would cause the circumference to increase by 1.2×10^{-2} cm, or 120 microns (0.005 inch). If the strainmeter was initially tightened by more than this amount, then it could remain under tension and still function properly.

It is also possible that the coefficient of thermal expansion of the strainmeter is less than that of the casing. In this case, the strainmeter will tighten onto the casing. For example, assume that the coefficient of linear expansion of the strainmeter is 0.92×10^{-5} 1/˚C. Heating to 200˚C would cause a differential strain of 2×10^{-3}. Assuming the elastic modulus of the sleeve is approximately 10 GPa, indicates the stress in the sleeve would increase by approximately 2×10^{-2} GPa, or 20 MPa. Components of the strainmeter would be required to accommodate a tensile stress of this magnitude without failing. Fiberglass and carbon fiber composites can accommodate this stress, but the strength of other components, and bond strengths between components would need to be evaluated.

The goal is to match the coefficients of thermal expansion of the strainmeter and casing, their difference should be less than 1×10^{-5} $1/^{\circ}C$. A smaller difference in thermal expansion is preferred.

DESIGN CONCEPT

Several designs for the high temperature strainmeter were evaluated to meet the goals and constraints listed above. Three main parameters were taken into consideration during the development phase: (1) the geometry of the instrument, (2) the deployment of the strainmeter onto a well casing and (3) the strain sensors.

Geometries

The basic design concept that was developed to meet the goals and constraints is to create a strainmeter as a sleeve, or shell that wraps far enough around the casing to allow multiple components of strain to be measured. An ideal geometry is a tubular geometry that is split axially along one side (Figure 10). This split-sleeve design can be opened and placed around a casing and then fasteners can be used to join the sleeve at the split and apply tension. It should be feasible to deploy strain sensors around nearly the entire circumference, and this would facilitate measuring the strain tensor normal to the axis of the casing.

One drawback of the split-sleeve design is that it requires the sleeve to be flexible enough to be deployed around the casing without permanent deformation. This may be possible with some materials and thicknesses, but other materials and thicknesses will be too stiff to open sufficiently by flexing. Stainless steel sheets that are thicker than 1 to 2 mm will likely be too

stiff to accommodate enough flexing, for example. This is significant because the sleeve may need to be created from metal or thick composite to be durable enough to withstand deployment.

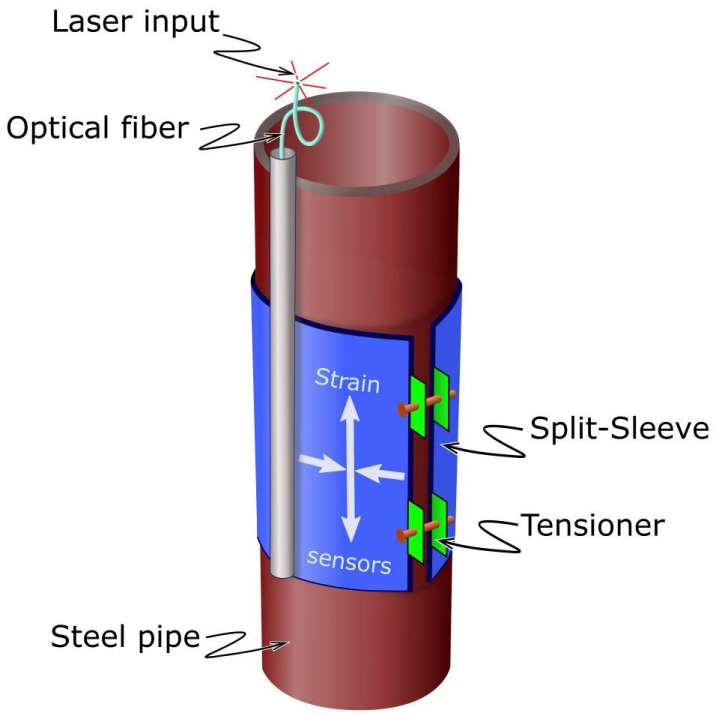

Figure 10. Design of the split-sleeve strainmeter wrapped around a steel pipe and clamped with tensioners. The split-sleeve strainmeter contains optical fiber sensors that measure multiple components of strain. .

An alternative design is a thin shell that wraps partially around the casing. This design would sacrifice coverage around the circumference, but it could be formed from metal or stiff composite material. For example, a shell that wrapped 180° around the casing could be rigid.

The design should accommodate strain sensors that are arranged either circumferentially or axially around the casing. The ratio of length to diameter should be greater than 4:1 in order to accommodate sensors that are arranged both around the circumference and parallel to the axis.

Clamping

Sensors in the strainmeter should be put into tension prior to deployment. This will facilitate measuring both expansion and contraction relative to an initial, tensioned state. Sensors that are at rest, not under tension, during deployment may underestimate compressive strains.

This can be accommodated by putting the sleeve or shell in tension when it is clamped to the casing. One approach is to attach tensioning fixtures to the edge of the sleeve and draw the fixtures together with a bolt. A similar approach could be implemented by attaching straps to a shell and tensioning the straps during deployment.

It is also possible to attach a sleeve or shell to a casing with an external clamp that compresses the outside of the sleeve onto the casing. This would apply a normal force that may help secure the sleeve to the casing, but it would avoid tensioning the sensors in the sleeve and therefore may diminish the performance of the strainmeter. The initial approach will be to clamp the sleeve to the casing under tension.

Sensors

Optical fiber strain sensors will be used to meet the design constraints. There are optical fiber sensors that can function at the desired temperatures and can provide the required strain resolutions. Optical fiber sensors are compact and can be embedded at different orientations in a protective sleeve or shell to complete the conceptual design.

COMPONENTS

Components to build the high temperature strainmeter were chosen to tackle the constraints listed above. The materials were chosen due to their physical properties and their availability.

Polyimide fiber splice

Strainmeters use optical fiber sensors due to their high sensitivity, simplicity, and lack of electromagnetic interference. There are several types of optical fiber depending on the material used for the coating around the fiber. Polyimide coated fibers can withstand temperatures of 150°C and above due to their high heat resistance and mechanical properties (Chang et al., 2017) allowing the fiber to be protected at elevated temperatures.

Optical fiber needs to be joined to a connector that attaches to an interrogator. Optical fibers also need to be joined to other fibers or components to create interferometers. The connection between two optical fibers is called a splice. To create a splice, two fibers are stripped of their protective coating, cleaved to create planar surfaces, and then put in a splicer that aligns the fibers and fuses them together. Removing the protective coating made from acrylate can be done with a mechanical tool. However, the bond strength between polyimide coating and the underlying optical fiber is too strong to remove the coating mechanically. Another stripping technique needs to be used.

Polyimide coating can be removed by heating the fiber to a temperature high enough to degrade the polyimide. Commercial tools are available to strip polyimide coating using high temperatures generated with electrical arcs or lasers, but these tools are expensive and were unavailable. Polyimide coating can also be removed by dissolution in a hot solvent (Janani et al., 2023). A system was developed to use heated solvent to remove polyimide coating in order to enable splicing of high-temperature polyimide optical fiber.

The polyimide stripped consists of a heated chamber that contains the solvent and the ends of optical fibers that are being stripped. To create this device, three holes were drilled in the

cap of a 15-cm tall insulated container and a block of aluminum with holes aligning with the ones in the cap was bolted onto it (Figure 11a and b) A 50 W stainless-steel cartridge heater and a K thermocouple were placed in each of the side holes. Both were wired to a controller so the desired temperature could be set and monitored (Figure 11). The aluminum block slows the rate of temperature change and helps to smooth temperature fluctuations caused by the controller. An aluminum sleeve with a 1-cm-wide base was made to contain a 1.5 mL glass vial, which was inserted into the aluminum block through a hole in the top cap. This device (Figure 11) will be referred to as a Tiny Oven Apparatus for Solvent Thermal Removal of optical fiber coating (TOASTR).

Polyimide is resistant to most chemicals, but it can be dissolved by a few special solvents. Dynasolve CU-7 (manufactured by Versum Chemicals and distributed by Ellsworth Adhesives) contains aqueous alkalis (NMP and DGA) and it is one of the few solvents that can dissolve solid polyimide (Janani et al., 2023). The effectiveness of the dissolution increases with temperature, presumably because the solubility of polyimide is temperature dependent. The boiling point of Dynasolve CU-7 is 205°C, and this limits the upper temperature of the dissolution application.

The TOASTR device is capable of heating to its boiling temperature, but lower temperatures were used during evaluation testing of the device. The technical datasheet of the CU-7 solvent indicates that application should be conducted at a minimum of 82°C, but it cites a range of 121°C to 176°C for most applications. An initial test was conducted by heating the solvent to 120°C. Six polyimide-coated optical fibers (manufactured by DK Photonics) were inserted 2.5 cm into the solvent in the glass vial in the TOASTR and then removed every five minutes and the polyimide coating was photographed under a microscope (Figure 13b).

(a) (b)

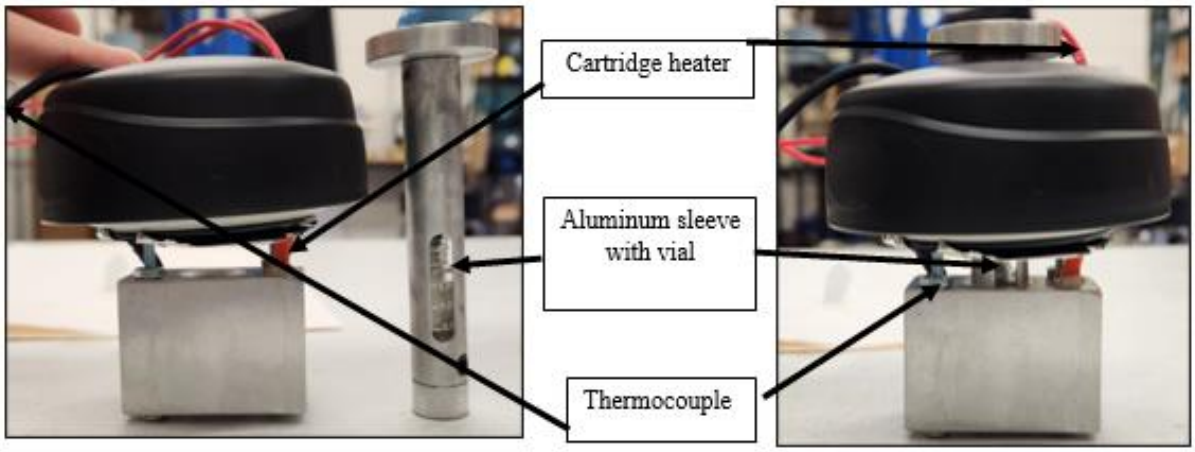

(c)

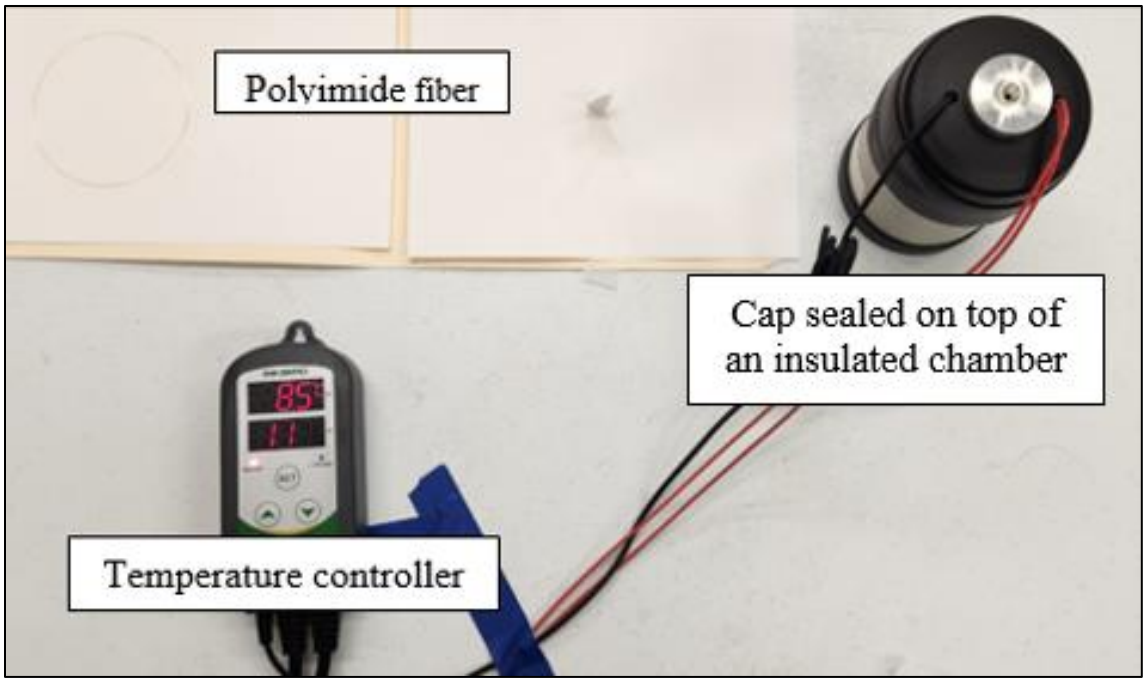

Figure 11. Device to strip polyimide coating from optical fiber using a heated solvent. (a) cap and sleeve containing vial shown separately in side view. (b) Vial and sleeve inserted into cap. (c) cap and sleeve attached to insulated vessel (thermos) with temperature controller view from above. A glass vial containing solvent is placed in an aluminum sleeve and inserted into an aluminum block, which contains a cartridge heater and thermocouple. The solvent is heated to 120˚C and the optical fibers are inserted through an opening in the sleeve containing the vial. .

The polyimide coating is brownish-yellow and approximately 10 microns thick. The appearance of the fiber that was exposed for 5 minutes is essentially the same as that of the original fiber, but the yellow color fades as the time of exposure increases. The fiber is essentially clear after 25 minutes, and the appearance is unchanged with longer exposure. It was assumed that the polyimide was completely removed after 25 minutes of exposure (Figure 12b and 13c-e). The polyimide appears to be completely removed after 25 minutes over the length of fiber that was immersed in solvent, but the color grades from clear to yellow over less 1 cm (Figure 13e) indicating the protective coating is unaffected where it is not immersed in solvent.

Polyimide-coated optical fiber that was stripped using heated solvent in the TOASTR was cleaved and fused in a fusion splicer using standard methods. The splices were heated to 200°C and remained fully functional, according to tests with a Optical Time Domain Reflectometer. This indicates that the solvent-based method is a viable approach for stripping polyimide coating from optical fiber prior to fusion splicing.

(a)

(b)

Figure 12. Polyimide fiber with its coating on (a) and the same fiber after 25 minutes in the Dynasolv solvent heated at 120°C (b).

(a) TOASTR optical fiber polyimide coating removal system during testing.

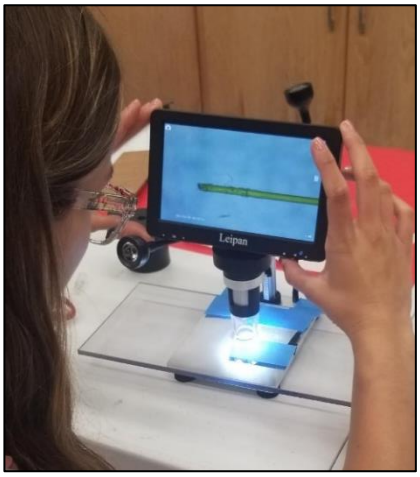

(b) Optical fiber imaging tool used to evaluate polyimide coating.

c.) Optical fiber with polyimide coating. The diameter of the fiber is 145 micron.

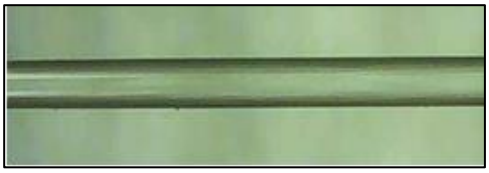

d.) Optical fiber with polyimide coating after 25 minutes of exposure to CU-7 at 120 ^{o}C.

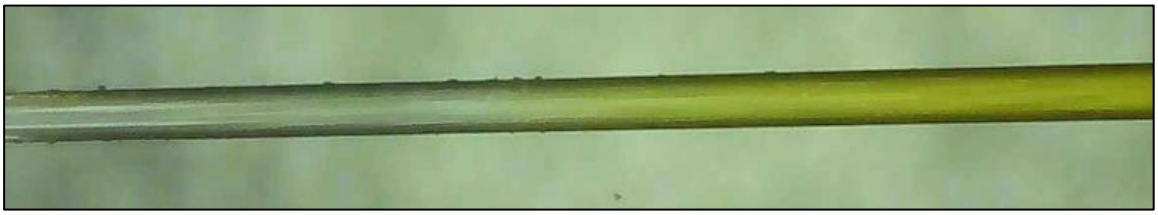

e.) Transition from intact to stripped fiber using heated Dynasolve CU-7 solvent at 120 ^{o}C.

Figure 13. The TOASTR device and resulting polyimide fiber during initial tests.

Strain sensors

Two optical fiber sensor technologies were used to design the strainmeter: (1) Fiber Bragg Grating sensors and (2) Mach-Zehnder interferometer.

Fiber Bragg Grating sensors

Fiber Bragg grating sensors offer several advantages compare to existing sensing technologies. They are light weight and non-invasive sensors that can be set to collect data remotely (Campanella et al., 2018). They are immune to electromagnetic and radio frequency interference and highly sensitive to strain as they can detect deformation as small as 0.64 pm (Lee, 2003). Most FBG interrogators measure over a bandwidth of 50 to 80 nm and the reflected wavelength of each grating requires a few nm of separation from that of the other FBGs on a fiber. This means that it can be possible to identify up to several dozen FBGs with different central wavelengths on a single fiber.

An FBG interrogator injects a broadband pulse of light into an optical fiber and light is reflected from each FBG at a wavelength that is proportional to the spacing of the Bragg grating. The wavelength of the reflected light changes as deformation changes the spacing of the fiber gratings. The FBG interrogator records the wavelength of the reflected light as a function of time, along with a reference wavelength. The strain at the FBG is proportional to the difference between the measured wavelength and the reference wavelength normalized to the reference wavelength (Campanella et al., 2018). Most FBG interrogators can resolve wavelengths of reflected light in the 1 pm range. The strain that can be resolve is approximately the ratio of the resolved wavelength to the central wavelength. So, resolving 1 pm out of 1550 nm is a ratio of $10^{-12}/1.55x10^{-6} = 0.6 \times 10^{-6} = 0.6\ \mu\varepsilon$.

The prototypes used in this research used FBGs in the range of 1550 nm or 850 nm so two different interrogators were used. A SM-125 Micron Optics interrogator (Figure 14) was used to read FBGs with center wavelengths in the range of 1510 nm to 1590 nm. It can read up to four fibers at the same time. The accuracy is 1 pm and the repeatability is 0.5 pm at 1 Hz

giving an strain measurement accuracy of 0.5με based on the interrogator performance. The signals are read at a frequency of 2 Hz that cannot be changed. The Micron Optics interrogator is operated by ENLIGHT, a software running on a computer. The reference Bragg wavelengths can be manually entered or detected automatically by the software. The user must define the type of sensor used and the wavelength-to-strain conversion equation.

A FiSens FBG X100 (Figure 14) was used to read FBGs with central wavelengths in the range of 808 nm to 880 nm. It is a single channel and the sampling frequency can be between 1 to 100 Hz. The precision is 1 με, and the digital resolution is 0.01 με, according to the manufacturer. The FiSens interrogator is operated by the BraggSens (single channel) monitoring software running on a stand-along computer. The wavelengths of the FBGs can be manually entered or detected automatically. Once the type of measurement done by the FBG is defined, the software calculates the wavelength-to-strain conversion itself.

Figure 14. Micron Optics interrogator (left) and FiSens interrogator (right).

Interferometer

Another type of optical fiber sensor is an interferometer. Interferometers give precise measurements of a displacement in the order of the nanostrain.

Optical interferometers are available that can measure strain with resolutions of 10^{-12}, many orders of magnitude greater than the capability of FBGs. Mach-Zehnder and Michelson

interferometers are both capable of resolving ne, so they can both meet the goal outlined above. The Faraday mirrors used in Michelson interferometers will likely degrade at elevated temperatures, so Mach-Zehnder interferometers appear to be the preferred configuration for geothermal applications.

A Mach-Zehnder interferometer will eventually be used in the split-sleeve strainmeter, but preliminary testing described here was limited to the use of FBGs. A Mach-Zehnder interferometer was built for a direct push strainmeter and is described in Chapter 4.

Sensor packaging

This research focused on designing a split sleeve strainmeter. The base of the strainmeter was made with fiberglass cloth and high temperature rated epoxy resin.

The fiberglass cloth used for this project is the FG-C0750R cloth from US Composites. It is made with electrical-grade glass (E-glass) fibers, a glass composition used for fiberglass fibers. It is a plain weave, 0.2 mm thick fabric and weighs 0.23 kg/m. Fiberglass is tightly woven together to form a fabric that can be combined with resin to shape it into a specific form. Three 30.5x40.6 cm rectangles were cut from a bulk roll to be used in the packaging.

The resin used for the packaging is Duralco 4461-IP resin and its hardener from Cotronics Corporation. The product datasheet indicates that the resin can be used for temperatures up to 260°C and acts as a protective coating for the material it is applied on. The resin has a viscosity of 600 cps, and the cured material has a tensile strength of 65 MPa and a thermal expansion coefficient of $5.4 \times 10^{-5}/^{\circ}$C. It is pale yellow when mixed at a 4:1 ratio (resin:hardener) and darkens when exposed to heat. It can cure at room temperature in 16 hours or at 120°C in 5 minutes. If cured at room temperature, the manufacturer recommends heat

treating for 1 hour at 120°C to strengthen the resin which was done for the presented prototype. When the resin is mixed with its hardener it introduces air which can alter the properties of the cured resin. The mixed resin was degassed in a vacuum chamber for 15 minutes.

The tensioning fixtures (tensioners) were cast as forged composites in a mold. They were formed from Duralco 4461 resin mixed with half-inch (1.27 cm) chopped carbon fiber tow (Feraboli et al., 2010). This fiber has a tensile strength of 246 MPa.

PROTOTYPE STRAINMETERS

The general fabrication procedure of the prototype strainmeter was a wet lay-up composite lamination technique (Figure 15) using the components outlined above. A goal was to limit to voids in the laminations, so several methods of lay-up were evaluated.

Several trial split-sleeve were made to find a replicable and efficient method of fabrication. Sleeves using low temperature rated resin were made to study the impact of air bubbles trapped in the fiberglass cloth and how to avoid them. The resin was applied with a brush or a syringe on the cloth lying flat on a surface or on a cloth wrapped and tapped around a pipe. Three curing methods were evaluated: curing in the room, curing in a pressure chamber and curing in the oven. Different peel ply and vacuum bags were also evaluated. The vacuum bags created ridges on the sleeve, but the sleeves created using Fibre-Glast Econostich peel-ply made with nylon were smooth with minimal amount of air bubbles. Air bubbles can create points of weakness within the sleeve. They increase the risk of cracking when the sleeve is flexed by concentrating stresses. They can also cause a gap in the sleeve-strain sensor-pipe contact area and alter the strain measurements. Finding a procedure and materials causing the least amount of air bubble was a priority.

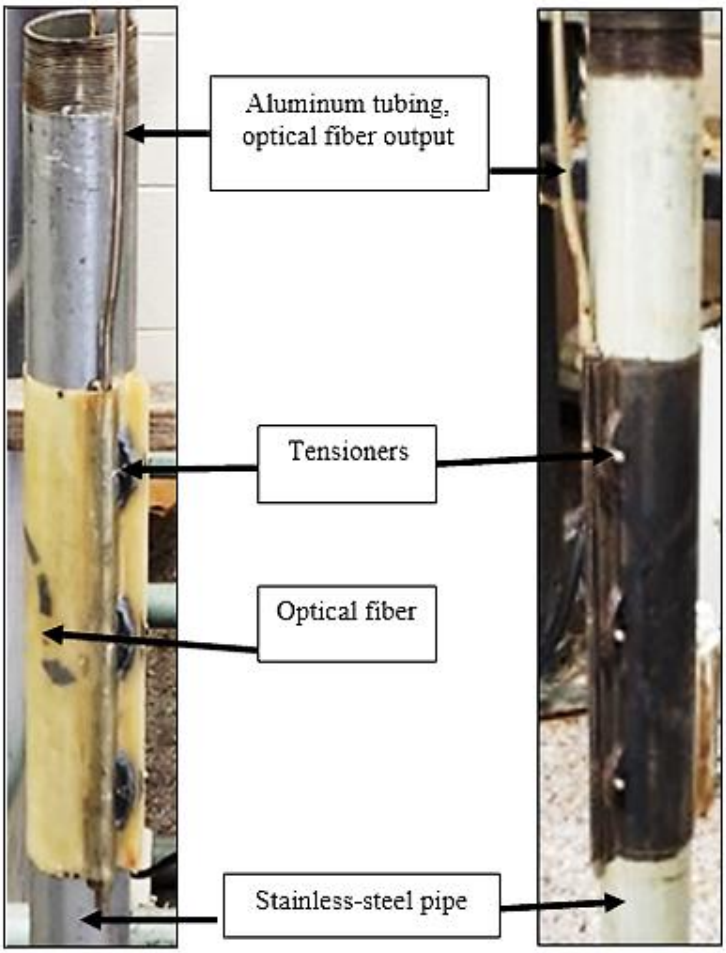

(a) (b)

Figure 15. Split-sleeve strainmeter on steel pipe (a) after initial fabrication and (b) after darkening caused by heating.

Another important part of this instrument is the tensioners. These are fixtures that are used to pull the edges of the sleeve together and put the sleeve in tension. Aluminum pieces with a threaded hole in the middle were bonded to the sleeve and bolts between the pieces were used for tensioning during initial tests. The aluminum pieces separated from the sleeve during tensioning, presumably because of the low bond strength of aluminum to epoxy. An alternative approach was developed to create tensioners from resin and fibers pressed in a mold.

The split-sleeve strainmeter was fabricated on a male mold designed to create a sleeve that fit onto casing with a close dimensional tolerance (Figure 16). The prototype was designed to fit on a 2-inch pipe as the well casing, so 2-inch pipe was used as the base for the mold. Steel pipe was used so the mold could be heated to set the resin. A 0.3 cm-wide slot was milled along the axis of the cylinder, and a thin piece of aluminum bar stock (0.3x2x33 cm) was fit into the slot and held in place with epoxy (JB Weld). The aluminum bar stock on the tube resembled a dorsal fin on a fish and will be referred to as the "fin." The pipe and fin were covered in kapton tape to prevent resin from adhering to them.

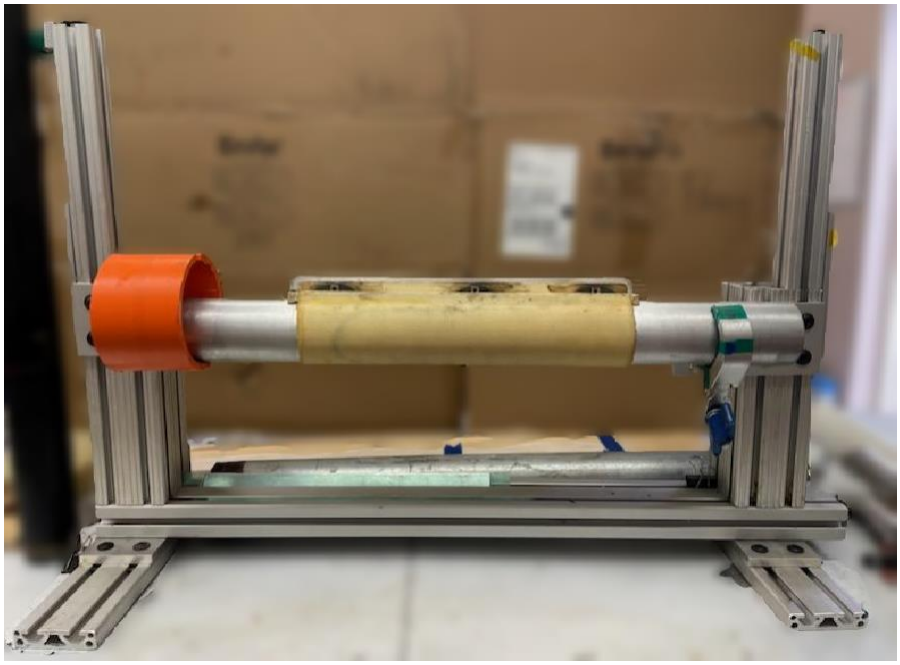

Figure 16. Split-sleeve strainmeter (yellow) on a mold set in a frame during fabrication.

Fabrication

The split sleeve strainmeter was fabricated as a hand lay-up laminate. The procedure involves first creating an inner layer that is cured and used as the base for the optical fiber. Two outer layers are then applied to protect the fiber and bond with the inner layer to create a continuous sleeve.

The fabrication procedure began by cutting sheets of plain weave, 0.23 kg/m fiberglass to a dimension of 30.5x40.6 cm. The fiberglass was placed on a flat surface and saturated with degassed resin. A silicone wiper was used to distribute the resin evenly and to remove excess resin. One end of the fiberglass was placed at the top of the fin on the mold and the wet fiberglass was placed onto the surface of the mold as it was rotated. The fiberglass was pushed into the corners where the fin meets the pipe, and the end of the fiberglass sheet extended up to the top of the far side of the fin. This created a continuous layer of fiberglass that wrapped from the top of one side of the fin around the mold to the other side. The layer was then heated with a heat gun at 150°C for 5 minutes, wrapped in a 31x41 cm Econostitch peel-ply and placed in a chamber pressurized to 25 psi, to cure for 24 hours. After curing the inner layer of sleeve, the base was removed from the pressure chamber and a hand lens was used to check for trapped air bubbles. A 0.635-centimeter diameter and 1-meter-long stainless-steel tube was placed along the fin on the cured inner layer. The tube was bonded to the base with high temperature rated epoxy putty (JB Weld). A narrow slow (30.5x1.5 cm) was cut along the axis of the tube where it joined the base. The tubing was used to protect the optical fiber as it passed from the data cable into the split sleeve.

A polyimide-coated optical fiber with 4 FBGs spaced 0.15 m apart was inserted into the stainless-steel tube, pulled through the slot and wrapped around the sleeve. The fiber was wrapped in a sigmoid pattern so the first three FBGs were oriented axially and spaced 120° apart on the sleeve. The fiber was then wrapped so FBG4 was oriented along the circumference and 4 cm above FBG 2. The fiber was glued down with epoxy adhesive (JB Weld). The axial strain sensors are located 120° from each other because the sleeve was designed to measure bending. The axial strain will vary around the circumference in a casing during bending and measuring

three uniformly distributed axial strains should yield the magnitude and direction of the bending strain. The fourth sensor, FBG 4, is located above the middle axial strain sensor, FBG 2, to measure circumferential strain during bending.

Two more pieces of fiberglass cloth were cut using the same dimensions as piece used the inner layer. Degassed resin was put in a 60 mL syringe and applied on one third of the sleeve surface. The resin was evenly distributed using a silicon brush and degassed again with a heat gun for 5 minutes. One outer layer was then progressively applied onto the sleeve and wet resin. The cloth was pushed down with a silicon wiper to accelerate the saturation process. Once saturation was complete, the mold was turned 120° so more resin could be applied on the sleeve and the cloth saturated. This was repeated one more time, so the first outer layer was completely covering the base and the optical fiber. A second outer layer was cut, and the process repeated. The mold was then put in the pressure chamber for 24 hours for curing.

The cured part consisted of a sleeve with two bands extending radially outward along the axial split in the sleeve (Figure 15a). The optical fiber entered the sleeve through the stainless-steel tube and was embedded between fiberglass laminates. The next step in the fabrication process was to create fixtures for tightening the sleeve onto a well casing. This was accomplished by drawing the two radial bands together using a bold and a nut. The circumference of the sleeve was slightly smaller than the circumference of the casing, by an amount equal to the thickness of the fin on the mold. As a result, there was a narrow gap, approximately 0.6 cm wide, when the sleeve was placed on a casing and pulling this gap together created tension in the sleeve. Initial tests showed that the radial bands flexed when drawn together with a bolt, so the bands were stiffened with dome-like pieces, called tensioners, that were bonded to the band and to the outer sleeve. A pair of tensioners were bonded on either side

of the two fins, with one side containing a threaded insert and the other a through-hole for a bolt. Three pairs of tensioners were arranged along the radial bands to create the overall tensioning structure. The height of the radial bands was then trimmed to the height of the tensioners. This caused the maximum height of the sleeve to be 1 cm.

The tensioners needed to be strong enough to support tightening, and they needed to be securely bonded to the sleeve. These requirements were met by casting the tensioners out of carbon fiber and epoxy resin (Figure 17). A mold was designed and fabricated with a 3D printer to create the small dome-like pieces used for tensioners. The pieces are 4 cm long at the base and 1 cm high at the highest point. They have cavity for a square nut to be embedded as a threaded insert.

The tensioners were made by mixing resin and 0.635-cm-long carbon fibers tows in a ratio of 3:2 (resin:fiber) by weight (Figure 17). The mold consists of two parts, a base shaped like a rectangular cavity, and an insert plunger with a curved shape that is pressed into the cavity to create the dome-like shape of the tensioner. Approximately 4 g of resin was poured in the mold base then 2 g of loose carbon fiber was added and mixed with the resin. More resin and fiber were added to a total of 16 g of resin and 11 g of fiber. Then the plunger was inserted and pushed down with a vise clamp. This expelled resin and air and compressed the fiber into the shape of the tensioner. It was left at room temperature for 24 h for curing. This process created a tough, strong composite part that was well suited to bonding to the sleeve. The technique for molding the part is based on a process called “carbon forging” developed in the automotive industry (Feraboli et al, 2011). Three tensioners were made following this carbon forging process. They were cut in half length wise, and each half was glued with epoxy adhesive on each

side of the radial bands. Holes were drilled in the tensioners and the band in order for bolts to pass through and tighten the sleeve.

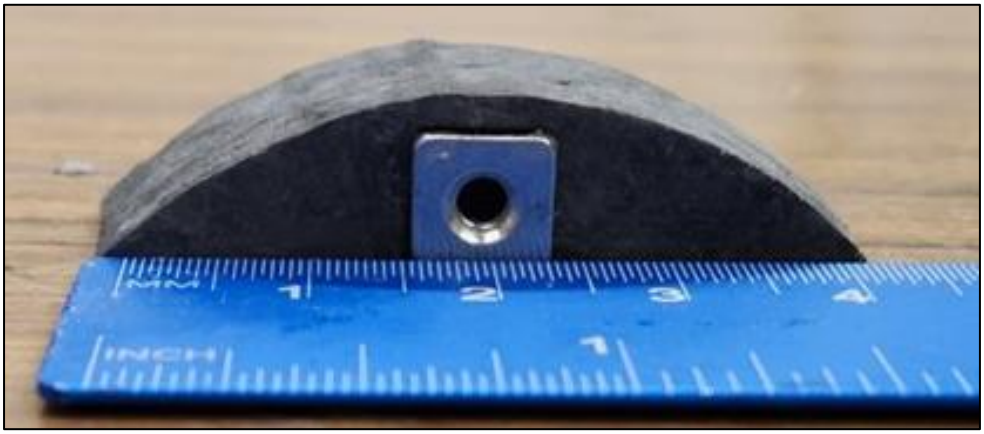

Figure 17. Dome-shaped tensioner made of forged carbon fiber tows and epoxy resin (black) with an embedded nut. Blue band is a scale.

The sleeve was heated at 120°C for 1 hour followed by 1 hour at 175°C to cure the epoxy once the tensioners were in place (Figure 15). The curing process strengthens the resin and is recommended by the epoxy resin manufacturer.

LABORATORY TESTING

The split-sleeve strainmeter was first tested in the laboratory for basic functionality and then a more comprehensive test was conducted to evaluate performance during heating and loading. The objective of the test was to evaluate the feasibility of measuring and interpreting strains at reservoir temperatures. The approach was to build an apparatus for heating and applying a load to a casing, and then attach the strainmeter to the casing and measure the response to applied loads at different temperatures defined in the constraints section. The responses obtained over a period of two months were then interpreted using simulations.

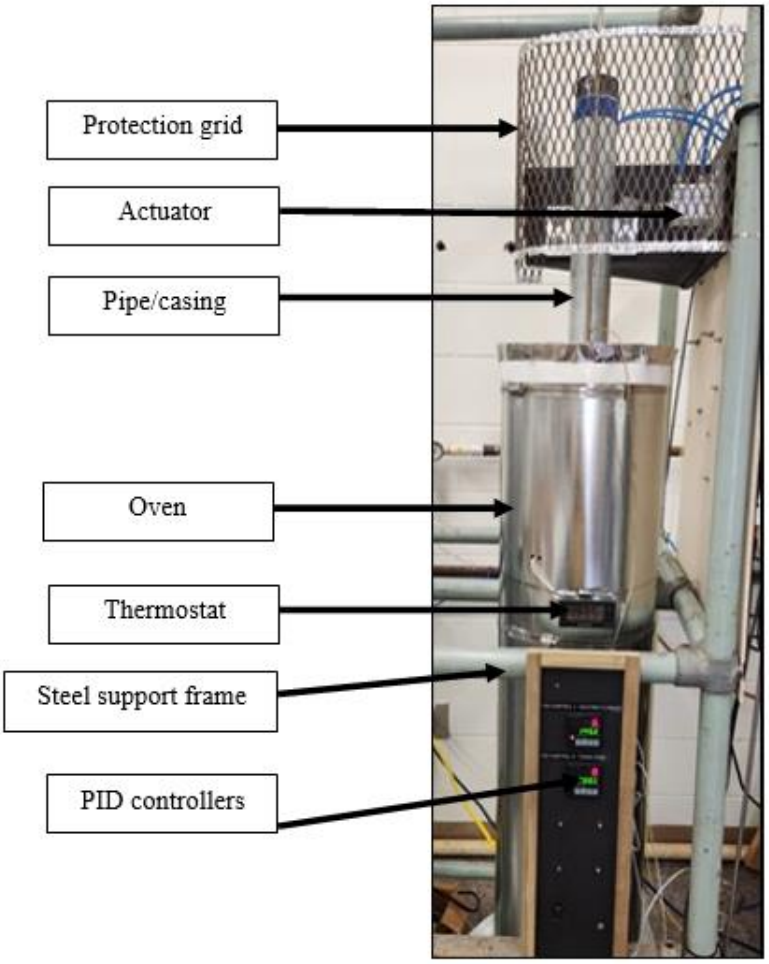

Figure 18. Oven with the split-sleeve strainmeter installed inside. A board with the PID controllers is installed on the steel frame to control the heating ribbon and oven temperatures.

Apparatus

The experiments were conducted using an apparatus based around a cylindrical oven controlled by two PID controllers. The oven was constructed using a 3-m-long 310 Watt BriskHeat heating ribbon wrapped around a 10-cm-diameter and 1.2-m long piece of sheet metal sold as an air duct, which formed the inner wall of the oven. The duct and heater were wrapped with a 7.6-cm-thick layer of fiberglass insulation. The insulated assembly was enclosed in a 25-cm-diameter duct that was capped and sealed with aluminum tape (Figure 18Figure 18. Oven with the split-sleeve strainmeter installed inside. A board with the PID controllers The

thermocouples for the PID controllers were placed in two different locations: (1) at mid-height of the oven taped on the inner wall with aluminum tape and (2) on the heating ribbon. The PID controllers use a three-parameter control loop to adjust and maintain a desired temperature. The PID controller that used the thermocouple attached to the heater was the primary control of the heater. The proportional, integral and differential parameters were tuned so temperature fluctuations in the oven were less than 5°C. The second PID controller was wired in series with the first and it used the thermocouple inside the oven. The upper set point of the second controller was set to 20°C above the set point of the primary controller. During a test with an early version of the oven, a malfunction caused the temperature to rise more than 100°C above the set point so the second PID was included to prevent overheating.

A 1.5 m-long, 2-inch steel pipe was mounted vertically inside the oven, and it served as a surrogate for well casing. The pipe was threaded into a flange that was bolted to two, parallel 2.5-cm-wide box tubes. The box tubes are 86.4 cm long and bolted to a steel frame approximately 31 cm above the floor. The oven was mounted to the steel frame and the flange holding the pipe was wrapped in insulation, enclosed in sheet metal and sealed with aluminum tape to form the bottom of the apparatus. The pipe extends through a seal and 0.3 m above the top of the oven (Figure 18). This configuration has the pipe/casing fixed at the bottom and free at the top, and it is enclosed in the oven from its base to a height of 1.2 m. The pipe/casing is intended to function as a vertical cantilever with a fixed base. However, the threaded joint between the pipe and the flange may be more compliant than a welded joint. Moreover, flexing of the 2.5-cm-wide box tubing probably caused the base to be more compliant when the pipe is loaded perpendicular to tubing than when it is loaded parallel to the tubing. These factors may cause the base to depart from a perfectly rigid structure.

The pipe/casing was loaded with forces applied transverse to its axis. This was accomplished using two air cylinders configured as linear actuators. They are placed at 90° from each other and can push the pipe/casing either parallel to, or perpendicular to the underlying box tubing (Figure 19). The actuators are controlled by two solenoid valves, which are controlled by three timers wired in series. The timers determine the duration and frequency of loading for each actuator (Figure 20).

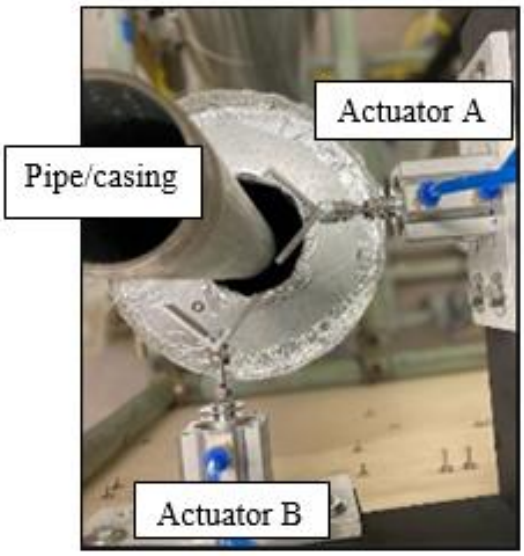

Figure 19. Top view of the pneumatic actuators used to apply transverse loads to the pipe/casing.

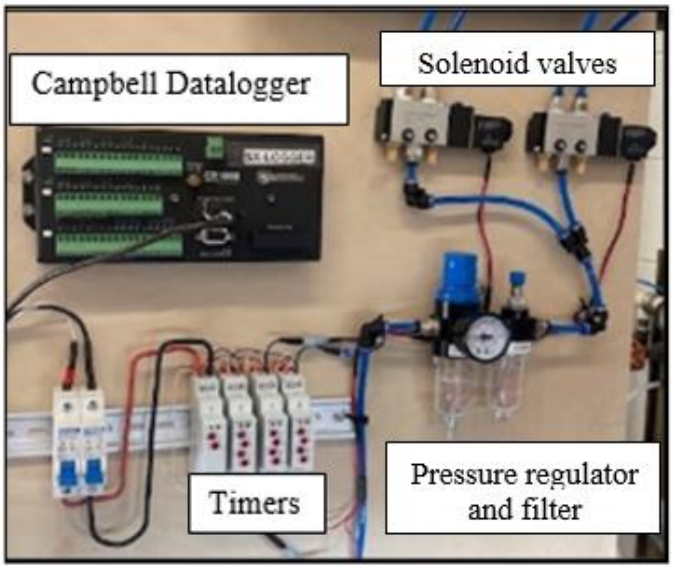

Figure 20. Pneumatic control panel for 2-axis loading system.

A V-shaped fixture is attached to the end of the actuator to center the pipe when the actuator is extended (Figure 19). The force and range of the actuators were adjusted to apply sufficient pressure to the actuator so it extended fully. This created a repeatable displacement condition for each cycle.

The actuator parallel to the box tubing was labeled Actuator A, and Actuator B was normal to it. The displacement at actuator A was 5 mm and it was 4 mm at actuator B (Figure 21).

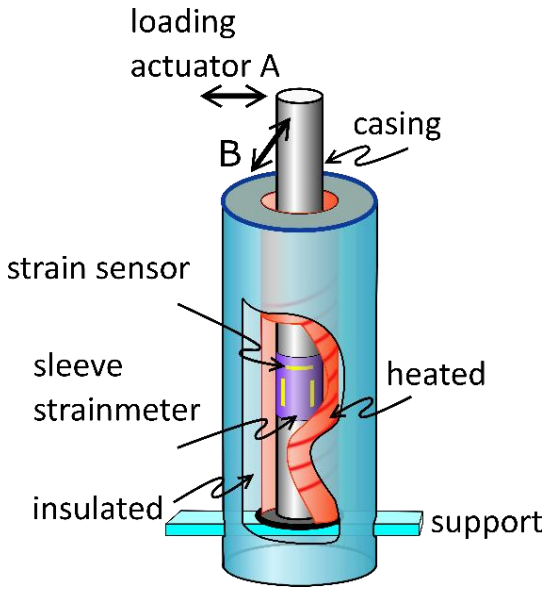

Figure 21. Schematic of experimental apparatus. The strainmeter (purple) is clamped on a steel pipe representing a casing and put in a heated oven. Actuators A and B load the pipe in two directions. Actuator A is parallel to the support of the casing.

Data analysis

The strain data were sampled every second by the FiSens interrogator and saved into a file. The files were divided into 4-day-long time periods and processed with a Python code that analyzes the data following steps.

1. Find all the loading cycles in the 4-day data. A convolution function (Arfken et al., 2013) was used to achieve that goal due to the step like shape of each loading cycle for all the FGBs and their apparent repeatability. A convolution peaks when the two compared functions (reference function and the time series) match the most (Figure 22).

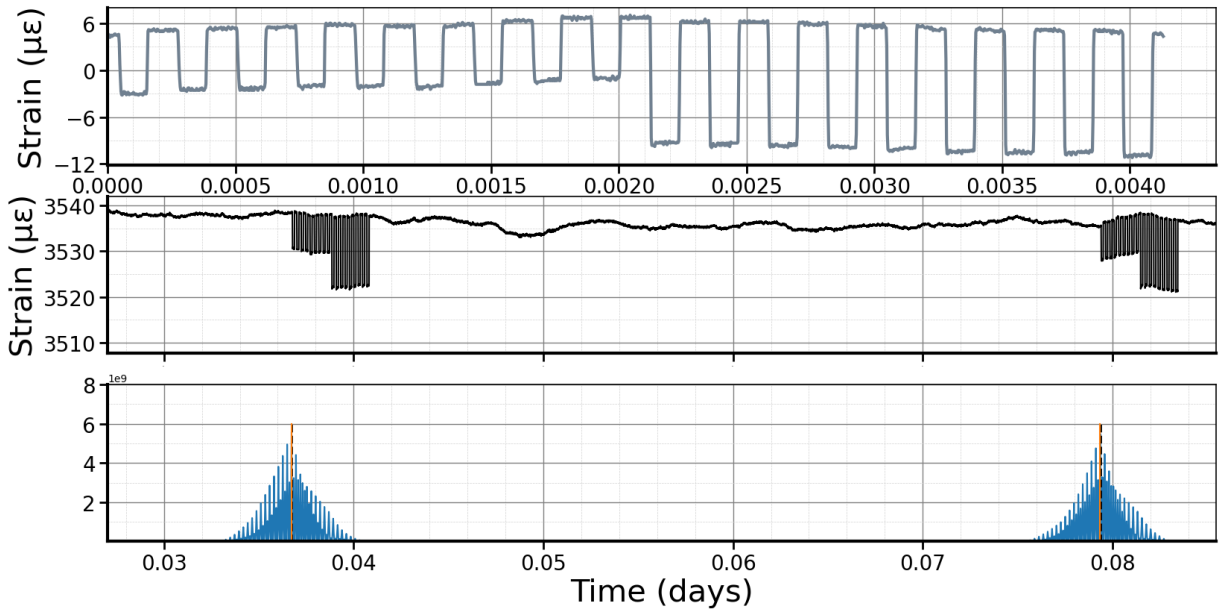

Figure 22. The reference function (top graph) is used to find loading cycle in the strain time series (middle graph). The convolution (bottom graph) peaks when the reference shape is detected in the time series.

2. Once the loading cycles are detected, average values of each plateau are calculated, and the average of a step is subtracted from the average of the baseline (Figure 23). To obtain an average strain amplitude value for loading A, the orange values were subtracted from the green values. The nine difference values obtained were used to calculate the mean. The same method was used to obtain an average strain value for loading B. The standard deviations for each 9-loading period were also calculated.

3. The number of average strain amplitude values per day was reduced to eight by summing six values at a time and dividing them by 6. The standard deviations for each 6-hour period were also calculated. The final processed dataset presented four average strain amplitudes per day for loading by actuator A and four values per day for loading with actuator B along with the standard deviations.

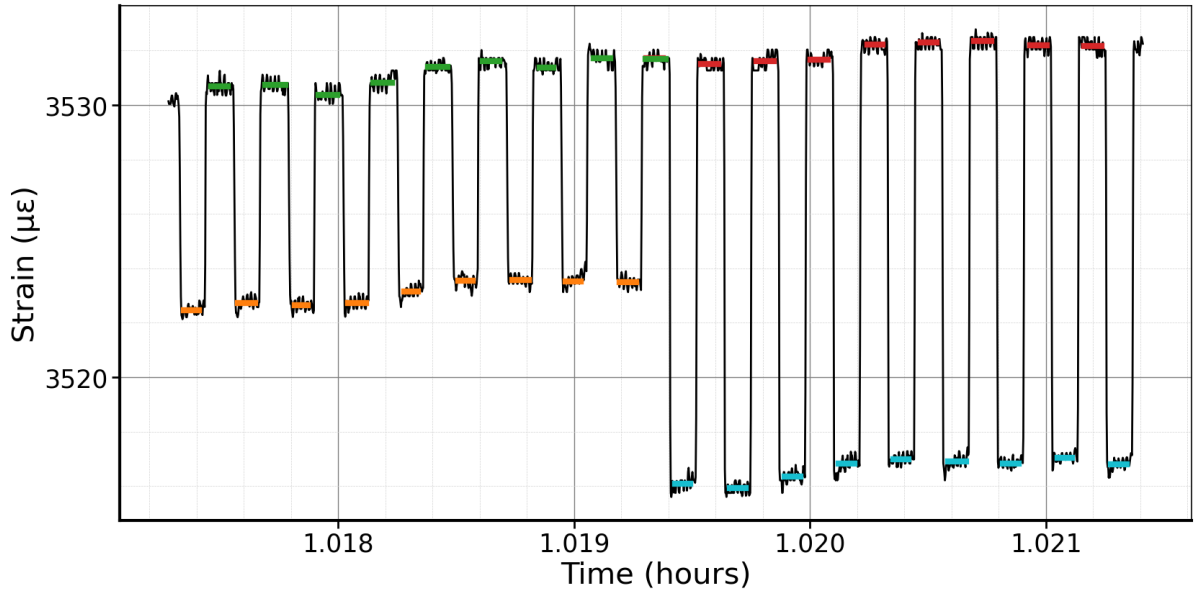

Figure 23. Strain time series with average values for each step shows as a colored line.

Proof-of-concept test

The objective of this task was to assess the operation of the instrument in the oven with load applied at regular time intervals.

The split sleeve strainmeter was mounted on the pipe/casing and the FBGs were oriented relative to the actuators as follows (Figure 24):

- FBG 2 and FBG 4 are aligned with air cylinder A and 90 degrees from air cylinder B.
- FBG 1 is 120 degrees from air cylinder A and 210 degrees from air cylinder B.
- FBG 3 is 120 degrees from air cylinder A and 30 degrees from air cylinder B.

The sleeve was tightened with a torque wrench set to stop tightening once the torque is 10 inch-pound. Three thermocouples were taped (Figure 24): at the base of the strainmeter (35.6 cm from the bottom of the pipe), at mid-height of the strainmeter (the same height as the FBGs and

50.8 cm from the bottom) and at the top of the strainmeter (66 cm). The oven was assembled, the seal was put in place at the top of the oven and, and the oven was turned on for 24 hours using a set point of 200°C.

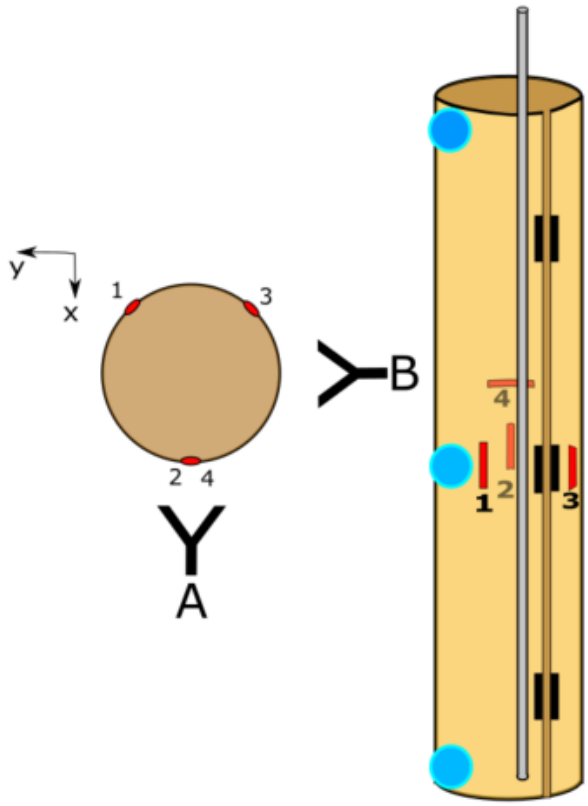

Figure 24. The split-sleeve strainmeter (left) with all four FBGs (red) was put on a pipe/casing (not represented here) and tightened with the tensioners (black rectangles). Three thermocouples (blue dots) were taped on the strainmeter. The vertical grey bar is the tube protecting the FBGs. A top view of the orientation of the FBGs and actuators is shown on the left.

When the oven reached the desired temperature, the actuators were turned on. They bend the pipe in different directions and cause responses from all the strain sensors. The sensors were compressed or extended depending on which actuator was used. Each actuator operated with a period of 20 sec (10 seconds of loading and 10 seconds of rest) for a total of 3 minutes (nine periods). Actuator A was activated for a 3-minute-long loading cycle, and then actuator B was activated for a 3-minute cycle and then they were both shut off for 54 minutes. This hour-long

sequence was repeated every hour for the duration of the test. This generated step-like strain time series, with nine steps up and nine steps down at each sensor (Figure 26).

The strain time series during heating of the oven were used to calculate an average coefficient of thermal expansion for the sleeve. When strain increases it indicates expansion meanwhile when it decreases it indicates shrinking. While the oven was reaching its set point, all four strains increased. The strain is a linear function of the temperature (Figure 25) and the slopes of the lines was used as the apparent coefficient of thermal expansion.

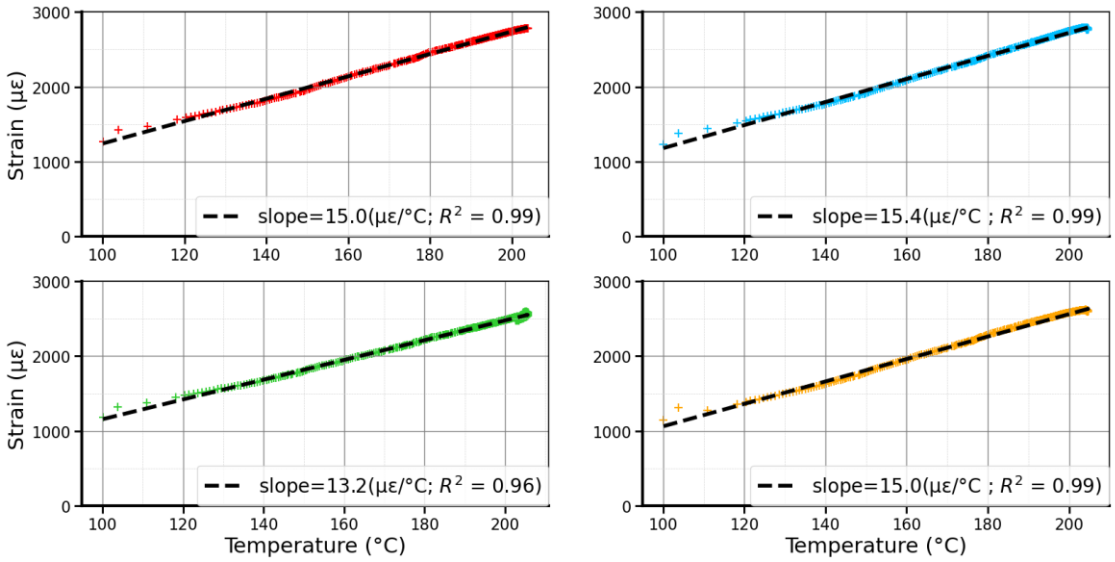

Figure 25. Strains observed as a function of temperature during heating of the oven from 100°C to 200°C. The four slopes used to calculate a coefficient of thermal expansion for the split-sleeve strainmeter.

The slopes range from 13.2 με/°C to 15.4 με/°C. The mean is 14.5° με/°C. The coefficient of thermal expansion for carbon steel ranges from 11 to 13 με/°C (Cverna, 2002). The sleeve falls within this range with a difference of 1 με/°C.

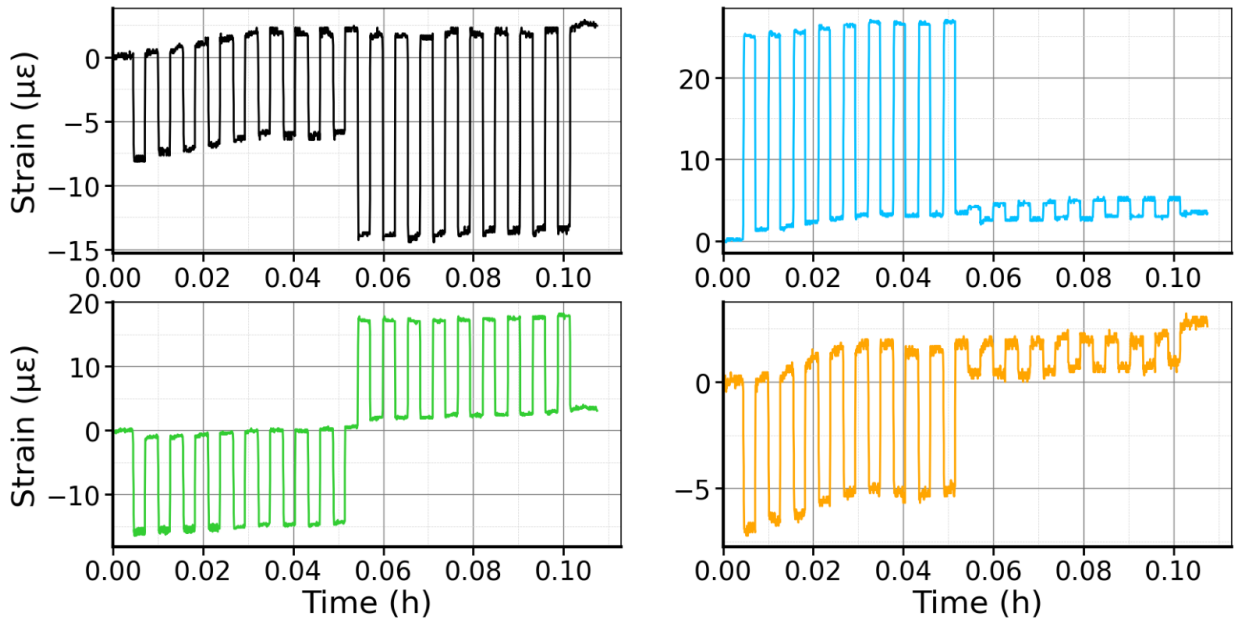

Figure 26. Baseline loading test where two loads were applied nine times resulting in strain changes. Measured data for each FBG is represented: FBG 1 (black), FBG 2 (blue), FBG 3 (green) and FBG 4 (circumferential) (orange).

During the loading part of the test, the strain amplitudes for each FBG differ from the others and the signals were also different depending on the actuator applying force on the pipe (Figure 26).

The amplitude of the steps range from -14 με to +23 με. The amplitudes were consistent when a load was applied from a particular actuator and measured by a particular FBG. The strain amplitudes for each FBG differ from the others and the signals were also different depending on the actuator applying force on the pipe (Figure 26). When strain increases it indicates tension and when it decreases it indicates compression.

The pipe bends in response to the transverse load from an actuator and this will cause the axial strain during bending to vary in magnitude and sign around the circumference of the pipe. Compressive axial strain will occur on the side opposite the actuator and tensile axial strain

occurs on the same side. The circumferential strain also changes during bending. This is why different strain magnitudes are measured at the different sensors.

All FBGs except FBG 3 recorded the same sign for their change in amplitude during loading A and B. The biggest change occurred at FBG 2 where strains increased by 23 με during loading by actuator A. The smallest change occurred at FBG 2 and FBG 4 where strains increased and decreased by 2.5 με during loading by actuator B. The signs of the strains for FBG 3 are opposite for each actuator but their amplitudes are the same. Loading by actuator A caused a decrease of approximately 15 με and loading by actuator B caused an increase of 15 με.

These results show that the coefficient of thermal expansion of the split-sleeve is within the same range as the coefficient of thermal expansion of stainless steel. They also show that the apparatus can create strains that are repeatable and consistent, and the strainmeter can measure strains that result from an applied transverse displacement. This demonstrates basic proof-of-concept.

Durability test

The objective of this experiment is to evaluate the feasibility of characterizing strains over extended duration at geothermal reservoir temperatures. These results will be used to assess the durability of the strainmeter.

After a successful proof-of-concept test, the oven was turned off to let the sleeve cool down while still in the oven. The experiment to test the durability of the instrument started once the sleeve was back to room temperature. The temperature of the oven was set to 100°C for 57 minutes, it was increased to 200°C for 29 days and then it was set to 230°C for 29 days. Variations of temperature were ± 5°C from the set point throughout the test (Figure 27).

Those temperatures were chosen because they are hotter than 150°C, the temperature defined as *required* for the strainmeter to function and hotter than to 225°C, the temperature in well 16A at Utah FORGE and the desired temperature for the functionality of the strainmeter.

The axial strain increased abruptly by 3200 to 3600 με and the circumferential strain increased by 4200 με as a result of heating from ambient (20°C) to 200°C (Figure 27). The strains changed gradually over the next few weeks, and after 25 days of heating the range of the axial strains decreased from 400 με (3200 to 3600 με) to roughly 15 με (3530 and 3545 με). The circumferential strain decreased to approximately 3590 με (Figure 27). After increasing the temperature to 230°C on day 31, all the strains increased by about 500 με. After peaking, the axial strain measured by FBG 1 decreased at a faster rate than the strain measured by FBG 2 and FBG 3 between day 31 and day 40. The range of the axial strains was about 100 με (3500 and 3600 με) at the end of the test. The circumferential strain that was at 3590 με reached a maximum value of 4500 με before decreasing to 4400 με. This is consistent with an effective CTE of 1.96×10^{-5} 1/°C in the axial, and 1.99×10^{-5} 1/°C in the circumferential directions.

The amplitude of the steps ranged from -28 με to +25 με (Figure 28). Positive strain is tension, negative is compression. During the 200°C and the 230°C heating periods, the amplitudes of the strain steps varied slightly with a coefficient of variation generally less than 0.5 (Table 1).

The axial strain varies in sign and magnitude around the circumference of the pipe during bending. Compression and tension happen at different locations of the pipe depending on the actuator working. The circumferential strain also changes during bending. This caused the different sensors to measure different strain magnitudes (Table 1 and Figure 28).

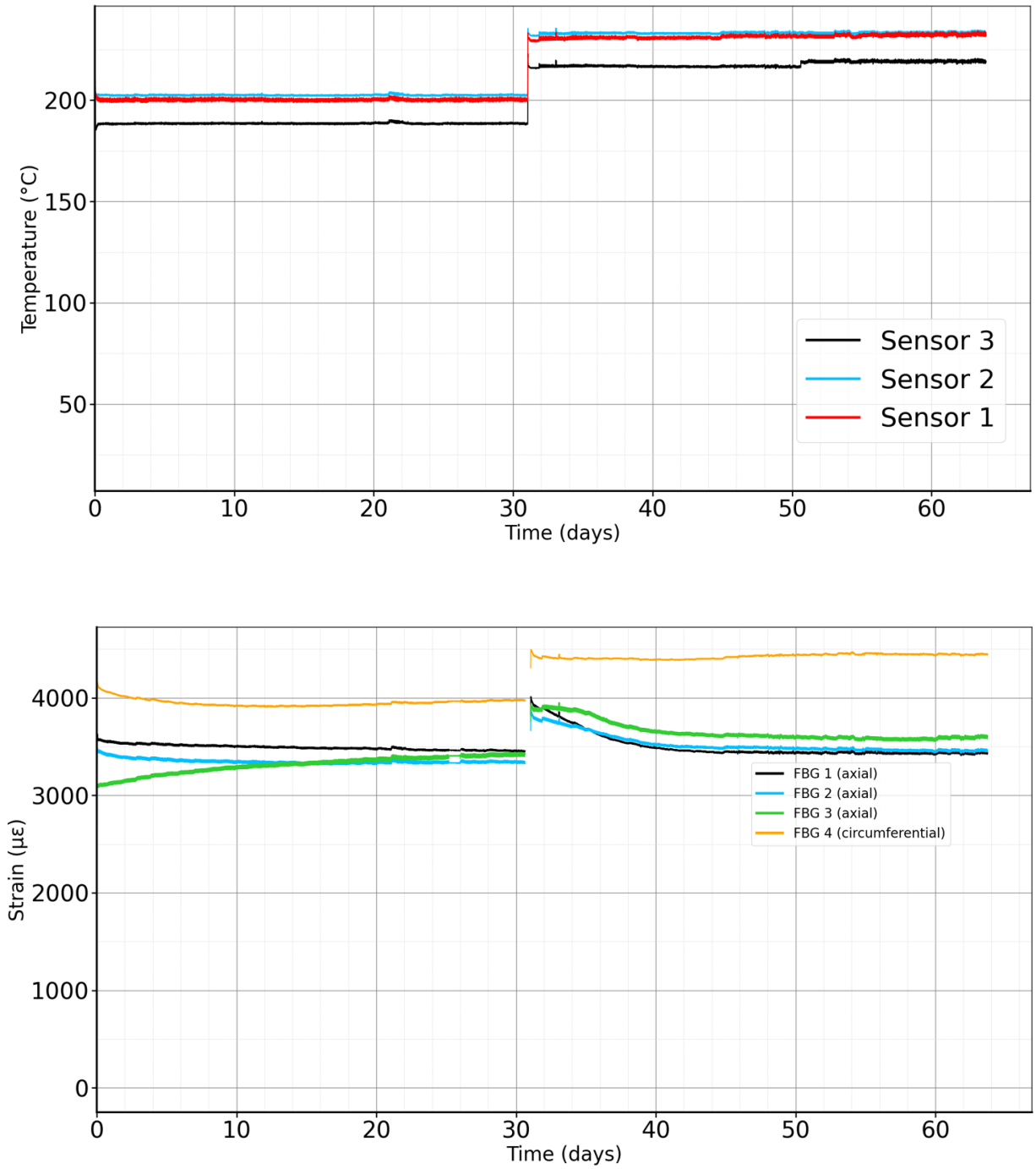

Figure 27. Time series of the temperature and strain during the durability test. The set point of the heater was increased from 200 to 230°C on day 31. Zero strain is at room temperature. Strain and temperature increase at the beginning of the test is too rapid to be shown at this scale.

Table 1. Mean and standard deviations of the amplitude of strain during the duration of the test for FBGs 1 through 4 and Loads A and B.

FBG+Load	mean	std dev	CoV
1A	-4.23	2.29	-0.54
1B	-9.13	4.06	-0.44
2A	20.7	2.59	0.13
2B	1.49	0.28	0.19
3A	-21.7	3.42	-0.16
3B	9.63	2.47	0.26
4A	-7.26	1.32	-0.18
4B	-0.99	0.26	-0.26

The average strain amplitudes during each loading cycle changes by less than a few με to roughly 13 με throughout the duration of the test (Figure 28 and Figure 29). The biggest change occurred at 3A (FBG number and the actuator applying the load) and 3B during the 200°C test where strains decreased by 13 με. At 230°C the trend for 3A and 3B is reversed, the strains increased by 8 με in both cases. The opposite effect occurs at FBG 1. Strain amplitudes increased over the duration of the 200°C test by approximately 6 με for 1A and 1B, and then after the temperature was increased to 230°C, the strain decreased by 7 με during loading 1A and 1B. The amplitudes for 2B and 4B were nearly constant but 2A and 4A varied by 2 to 4 με (Figure 28 and Figure 29).

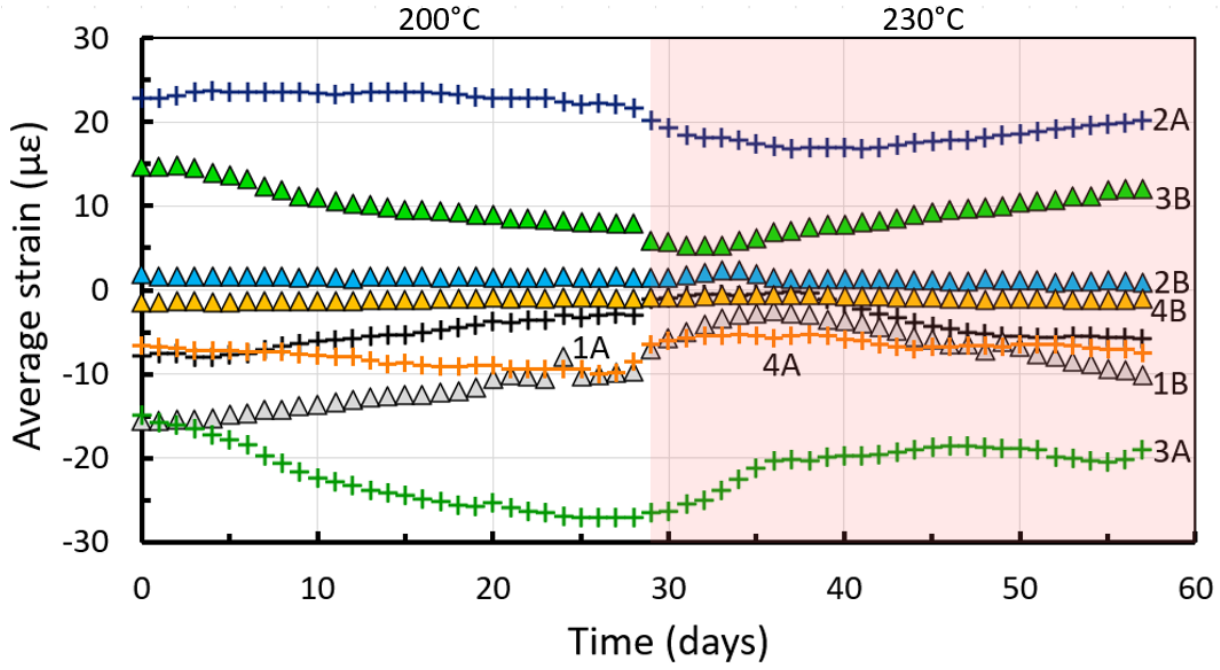

Figure 28. Daily averages strains during periodic load tests measured with split-sleeve strainmeter as a function of time during heating at 200°C and 230°C. The color code is consistent with Figure10: Black -FBG1, blue – FBG2, green – FBG3 and orange – FBG4. Load A: a + symbol, load B: a triangle symbol.

SIMULATIONS

Data from the tests show the responses were generally repeatable, and the sign of the strain was consistent with the expected bending that resulted from the applied loads. These results are encouraging, but additional analyses are required to achieve the goal that the strain can be *measured* and *interpreted*. It was infeasible to measure strain independently during the experiments, so direct verification of the measurements from the strainmeter was unavailable. In the absence of confirmation data, a numerical simulation was developed to evaluate the strain data. The goal of the simulation was to assess how closely the experimental data matched expected values, and to evaluate the feasibility of interpreting the experimental data.

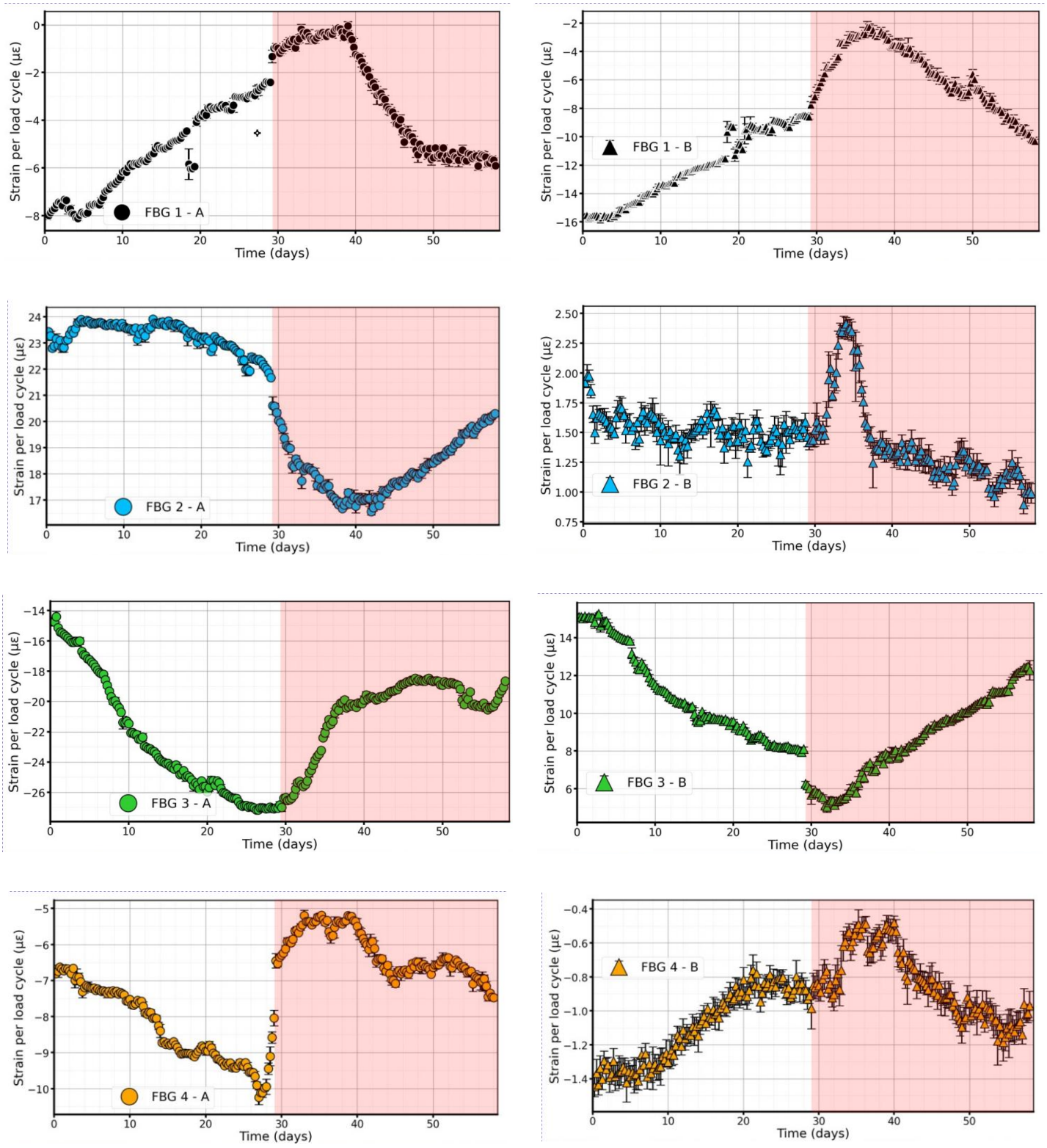

Figure 29. Four-hour average strains (with one standard deviation as error bars) during periodic loading tests measured by split sleeve strainmeter. White background = 200°C. Red background = 230°C. Strains from load A in left column, load B in right column. These plots show the data in Figure 28 in more detail.

Conceptual Model

The simulation will be based on a conceptual model that considers the pipe/casing loaded transversely by actuators. The initial assumption was that the base of the pipe/casing was rigid, but preliminary analyses indicated that the base was flexing and this may have affected the results. The conceptual model was expanded to include the pipe/casing, the flange, and the two box tubes (Figure 30). The flange was bolted to the box tubing and the ends of the box tubing were bolted to a larger steel frame. As a result, it was assumed the displacement of the ends of the box tubing was fixed.

The actuators used in the experiment were completely extended, which created a fixed displacement of the end of the pipe/casing. The displacement for Load A was 5 mm and it was 4 mm for Load B.

All the components were made from carbon steel. The Young's Modulus was assumed to be 200 GPa and Poisson's ratio was 0.3 (Gandy, 2007). Three scenarios will be considered to evaluate different effects:

- Baseline: The properties of the three parts are uniform and the displacements are uniaxial.
- Scenario 1: This scenario was developed to reduce the magnitude of the strains in the simulation. It considers a junction between the pipe and flange that is compliant. This could be a result of the material removed at the threads or slight loosening at the threaded junction. The compliant junction was represented using E = 0.7 GPa at the junction (light purple in Figure 31).

- Scenario 2: This scenario was developed to explain the difference between strains during 1A and 3A. This scenario includes 2 mm of displacement in the -y direction during Loading A.

The primary data from the experiments is a time series of strains during loading and unloading cycles in the A and B directions (Figure 26), so the conceptual model includes this type of transient loading. The transient experimental data were then analyzed to evaluate the magnitude of the displacement caused by an applied load. These values changed during the experiment, as shown in Figure 28 and Figure 29, but it will be assumed that each data point in those plots can be represented by a steady-state analysis showing the displacement caused by an applied load.

Numerical model

A numerical model of the apparatus was built to evaluate the strain data obtained experimentally. Pieces from the apparatus were replicated in COMSOL so the numerical model resembled the laboratory apparatus.

Geometry and properties

Three main geometries were designed to build the numerical apparatus representing (1) the pipe/casing, (2) the flange and (3) the box tubing that are part of the support frame. The flange was made by using a SolidWorks file obtained from McMaster.com. The pipe/casing was created using the difference between two cylinders to form a hollow cylinder. The box tubings are two long cuboids. Those geometries are joined with a continuity constraint so when the displacement is applied on the pipe/casing, it continues where the geometries meet.

The properties were divided into two zones: (1) the pipe/casing, the flange and the support structure and (2) the threads on the pipe (Figure 30 and Figure 31). The focus of the numerical simulation is to evaluate the strain during loading of the pipe/casing. This implies doing a study of the elasticity of the apparatus, so the properties defined for the two zones were the Youngs modulus and Poisson's ratio. Zone One has a Youngs modulus of 200 GPa and a Poisson's ratio of 0.3. Those values are the same as the values defined for carbon steel (Gandy, 2007). Zone Two is considered more compliant than steel due to the presence of threads. A Young's modulus of 0.7 GPa was used for Zone Two.

Physics

The simulation assumes the apparatus deforms as a linear elastic solid. Conservation of momentum requires

$$\nabla \cdot \sigma = 0 \tag{1}$$

where σ is the total stress tensor. Quasi-static conditions are assumed and body forces are ignored. The stresses are related to strains through Hooke's Law as

$$\begin{aligned}
\sigma_{xx} &= 2G\varepsilon_{xx} + \lambda\varepsilon_{kk}\sigma_{ij} \\
\sigma_{yy} &= 2G\varepsilon_{yy} + \lambda\varepsilon_{kk} \\
\sigma_{zz} &= 2G\varepsilon_{zz} + \lambda\varepsilon_{kk} \\
\sigma_{xy} &= 2G\varepsilon_{xy} \\
\sigma_{xz} &= 2G\varepsilon_{xz} \\
\sigma_{zy} &= 2G\varepsilon_{zy}
\end{aligned} \tag{2}$$

which can be written in a more compact form using index notation

$$\sigma_{ij} = 2G\varepsilon_{ij} + \lambda\varepsilon_{kk}\delta_{ij} \tag{3}$$

where δ_{ij} is the dirac delta and G is the shear modulus, and λ is Lame's constant. These constants are related to Young's Modulus, E, and Poisson's ratio, ν, using

$$\lambda = \frac{E\nu}{(1+\nu)(1-2\nu)}$$
$$G = \frac{E}{2(1+\nu)} \tag{4}$$

The normal strains are

$$\varepsilon_{xx} = \frac{\partial u_d}{\partial x}$$
$$\varepsilon_{yy} = \frac{\partial v_d}{\partial y} \tag{5}$$
$$\varepsilon_{zz} = \frac{\partial w_d}{\partial z}$$

and shear strains are

$$\varepsilon_{xy} = \frac{1}{2}\left(\frac{\partial u_d}{\partial y} + \frac{\partial v_d}{\partial x}\right)$$
$$\varepsilon_{yz} = \frac{1}{2}\left(\frac{\partial v_d}{\partial z} + \frac{\partial w_d}{\partial y}\right) \tag{6}$$
$$\varepsilon_{zx} = \frac{1}{2}\left(\frac{\partial w_d}{\partial x} + \frac{\partial u_d}{\partial z}\right)$$

where the displacement vector is

$$\mathbf{u} = u_d\mathbf{i}_x + v_d\mathbf{i}_y + w_d\mathbf{i}_z \tag{7}$$

The volumetric strain is given by

$$\varepsilon_{kk} = \varepsilon_{11} + \varepsilon_{22} + \varepsilon_{33} \tag{8}$$

Boundary conditions assumed a traction free surface everywhere except at the ends of box tubing (Figure 30) where

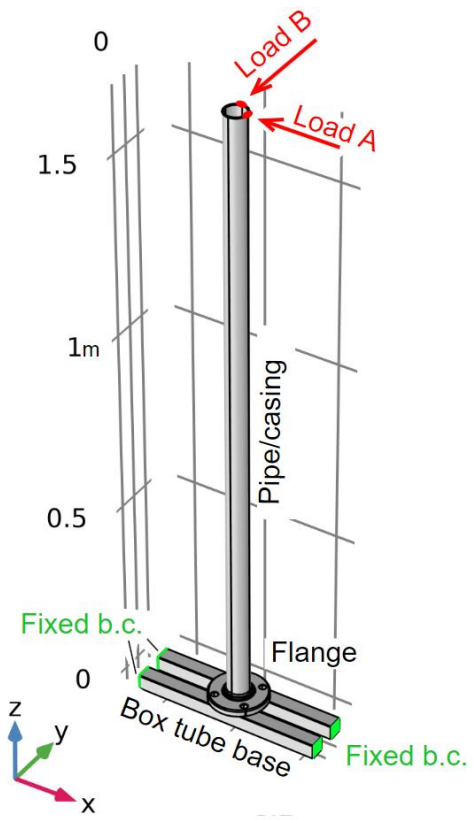

Figure 30. Geometry and boundary conditions used in the simulations. Components include pipe/casing, flange and box tubing with continuity where they contact. All surfaces are traction free except the ends of the box tubing, which are fixed displacement. Load A is a specified displacement in the -x direction, Load B is a specified displacement in the y direction.

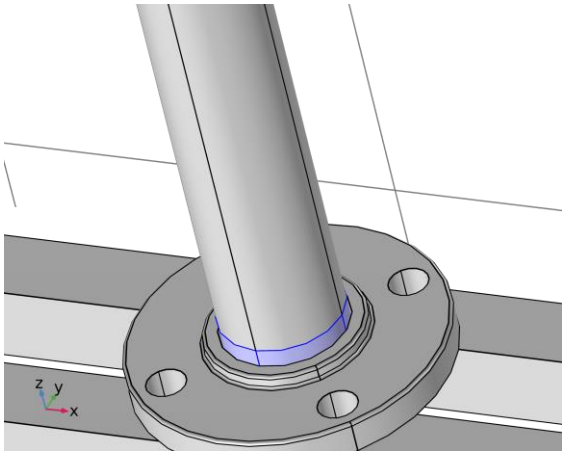

Figure 31. Detail of the pipe/casing and flange. Young's modulus of the zone where the pipe meets the flange (light purple) was reduced to simulate the effect of a soft junction between the pipe and flange in Scenarios 1 and 2.

$$\mathbf{u} = 0 \tag{9}$$

Boundary conditions for the Baseline Scenario and Scenario 1 are

Load A: $u_d = -0.005m$ at pt A (Figure 30)

Load B: $v_d = 0.004m$ at pt B (Figure 30)

Boundary conditions for the Scenario 2 are

Load A: $u_d = -0.005m$ at pt A (Figure 30) and $v_d = -0.002m$ at pt B (Figure 30).

Load B: $v_d = 0.004m$ at pt B (Figure 30)

Mesh

The mesh was made with 53,452 tetrahedra (Figure 32) with a size range of 0.031-0.172 m.

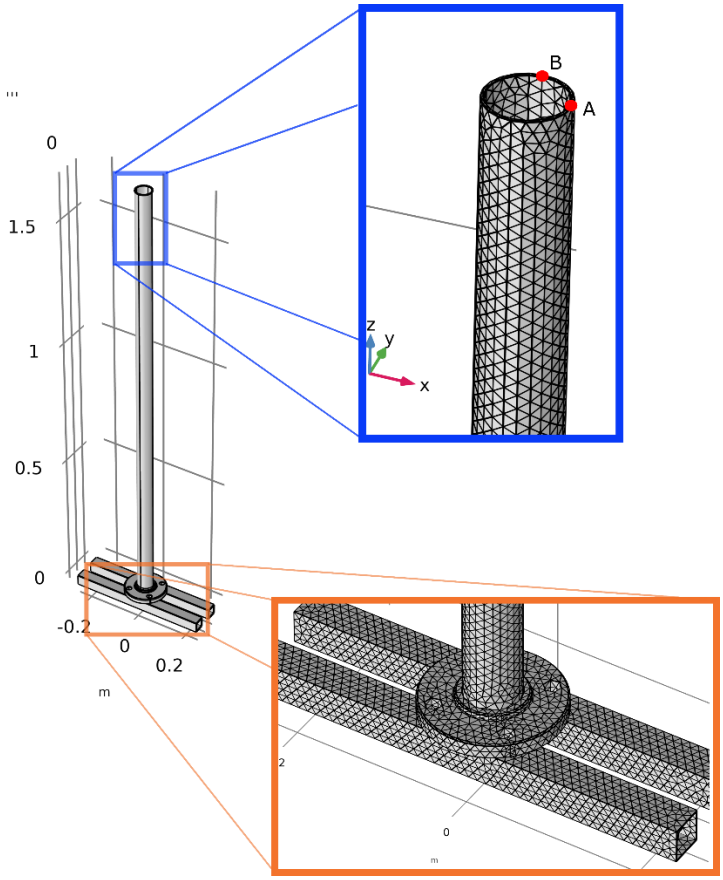

Figure 32. Tetrahedral mesh used to discretize the geometry.

Results

The baseline scenario was evaluated using a transient analysis that considered two cycles of A followed by two cycles of B loading. The specified displacement was applied for 10 seconds and released for 10 seconds, following the experimental conditions (Figure 26). Measurements were included in the simulations at the same location as the FBGs in the strainmeter.

The predicted strains at the FBG locations are periodic square waves with magnitudes that vary with the location of the measurement and the load (Figure 34a). The largest strain response is a magnitude of more than 80 με and it occurs at FBG2 during loading A, and the strains are equal and less than -40 με at FBG1 and 3 during loading A (Figure 34a).

The magnitudes of the strain responses in the simulations relative to each other are similar to the experimental data, but the simulated magnitudes are roughly three times larger than those in the experiments (Figure 27, Table 2). This indicates that the curvature of the pipe/casing in the simulations is greater than it was in the experiments. One explanation for this is the displacements used for the boundary conditions are larger than the actual displacements. The displacements used in the simulations are based on measurements, however, so this seems unlikely. Another possibility is that the joint between the pipe and the flange is more compliant than assumed in the baseline model. To understand this effect, consider a joint that can flex with no resistance at all. In this case, applying displacement for Load A would cause the pipe/casing to pivot about the joint without bending at all. The axial strains measured by the strainmeter would be zero. This is an end-member case, but it is possible that the actual joint is more compliant than the baseline because of the threaded connection between the pipe and flange. The wall of the pipe is thinner at the threads and will therefore be more flexible. Moreover, the

threads are designed to seal against internal pressure, but they are in contact over a small surface area and this will make the joint flexible.

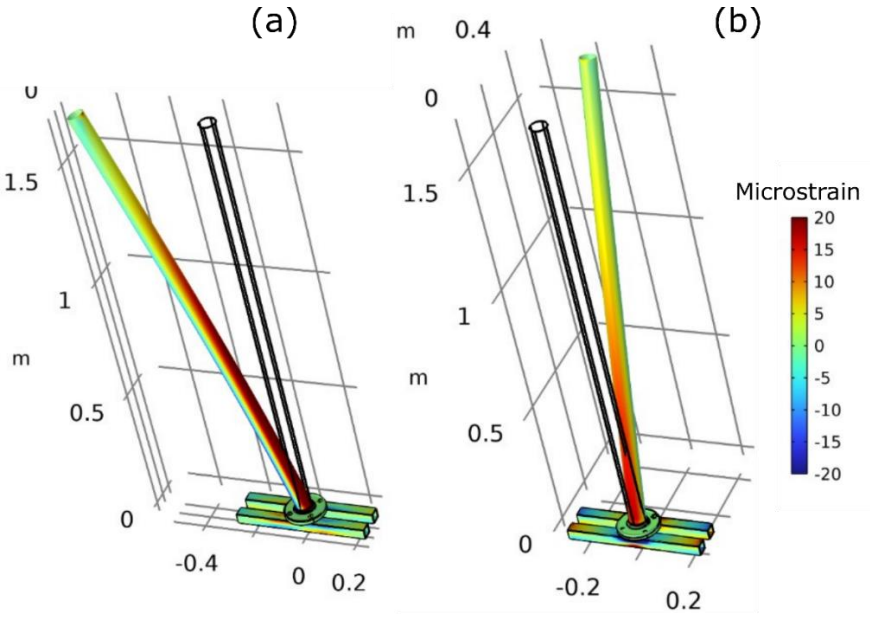

Figure 33. Perspective view of pipe/casing, flange and box tubing with vertical strain as color during (a) Load A and (b) Load B. Apparatus is displaced with exaggeration of 100x. Legend is vertical strain in units of microstrain.

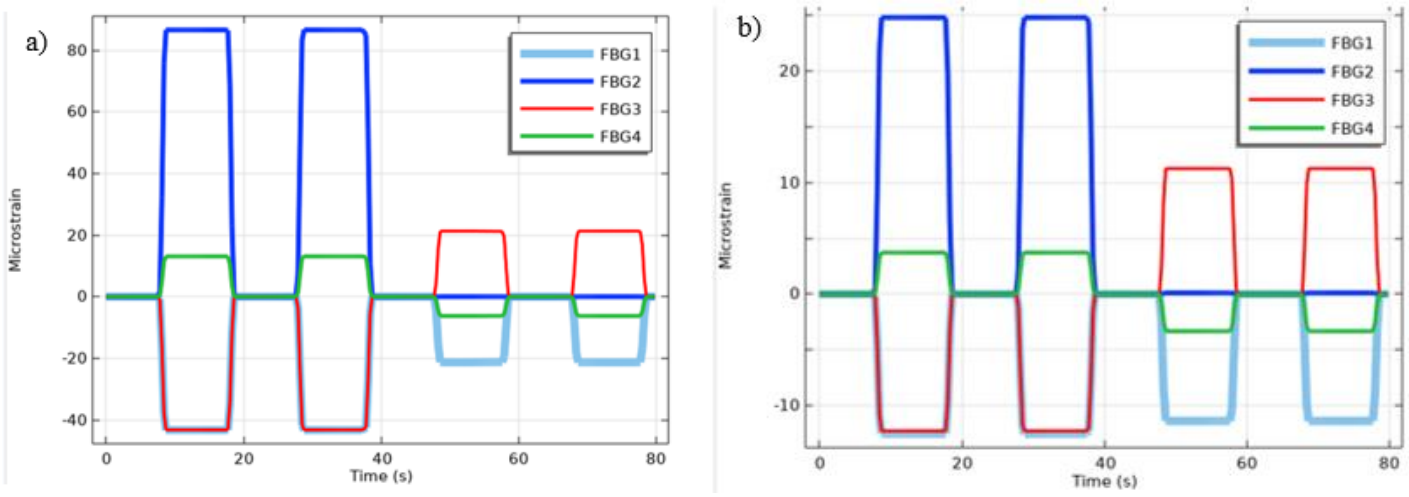

Figure 34. Strain as a function of time at 4 measurement locations similar to the locations of FBGs in the strainmeter during the experiment. Load A was applied twice and then Load B. (a) Baseline scenario, (b) Scenario 1.

To evaluate the hypothesis that the pipe/flange joint was flexing, a zone at the base of the pipe was introduced where the Young's modulus could be set independently of *E* for the rest of the apparatus. This is called Scenario 1 above. Young's modulus of the joint was adjusted until the axial strains in the simulation were similar to those from the experiments. The data in Table 2 were obtained using E = 0.7 GPa for the effective Young's modulus of the joint. This change reduces the magnitudes of the strain steps (Figure 34b) by approximately a factor of 3. So, for example, the simulated amplitude of 2A is 24 με, which is within one standard deviation of the mean value from the experiments (Figure 34; Table 2). The strains are reduced because the flexibility of the joint reduces the curvature of the pipe (Figure 35).

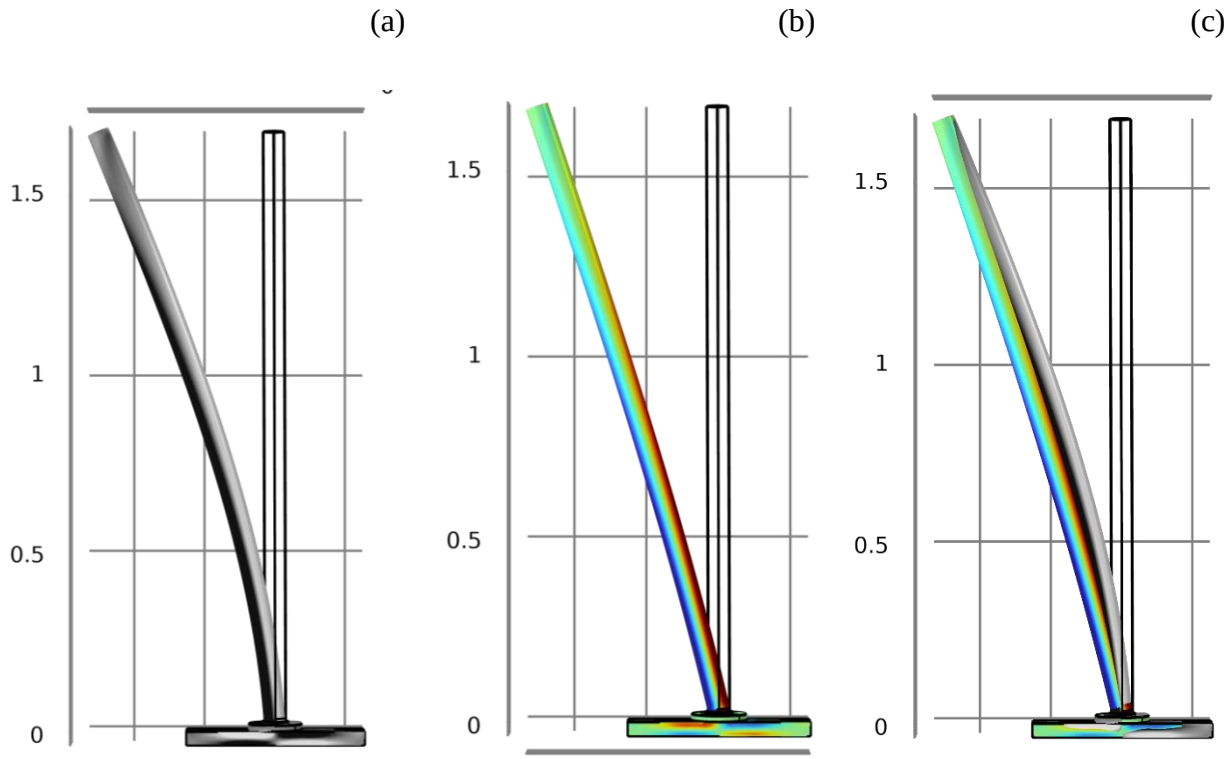

Figure 35. Deformed apparatus (100x exaggeration) viewed in y direction. (a) Baseline case. Vertical strain shown as grey scale. (b) Scenario 1 with a compliant joint. Vertical strain as color scale. (c) Images from (a) and (b) superimposed to highlight difference in curvature.

The relative error between the simulated and observed strains is less than 0.2 for four of the datasets for Scenario 1, which is a marked improvement compared to the Baseline scenario (Table 2).

Table 2. Strain magnitudes in response to load from experimental data for the first 20 days and from simulations. Baseline simulation considers uniform material, Scenario 1 considers a compliant junction between pipe and flange, Scenario 2 considers a compliant junction and a small component of displacement in -y direction during Load A. std dev= standard deviation, CoV = coefficient of variation, R.E.=relative error of simulations and data. Shaded cells are where R.E. > 0.2.

Data				Simulations					
FBG+Load	mean	std dev	CoV	Baseline	R.E	Scenario 1	R.E.	Scenario 2	R.E.
1A	-6.23	1.29	-0.21	-43	-5.90	-12	-0.93	-6.8	-0.09
1B	-13.63	1.38	-0.10	-21	-0.54	-11	0.19	-11	0.19
2A	23.46	0.28	0.01	86	2.67	24	0.02	24.6	0.05
2B	1.61	0.09	0.06	1E-03	-1.00	1E-04	-1.00		-1.00
3A	-21.22	3.63	-0.17	-43	-1.03	-12	0.43	-17	0.20
3B	11.61	2.09	0.18	21	0.81	11	-0.05	11	-0.05
4A	-7.87	0.82	-0.10	-26	-2.30	-7.5	0.05	-7.4	0.06
4B	-1.24	0.17	-0.13	-0.1	0.92	0	1.00		1.00

The relative error of four of datasets in Scenario 1 are greater than 0.2, so additional factors were considered to account for this error. The magnitudes of 2B and 4B in the data (1.6 and -1.2 με) are smaller than the other datasets, and the simulation predicts that these values should be zero. This causes a high relative error, but the absolute error is small, so it appears that the simulation predicts these values with sufficient accuracy.

The magnitudes of 1A and 3A are predicted to be equal in the Baseline and Scenario 1 because FBG1 and FBG3 are symmetric about the line of Load A (Figure 24). However, the magnitude of 1A observed in the data (-6.2 με) is greater than, and that of 3A (-21 με) is less than the predicted value of -12 με. This suggests that a factor that breaks the symmetry of the apparatus is responsible for the error. One possibility is that FBG1 and FBG3 are not symmetric

about the line of Load A (-x axis). This could occur if the strainmeter was unexpectedly rotated, or if the locations of the FBGs where shifted during fabrication of the strainmeter. These factors would cause 1B to differ from 3B, but the data indicate that these values are essentially the same (within 1 standard deviation).

Another possibility is that there is a small displacement in the -y direction during Load A. This could occur, for example, if the V-shaped fixture at end of the actuator (Figure 19 and Figure 24) was displaced slightly from the center line so one side of the V contacted the pipe before the other side. To evaluate this possibility a displacement of -0.002 m in the y direction was included in Loading A, along with the displacement of -0.005 m that was used in the other scenarios. This decreases the strain at 1A and increases it at 3A. The relative error of the resulting strains (Table 2) are all less than 0.2 (ignoring the R.E. at 2B and 4B as justified above).

CONCLUSION

Numerical simulations set up to resemble the experimental apparatus predict strains that are similar to the experimental measurements. The magnitudes of the baseline simulations are approximately three times larger than the experiments, but this can be explained if the joint between the pipe/casing and the flange is more compliant than the idealized case assumed in the baseline. The observed strains in 1A and 3A differ with a factor of 3, but they should be equal because the loading is symmetric about the two points. This effect can be explained by a slight misalignment of the loading actuator. These findings suggest data from the split-sleeve strainmeter are measuring the actual strains in the pipe casing, and the values can be interpreted to improve understanding of the experimental conditions when strains are applied at temperatures similar to geothermal reservoirs.

Chapter Four: DIRECT-PUSH STRAINMETER

This chapter presents the work done to build a strainmeter that can be pushed into the boring to couple the instrument to unconsolidated material using friction. Tests in the laboratory were done to evaluate its properties. Tests in the field were done to study the performance of the instrument. Numerical models were built to interpret the strain signals measured during the experiments.

DESIGN OBJECTIVES AND CONSTRAINTS

The design of the direct-push strainmeter was guided by objectives and constraints meant to make it capable of detecting strain events in unconsolidated geologic media, such as the alluvium at Utah FORGE. The constraints include the strain components, strain resolution, the instrument physical properties, deployment logistics and size.

Strain Components

Measuring data from several directions is essential to quantify subsurface deformation. The baseline goal of this instrument was to measure three strain components normal to the axis of the strainmeter so the magnitude and direction of the principal strain could be resolved. A strain component parallel to the axis would allow the full tensor to be measured. These objectives are similar to those outlined in Chapter Three.

Strain Resolution

The direct-push strainmeter needed to be capable of accurately resolving strains expected to occur in the vicinity of wells operating deeper in geothermal reservoirs as well as strains that occur during deployment. According to the simulation of hydraulic fracturing at Utah FORGE described in Chapter Three and strain data measured in the subsurface during injection tests at

the field site, the strain field at the ground surface is in the order of nanostrain (Figure 36). For this reason, the strainmeter needs to be capable of resolving strains in the order of nε.

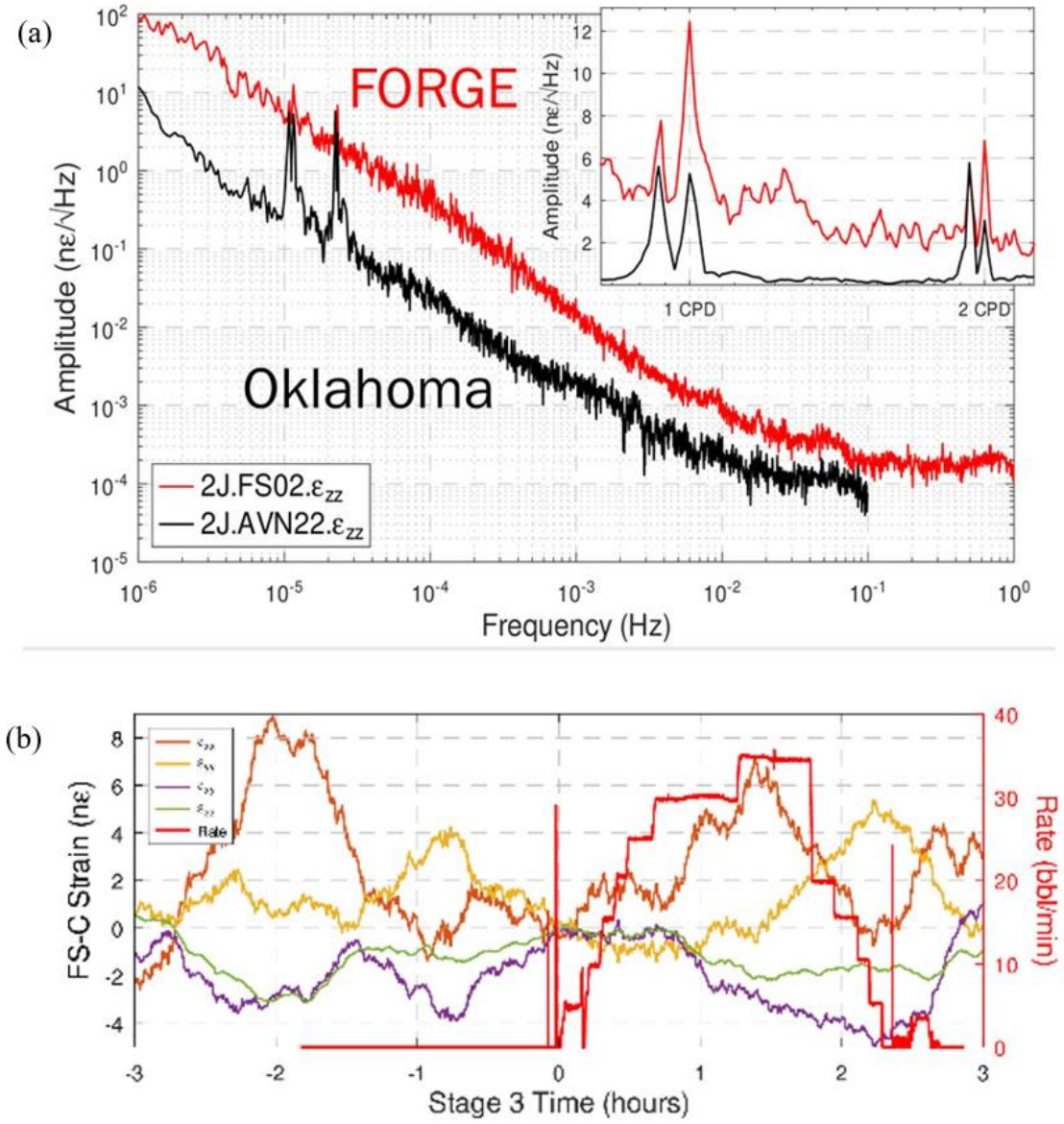

Figure 36. Ambient noise amplitude spectra measured at Utah FORGE and in a different field site in Oklahoma (a). Strains measured before and during an injection test in Utah FORGE (b).

Coupling the strainmeter to the formation may cause significant strains in the instrument during deployment. This may damage the strainmeter or otherwise affect its performance, so it would be useful to measure strains during deployment. A method that can measure strains of several 1000 με would be ideal. High resolution strain measurements that can satisfy the nε constraint may lack the dynamic range to also measure the large strains during deployment, so an additional measurement method may be required.

Measuring strain during deployment has not been done before. Understanding the stresses at play during the installation of a strainmeter could help future designs. It is assumed that as the instrument will be pushed down the strains will vary greatly. Adding low resolution strain sensors to the direct push would make it possible to measure strain instantaneously and over a broad range. This can be done with Fiber Bragg Grating sensors (FBG).

Coupling to Formation

Strainmeters must be coupled to the enveloping formation to provide meaningful data, and the need for an alternative method of coupling was one of the primary motivations behind developing the direct-push strainmeter. This motivation was based on the performance of strainmeters deployed by cementing them into borings in alluvium at Utah FORGE. Strains fluctuated by several nε during a hydraulic fracturing operation at Utah FORGE, which is consistent with the model predictions in Chapter Three (Figure 9), but the strains fluctuated by similar magnitudes prior to hydraulic fracturing. This indicates that the fluctuations in Figure 36b are noise that is unrelated to hydraulic fracturing. The magnitude spectra confirm that the ambient noise in the alluvium at Utah FORGE is at least an order of magnitude greater than is measured by strainmeters completed in rock (Figure 36a). The high noise level appears to be partly a result of apparent “events” that are unrelated to barometric pressure or earth tides

(Figure 37). All strain components change by up to several tens of nε over durations from tens of seconds to tens of minutes during the events. Events are observed at all four strainmeters at FORGE, but each event is restricted to an individual strainmeter, the same event is not observed at multiple strainmeters.

The origin of the events is unknown, but one possibility is that they are related to localized slip between grains in the alluvium. This is consistent with their occurrence in alluvium but not shale, and in their limitation to only one strainmeter, and it is also consistent with an event where all the strain components vary at the same time. Drilling a borehole reduces compressive stresses in the vicinity of the hole, whereas cementing increases compression.

One hypothesis if that the drilling and cementing process changes stresses enough to result in slip of grains in the vicinity of the borehole. This hypothesis can be tested by deploying strainmeters that avoid using cement to couple the strainmeters to the enveloping formation. It appears to be possible to couple strainmeters to a formation using friction, instead of cement, and this motivated the development of the direct-push strainmeter.

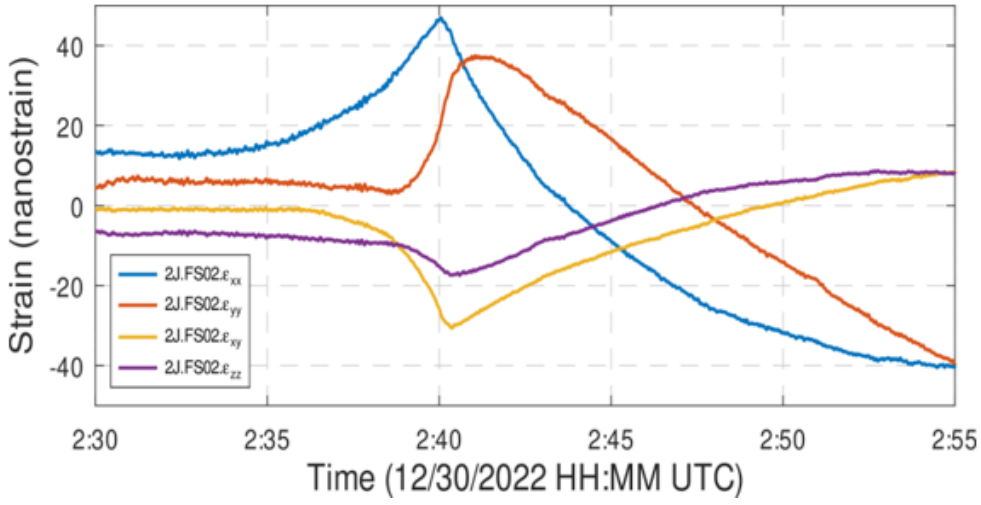

Figure 37. Strain time series during an event of unknown origin at Utah FORGE

Calibration of the instrument

One challenge to using high-resolution strain measurement systems, like an interferometer, is that they require calibration. One approach is to calculate the strain created by earth tides and then correlate that strain to the signal of optical phase measured by the strainmeter. This gives a transfer function from phase to strain. Preliminary measurements in shallow alluvium suggested that it may be difficult to resolve tidal signals, so an alternative method of calibration is needed.

In Zhang et al (2021), two optical sensors with different resolutions, FBG and Mach-Zehnder interferometer, are combined to measure physical properties. The results for each sensor are analyzed separately and combined with a matrix to get value for a change in the index of refraction and temperature. For the Utah FORGE project, strain needs to be measured explicitly. The Michelson interferometers already present at the Utah FORGE field site measure deformation with units of radians.

A goal of this design is to combine Fiber Bragg Grating sensors to a Mach-Zehnder interferometer (MZI) to calibrate the interferometer so the radians can be converted to strain.

Elastic modulus matching

The contrast between the elastic properties of the strainmeter and those of the enveloping media affect the performance of the strainmeter. A strainmeter that is stiffer than the enveloping media will deform less than the media and this will increase the deformation in adjacent material. This occurs, for example, when strainmeters contained within a stainless-steel tube are deployed in soil. The effective elastic modulus of strainmeter in a steel tube is expected to be 10 GPa or more, whereas the elastic modulus of shallow soils is in the range of 0.01 to 0.1 GPa, so the

modulus contrast would be between 100 and 1000. Conversely, a relatively soft strainmeter will deform more than the enveloping media. These effects can be accommodated by calibration using an external signal of known magnitude, such as an earth tide signal. However, the extent to which the contrast in elastic modulus affects strain results can be difficult to characterize, so under ideal conditions the effective modulus of the strainmeter would be the same as that of the enveloping formation. This would improve the reliability of the strain measurements, and it would also relax the requirements for in-situ calibration. A strainmeter calibration from the laboratory, for example, could be used in the field in cases where the modulus contrast between the strainmeter and the enveloping media was small.

A goal of this design is for the apparent elastic modulus of the strainmeter to match that of saprolite.

Deployment logistics

Strainmeters are deployed in boreholes to place them in the region where strain is occurring. The instrument has to be coupled with the geologic formation so that strain within the formation is transferred to the strainmeter. Most strainmeters are cylindrical and are coupled to the formation using expanding cement in the annulus between the cylinder and the borehole wall (Murdoch et al, 2019).

Due to the strain field values at the subsurface (Figure 9) and the difference in stiffness between alluvium and cement traditional methods cannot be used for the direct-push strainmeter. It is assumed the alluvium-instrument coupling could be done by friction. The objective is to be able to push the strainmeter directly into a pilot hole with a smaller diameter than the instrument. This may require significant force, which would result from shear stress on the surface of the

instrument. Optical fiber breaks when their axial strain exceeds 0.02 to 0.04 με, so strains during deployment that exceed these values could damage the fiber making the instrument unusable. It is necessary to use a material that will not only reflect the elastic property of the alluvium but also be able to limit the strains applied during deployment.

Size constraints

The size of the strainmeter is constrained by the size of the pilot hole. In general, the strainmeter needs to be slightly smaller than the size of the pilot hole to strike the balance between compression that is large enough to couple the strainmeter to the soil but small enough to avoid damaging the strainmeter. It is assumed the pilot holes would be made using drilling methods that were either already available, or that could be readily obtained. The diameter of the strainmeter was estimated to be at least 1mm and no more than 5 mm greater than the diameter of the pilot hole, although this range is open to revision.

CONCEPTUAL DESIGN

The basic design concept that was developed to meet the goals and constraints was to create a cylindrical strainmeter from urethane with a threaded steel rod at its center. This strainmeter will endure several strain events requiring sensors with different resolutions capable of measuring several strain components. A solution to this challenge is to include fiber Bragg Gratings (FBGs) and a Mach-Zehnder interferometer (MZI) within the same instrument (Figure 38). Output from the FBGs can also be used to calibrate the MZI. It should be feasible to deploy strain sensors around the entire circumference of the strainmeter and this would facilitate measuring the strain tensor normal to the axis of the instrument.

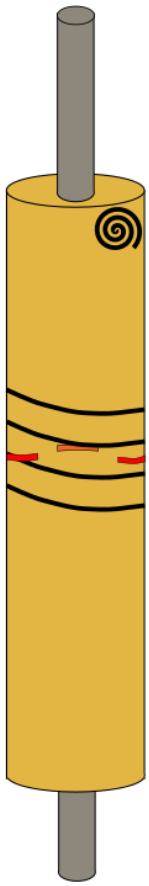

Figure 38. Conceptual model of a direct push with a Mach-Zehnder interferometer (black lines, the reference arm is represented with a coiled line at the top of the instrument, the measuring arm is represented with four bent lines in the middle of the instrument) and FBGs (red). The grey tube represents a threaded rod.

One constraint of the direct-push strainmeter design is that it should be compliant enough to approximately match the elastic modulus of the soil, while it is stiff enough to prevent damage to the fiber when being pushed down during deployment. This should be possible using a polymer with a modulus similar to soil that is reinforced with an axial rod. Some preliminary designs were developed and evaluated by casting a cylinder from urethane rubber with an axial hole 1.9 cm in diameter. A 1.9-cm diameter threaded rod was placed in the hole and protective caps were added at the top and bottom of the strainmeter. This “lose” threaded rod design was brought to the field and pushed in a pilot hole with a geoprobe. The hole had been drilled with a

4-inch (10 cm) auger over 10 feet (3 m). Then a 2-inch (5 cm) macrocore was used to reach a depth of 14 feet (4.3 m). The strainmeter was pushed down for 3.5 m and hammered for another 0.8 m. It was noticed after that the lose threaded rod design did not withstand deployment as the fiber broke.

Two types of optical fiber strain sensors and interrogators will be required. Fiber Bragg Gratings are capable of measuring strains in the range of 1 to 20,000 με, and they can measure strain change relative to a baseline without continuous monitoring, so they are ideal for measuring relatively large strains in the laboratory and during deployment. FBGs cannot achieve sufficient resolution (1 nε goal) for field applications, however. Both Michelson or Mach-Zehnder optical fiber interferometers can meet the resolution goal, but they require continuous monitoring and can have difficulties tracking large strains such as those that may occur in the lab and during deployment.

The design should accommodate optical fiber strain sensors that are arranged either circumferentially or axially around the strainmeter.

COMPONENTS

Components to build the direct push strainmeter were chosen to tackle the constraints listed above. Those materials were chosen due to their physical properties and their availability.

Strain sensors

Two optical fiber sensor technologies were used to design the strainmeter: (1) Fiber Bragg Grating sensors and (2) Mach-Zehnder interferometer.

Fiber Bragg Grating

This design used FBGs on 1550 nm acrylate coated fiber. The direct-push strainmeter is intended for use at ambient outside temperatures, so the high-temperature polyimide fiber used in the split-sleeve strainmeter was unnecessary. Fiber Bragg Grating (FBG) sensors were previously described in detail in Chapter One. The MicronOptics SM125 interrogator and its ENLIGHT software were used as data collection tools.

Interferometer

A MZI was used as the interferometer in the direct-push strainmeter. A Michelson interferometer would also meet the constraints, but a MZI was chosen so it could be evaluated in the field before using it in the split-sleeve strainmeter. It was infeasible to deploy a high temperature split-sleeve strainmeter at the Clemson field site, so it was used in the direct-push strainmeter. The principles of interferometry were described in Chapter One.

Sensor packaging

The instrument was made with urethane cast onto a 1.9-cm threaded steel rod. Fixtures for the MZI were created using 3D printing.

The urethane rubber used for this project was the PMC-780 Dry urethane rubber from Smooth-On. It comes with 2 containers, part A and part B. They are mixed following a 2A:1B ratio by weight or by volume. The mixture has a pot life of 25 minutes and takes 48 hours to cure. It has a density of 1020 kg/m^3 and a tensile strength of 6 MPa once cured. The hardness of the urethane is 80 durometer. Several methods have been used to evaluate the relationship between durometer and Young's modulus, and the results are summarized by Larson (2019). His results indicate that Shore-A durometer is a Young's modulus between 1 MPa and 10 MPa. The

urethane was cast to shape using two molds created with polyactic acid (PLA) using a 3D printer. One mold (inner mold) was used to cast an inner cylindrical piece, 30.6 cm long and 5 cm in diameter. Another mold (outer mold) was used to cast a 6-mm-thick layer of urethane around the inner casting.

The molds used to cure the urethane resin in were designed on SolidWork and printed with polyactic acid fiber at a 3D printing shop. The mold for the inner casting has a recess for the threaded rod at the bottom, a ramp for the C-channel at the top and three protrusions to form centralizers on the urethane base (Figure 39). The centralizers help keep the instrument in place when inserted into the second mold. The base mold is 35.2 cm tall with a mark at 30.6 cm so urethane can be poured without overflowing. The diameter is 5 cm. A cap with holes for the threaded rod and the C-channel goes on top of it to centralize the rod. The outer mold has a place for the threaded rod and a male fitting at the bottom (Figure 40). It is 34.3 cm tall and has a diameter of 5.67 cm.

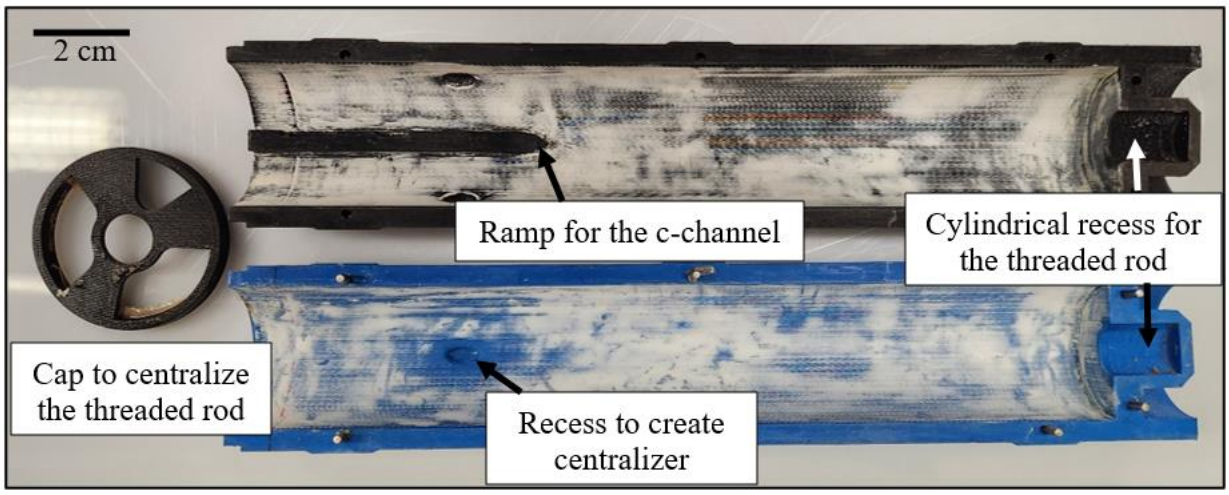

Figure 39. Inner mold for direct-push strainmeter. The inside was sanded and filled with epoxy putty to get a smooth surface after curing.

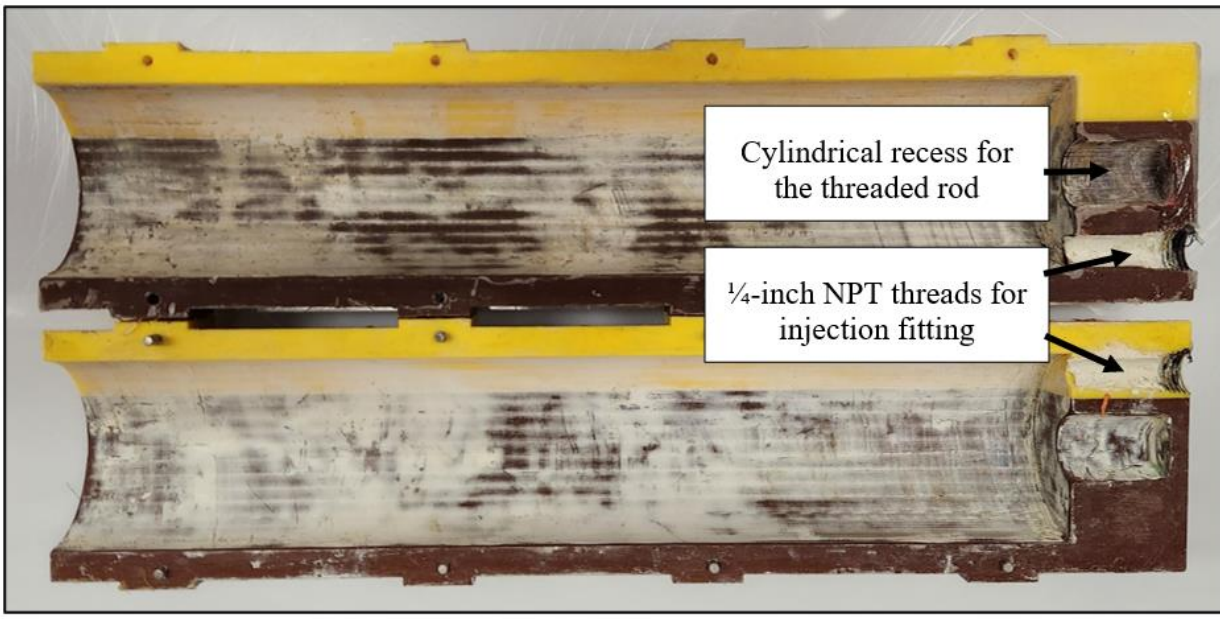

Figure 40. Outer mold for the direct-push strainmeter.

The stainless-steel threaded rod is 1.5 m long with a 0.75-10 thread pitch. Both molds have a 2.54 cm and 1.9 cm wide cylindrical fixture so the threaded rod can be embedded at the center of the instrument. A cap goes on the inner mold to ensure that the threaded rod stand straight while the urethane base cures.

The aluminum c-channel was used to contain the splices and optical couplers used in the MZI. The channel is 1 m long and 0.76 cm wide. The mold for the base has a 0.8x11.4 cm ramp for the c-channel.

A Mach-Zehnder interferometer has a reference fiber that needs to be isolated from strain (more information about MZI is in Chapter One). An enclosure was designed (Figure 41) to contain the reference fiber. The reference fiber is coiled around a central spool and the extremities of the fiber are directed by two channels to the c-channel. The 3.4 x 4.5 cm enclosure was clipped to one slide of the c-channel. A flat cap was made to close the enclosure and cover the reference fiber. The coil, cap and enclosure (Figure 41) and were 3D printed from nylon.

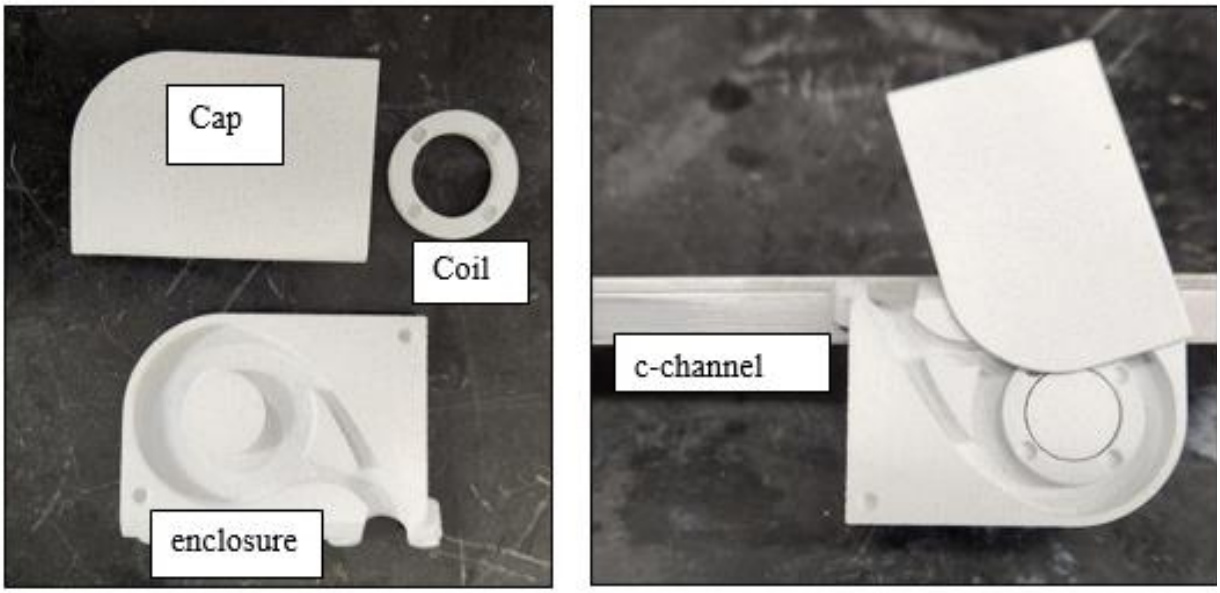

Figure 41. Enclosure for the reference fiber of the Mach-Zehnder interferometer.

PROTOTYPE STRAINMETER

The prototype strainmeter was cast from urethane resin in three steps. The fabrication procedure involves creating an inner casting that is cured, and then the optical fiber sensor is wrapped around the casting. The inner casting with the optical fiber is placed in the outer mold and another layer of urethane is formed around the inner casting to protect the optical fiber.

Air bubbles can create points of weakness within the direct-push strainmeter. They increase the risk of damaging the fiber when the strainmeter is flexed by concentrating stresses. They can also cause a gap in the direct-push strainmeter-strain sensor-soil contact area and alter the strain measurements. Finding a procedure and materials causing the least amount of air bubble was a priority. The urethane resin was mixed with a rotational blender and degassed in a vacuum chamber at 28 psi for about 20 minutes before being used in the molds. The inner mold was tipped slightly off vertical and the resin was poured in from the top. It flowed down the side of the mold and filled it from the bottom up. The inner casting was removed from the mold and

processed as described below, and then it was placed in the outer mold. The diameter of the outer mold is approximately 0.67 cm larger than the inner casting, and there are three bulges in the inner casting that centralize it in the outer mold. The urethane was initially poured into the outer mold from the top, using the same procedure that was used for the inner mold. The outer layer of urethane in the early prototypes contained a large number of air bubbles, it was thought that air was being trapped when the urethane was poured in from the top.

The mold was then redesigned so it could be filled from the bottom. A 1 cm hole was drilled at the base of the mold and the outside was tapped for a 1/4-inch NPT. A 5 cm diameter butyrate tube with a 1 mm wall was cut to be 15 cm long. It was fitted with two 4.9-cm diameter pistons with O-ring seals (Figure 42). The piston at the bottom is tapped ¼-inch NPT, and barb fittings were used to connect the piston to the mold with ¼-inch tube. The butyrate tube was filled with de-aired resin with the bottom piston in place, the top piston was put in place and the assembly was placed in a caulking gun without modification (Figure 42). The caulking gun was used to inject resin and fill the mold from the bottom up.

Figure 42. Caulking gun and pistons used to inject urethane resin into the outer mold. The pistons are inserted into a butyrate tube (not shown) containing resin.

The fabrication procedure began by sanding the inner mold and applying mold release in it. Then the 1-m long C-channel with the enclosure attached was clipped on the ramp, the 1.5 m long threaded rod was placed in a recess in the bottom of the inner mold, and the cap fits over the threaded rod and centralizes the rod in the mold. A mass of 440 g of PMC-780 Part A was poured into a plastic container. Then 220 g of PMC-780 Part B dry was added to give a 2:1 ratio of A:B. The resin was mixed vigorously for 3 minutes with a rotational blender. The container was placed in a vacuum chamber at 28 psi for 20 minutes. The urethane was then poured into the inner mold and left to cure for 48 hours (Figure 43).

(a) (b)

Figure 43. (a) The inner with the threaded rod in a vertical position during curing. The mold was attached to a pipe with tape. The mold was closed tight using hose clamps. (b) The inner casting has the enclosure, C-channel and threaded rod embedded in it.

The second step consisted in attaching the MZI and FBG optical fiber sensors to the inner casting (Figure 43b). This was accomplished by first cleaning the casting and slightly sanding it to improve bonding with the next layer of urethane. Construction of the MZI began by cutting two, 3-m long pieces of acrylate-coated SM28e optical fiber that will be used as the reference and measuring fibers. The fibers attached to the 2x2 and 3x3 couplers were cut to be 50 cm long. Two meters of the reference fiber was coiled onto the spool, which was then placed in the enclosure. Clear silicone sealant (Loctite) was used to bond the nylon printed flat cap onto the enclosure. Two meters of the measuring fiber was wrapped around the circumference of the inner urethane casting (13 wraps) between 7 cm and 16 cm from the bottom of the casting. One end of the reference and measuring fibers were spliced to the 2x2 coupler and the fibers and splices were placed in the C-channel. The other ends of the reference and measuring fibers were spliced to two fibers on one side of the 3x3 coupler. The third fiber of the coupler was cut to be 1 cm long.

An acrylate coated fiber with 3 FBGs spaced 15 cm apart was wrapped around the inner urethane casting at 11 cm from the bottom and the fiber excess was placed in the C-channel.

The breaking strength of optical fiber is roughly 0.5 to 1 N, which is enough to limit damage during careful handling in the lab, but it is too weak for field applications. To address this problem, the optical fibers in the strainmeter were connected to fibers in a reinforced 24-m long tactical cable. The cable contains four fibers with tightly buffered, colored coatings that are contained in a Kevlar jacket and coated in polymer. One fiber was spliced to the upper end of the 2x2 coupler, and two fibers were spliced to the 3x3 coupler. The other fiber in the tactical cable was spliced to the fibers containing the FBGs. FC connectors were spliced to the up-hole end of the tactical cable.

Low viscosity epoxy-ER040 resin (Progressive Epoxy Polymers Inc) was mixed, de-aired for 10 minutes at 28 psi and poured into the C-channel to keep the fibers, splices, and 2 cm of tactical cable in place and protect them from damage. It was left to cure for 24 hours.

The third step began with placing the inner casting with the fiber sensors in the outer mold, which was secured with clamps (similar to Figure 43a). A total mass of 260 g of urethane resin was mixed and degassed for 15 minutes and transferred to the injection tube used with the caulking gun (Figure 42). The bottom piston was attached to the mold using ¼-inch (0.63 cm) diameter tygon tubing. Urethane resin was then injected into the mold over several minutes. After curing for 48 hours, end caps were secured, a fiberglass tube was attached and the instrument was ready to be tested (Figure 44).

LABORATORY TESTING

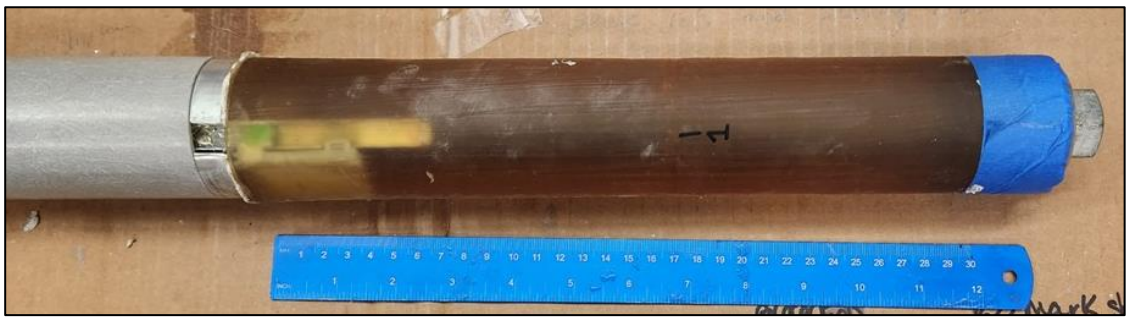

Figure 44. Direct-push strainmeter created from urethane casting and containing 3 FBGs and a Mach-Zehnder interferometer. C-channel and enclosure are visible through the outer layer of urethane on the left side. Blue tape on the right side covers a bottom end cap.

The direct-push strainmeter was tested in the laboratory for basic functionality and calibration. The objectives of the tests were to find a calibration equation relating the optical phase measured by the Mach-Zehnder interferometer to the strain and pressure applied to the instrument. The approach was to first build a pressure chamber for changing the pressure applied to the strainmeter with water or air. The strainmeter would be put in the apparatus and the

response to different pressures would be measured. The data were then used to correlate optical phase to strain and pressure.

Apparatus

The pressure chamber apparatus is a 1.6-m long 4-inch PVC pipe with caps at the top and bottom, which is mounted vertically on the wall. A ¼-inch female fitting was screwed into the bottom cap of the pipe and a Y fitting was added to connect two valves (Figure 45). A 0.21 MPa transducer was connected to one of the valves to record pressure change over time. A scale of 200 cm was placed vertically along the chamber and a clear ¼-inch (0.64-cm diameter) tygon tubing was connected to the other valve and placed along the scale. This tubing was unplugged and replaced with a Quick Connect air fitting for the pressure change test with an air compressor. The transducer is connected to a Campbell data logger to record the pressure as a function of time. A strain-relief cable gland fitting with an opening large enough to accommodate the optical connectors on the tactical cable was attached to the top cap of the pressure chamber. The strain-relief cable gland could be tightened around the tactical cable to seal the strainmeter inside the pressure chamber while the tactical cable was attached to optical interrogators.

Hydrostatic test

The first series of experiments were hydrostatic tests. After putting the direct-push strainmeter in the pipe, water was added until the instrument was under water. To minimize the temperature effect on the strain measurements the set up was left at room temperature for a few hours before testing. The water level was changed at a constant rate with a peristaltic pump.

The first series of tests involved a 10 cm water level change. The water was removed at 0.3 gpm and then reinjected five times while the MZI and the FBGs were connected to their

respective interrogators and computers. Pressure data were recorded with the transducer. Only the Mach-Zehnder produced a response to the water level change, which was approximately 1 kPa, so the pressure head change was increased to 20 cm and then 50 cm.

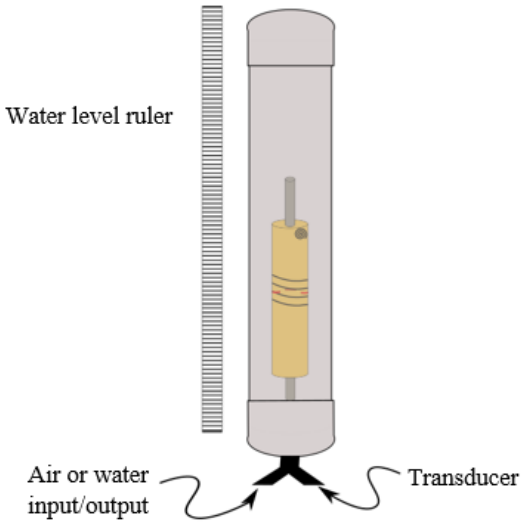

Figure 45. Conceptual model of the pressure change apparatus.

The change in pressure caused by the hydrostatic test caused strains that were too small for the FBGs to measure. It was decided to change the approach and use an air compressor to cause a bigger pressure change in the pipe.

Air compressor test

The PVC pipe was emptied, and the tygon tubing disconnected from the valve to plug the air fitting connected to an air compressor. The tactical cable was passed through the cable gland on the top cap of the pipe and the gland was tightened onto the tactical cable. The air compressor was used to increase the pressure in the chamber to 20 psi. For the first two tests, the valve at the bottom of the pressure chamber was left open. The air compressor was turned off and the pressure decreased for 3 minutes. For the next tests, the valve was closed when the air

compressor was turned off and the pressure decreased gradually over 10 minutes. Signals were recorded by the FBGs and Mach-Zehnder interferometer during the four tests (Figure 46).

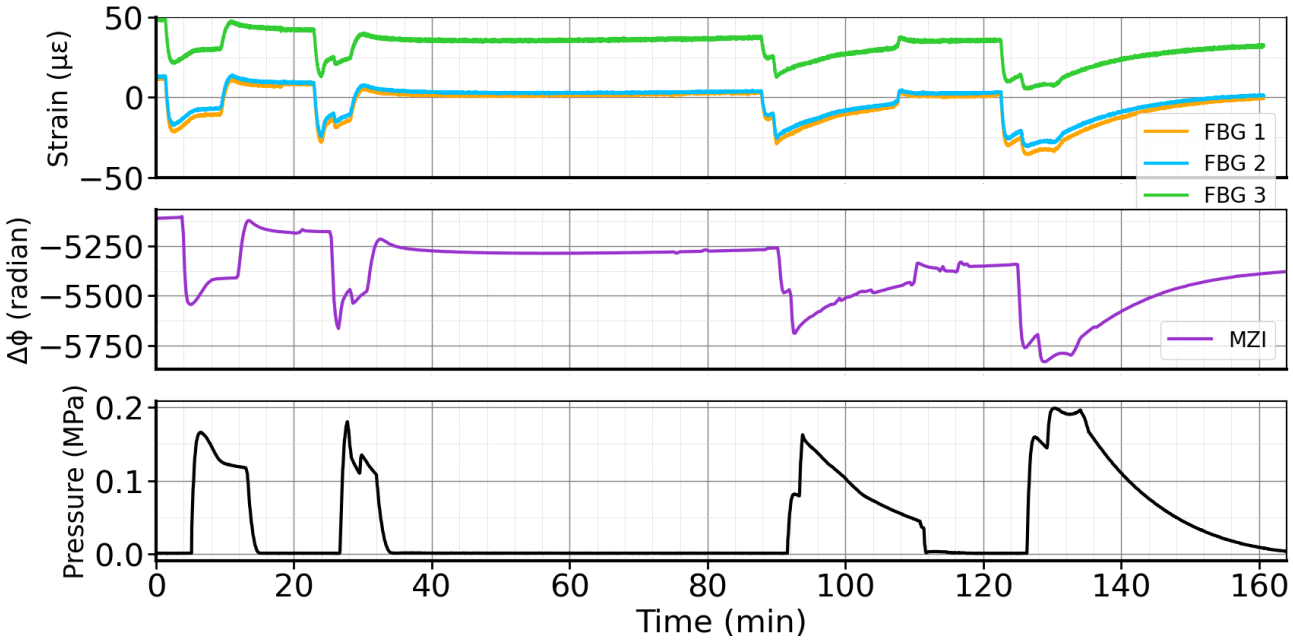

Figure 46. Signals during calibration experiments, (a) strain measured by FBGs, (b) optical phase measured by the MZI, (c) pressure in the chamber.

The signals measured by the FBGs and the MZI have a similar shape for all four tests (Figure 46). The pressure increased by 0.16 to 0.2 MPa (23 to 30 psi) over a few minutes and then decreased over 3 to 30 minutes (Figure 46c). The strains from FBG 1 and 2 are similar to each other while the strain measured by FBG 3 is approximately 40 με greater (Figure 46a). This could be due to the strainmeter position in the PVC pipe. The direct-push strainmeter was in the pipe slightly diagonally so the threaded rod could rest on the pipe edges. This slight tilt could add weight on one side of the instrument resulting in one FBG measuring a higher baseline for the strain signal. The amplitudes of the three strains responding to an increase in pressure are about -26 με. This value stays the same for all four changes in pressure, only the baseline strain signal decreases a little. The optical phase change measured by the MZI decreases by about 375 radians when the pressure increased (Figure 46b).

To calibrate the MZI the strain change from the FBGs was averaged and correlated to the optical phase measured by the MZI (Figure 47). The data during an increase in strain trace out a slightly different path than during a decrease, but the slopes are nearly identical.

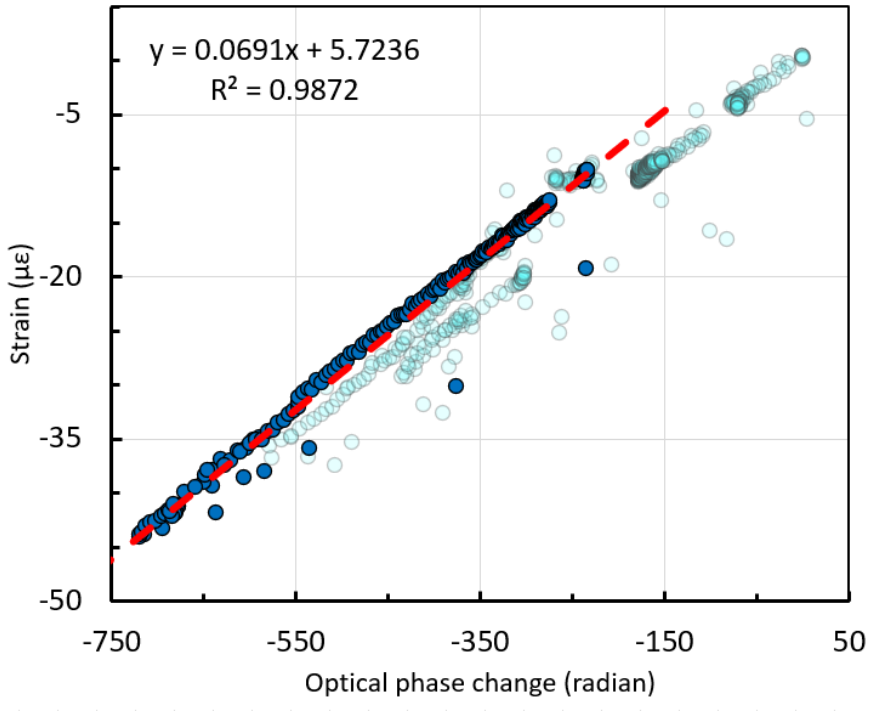

Figure 47. Average circumferential strain measured by FBGs as a function of optical phase change of MZI during testing in a pressure chamber

The data were also used to determine the apparent elastic modulus of the direct-push strainmeter by plotting pressure change as a function of strain. The value of the slope for a direct-push strainmeter with an embedded threaded rod gives the apparent modulus, E_a =9,800 MPa (Figure 48a) and E_a = 66 MPa for a strainmeter with a loose threaded rod (Figure 48b). This large range of apparent elastic modulus was surprising because the FBGs were embedded in the same urethane resin and the instruments only differed by how the threaded rod was attached to the urethane casing.

Urethane was used to create a strainmeter with an effective modulus similar to saprolite. The elastic modulus of saprolite at the field site is in the range of 60 to 100 MPa, so the apparent modulus of the loose threaded rod strainmeter is in correct range. However, the optical fiber in the loose threaded rod prototype broke during deployment. Breakage appears to have occurred because deformation that occurred during deployment exceeded the strength of the fiber. The apparent modulus of the prototype with the embedded threaded rod was much stiffer than the one with the loose rod, but a prototype with this design was successfully deployed without breaking the fiber. Nevertheless, this instrument is much stiffer than saprolite, so in-situ calibration methods will be needed to measure the correct value of strain.

Simulations

The response of the direct-push strainmeter to hydrostatic loading was simulated to evaluate the large range of apparent elastic modulus observed during testing (e.g. Figure 48). The simulations were done by assuming linear elastic behaviour and a geometry that could be represented in axial symmetry. The strainmeter was represented as one cylinder embedded in another. The inner cylinder (green block in Figure 49) presents either an open hole, an open hole partially filled with material, or an embedded steel rod. The outer cylinder (blue in Figure 49) represents the urethane casting. Aluminum discs on the top and bottom of the region representing the urethane casting were included to represent the aluminum disks that bound the top and bottom of the casting (Figure 49).

(a) (b)

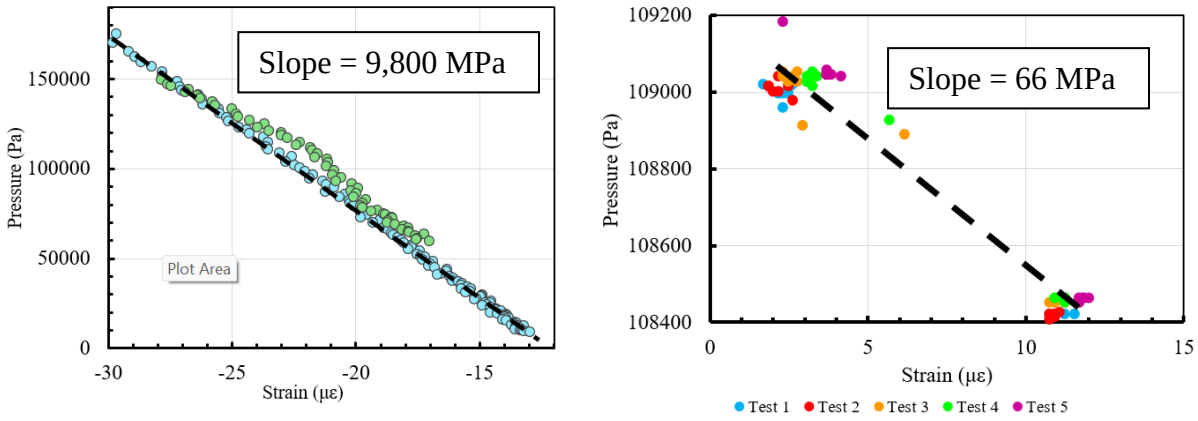

Figure 48. Pressure as a function of strain measured for two direct-push strainmeters, an embedded threaded rod strainmeter (a) and a loose threaded rod strainmeter (b). The slope is the apparent elastic modulus, E_a.

A fixed displacement boundary condition was used at the top of the inner cylinder, whereas roller boundaries were used on the upper and lower surfaces of the aluminum disks (circles in Figure 49). This is appropriate because the aluminum disks were much stiffer than the urethane and they were attached to the steel rod along the axis of the casting. A specified pressure boundary was used on the outer surface of the urethane casing to represent hydrostatic pressure. The boundary conditions assume that the hydrostatic pressure is only applied on the outer surface of the urethane casting. Sealant was used between the casting and the upper and lower disks to prevent those faces from being loaded by pressure.

Simulations were conducted using three values for Young's modulus of the inner cylinder, E_i = 1 Pa, 10^7 Pa, and 10^{11}Pa. The small value (E_i = 1 Pa) causes the inner cylinder to behave as an open hole, whereas the large value ($E_i = 10^{11}$ Pa) causes it to behave as a steel rod.

The intermediate value of E represents a hole that is partially supported. For example, during compression the urethane casting could be displaced onto the threads on a threaded rod much more than on a smooth rod, so the threaded rod could be represented by the intermediate value of E_i.

The specified pressure was increased incrementally from 0 to 0.15 MPa and the circumferential strain was calculated at the location of the FBG sensors (Figure 49) for each of the three values of E_i. The Young's modulus of the outer cylinder was set to 20 MPa, which was estimated from the durometer = 80A rating of the urethane resin provided by the manufacturer. There is some uncertainty when converting durometer to Young's modulus, according to a review of analyses and dataset summarized in Table 3. One reason for this uncertainty is that the relationship between stress and strain for urethanes is non-linear (Qi & Boyce, 2005), but Young's modulus implies that it is linear, so some approximation is required. The Young's modulus of resin durometer 80A ranges from 12 to approximately 40 MPa. A mid-range value of E = 20 MPa was used in the simulations.

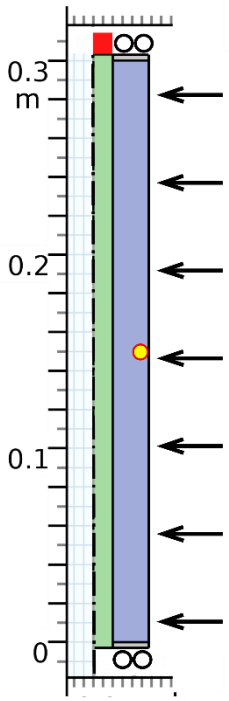

Figure 49. Schematic of simulation of direct push strainmeter. Urethane casting (blue), axial hole or rod (green), circumferential strain sensor (yellow circle with red rim), end caps (gray). Specified pressure (arrows), roller boundary (circles), fixed boundary (red square), axis of rotation (dashed dot line).

The analysis was calibrated by adjusting the Poisson's ratio of the outer cylinder and comparing the results to experimental values.

Results

In general, increasing the strain causes the applied pressure to decrease (Figure 50). The pressure is a linear function of the strain and the absolute value of the derivative dp/dε is the apparent modulus of the instrument, E_a (labeled in Figure 50). The rate at which the strain decreases with pressure is a strong function of the stiffness of the inner cylinder. The apparent modulus of the instrument is E_a = 68 MPa when the inner cylinder of the instrument is an open cavity. The apparent modulus increases by two orders of magnitude, however, when the modulus of the inner cylinder is increased to represent an embedded rod.

Table 3. Estimates of Young's Modulus of PMC 780 Dry urethane resin.

Young's Modulus estimated for Shore 80A	Source
12 MPa	PSI Urethane, Inc. "Calculating the compression/deflection of urethane".
32 MPa	Precision Urethane & Machine, Inc. "Cast urethane hardness data".
12 MPa	Plastic Insights. Johannes Kunz and Mario Studer, (2006). Determining the modulus of elasticity in compression via Shore A Hardness test. Issue 6.
10-40 MPa	Dow Chemical Company. Kent Larson (2017). Can You Estimate Modulus From Durometer Hardness for Silicones?

The values of apparent modulus for the instrument with an open cylinder and embedded rod are consistent with the data measured during hydrostatic tests in the laboratory (Figure 48). For example, the experimental value for an open cylinder is E_a=66 MPa and the simulated value is nearly identical, E_a=68 MPa. The experimental value for the embedded rod is 9800 MPa and the simulated value is 6600 MPa, which is similar to the experimental value relative to the value determine for a loose fitting threaded rod.

A value of Poisson's ratio of ν = 0.499 was used in the simulation to generate the data in Figure 50. This estimate was obtained by manual fitting, so no error estimates are available, but the upper end of E_a is sensitive to ν and a value of ν = 0.490 gives a result for E_a that is an order of magnitude less than that obtained in the experiments. Poisson's ratio of rubber is generally recognized to be approximately equal to 0.5, according to Engineering Toolbox which cites a value of 0.48~0.5. Qi & Boyce (2005) point out that the stress-strain constitutive model for urethane is non-linear, but that the effective Poisson's ratio is in the range of 0.48-0.5. As a result, the large value of Poisson's ratio (ν = 0.499) determined from this analysis appears to be consistent with results from other tests characterizing the behavior of rubber.

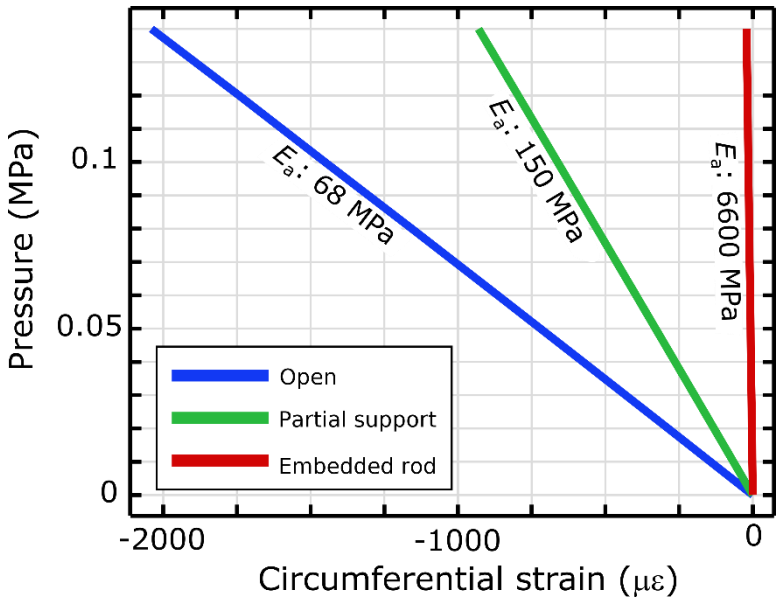

Figure 50. Pressure as a function of circumferential strain for three different moduli of the inner cylinder. An open inner cylinder is represent using E = 1 Pa (blue), a partially supported inner cylinder is represented using E = 10^7 Pa (green), and a steel rod embedded in the urethane casting is represented using E = 10^{11}Pa (red). The slopes are an effective modulus of the strainmeter and are labeled along each plots.

A conceptual explanation for the behavior of the urethane cylinder is that pressure on the outside of instrument compresses the urethane casting in a radial direction and this causes

elongation in the axial direction. The effective modulus of the instrument is similar to the Young's modulus of the urethane when the urethane casting can extend axially. This occurs when the inner cylinder is open, or when it open and resting on threaded rod. However, the stiffness of the urethane casting is more similar to the bulk modulus when axial elongation is prevented by the threaded rod embedded in the casting. Bulk modulus is given by

$$K = \frac{E}{3(1-2\nu)}$$

So, for E = 20 MPa and ν = 0.499, K = 3330 MPa, which is slightly less than, but similar to the value of E_a for the direct push instrument with the embedded threaded rod.

The original motive for using urethane was to construct a strainmeter with an effective modulus similar to that of the soil. The results from the experiments and theoretical analyses show that effective modulus of the strainmeter is sensitive to both properties of the material used to construct the strainmeter, and to how the strainmeter can deform during deployment. The effective modulus is similar to that of soil when the cylinder is free to deform, but the fiber broke when this instrument was deployed. An axial rod embedded in the urethance casting reduced the probability of breaking a fiber during deployment, but it also increased the effective modulus of the strainmeter to two orders of magnitude more than soil. This occurs because of the large Poisson's ratio of urethane. Future designs should take these insights into consideration when designing strainmeters that can match the modulus of soil and that can be successfully deployed without breaking the optical fiber used to make the strain measurements.

FIELD TESTING

The optical fiber in the urethane strainmeter described above was broken at the bottom of the C-channel after laboratory testing so it was unavailable for field testing. Another strainmeter

was used instead for field testing at the Clemson Bull Farm site. This strainmeter is the same design as the strainmeters currently deployed at Utah FORGE and described in Chapter Two. It measures the horizontal strain in three directions and the vertical strain. The strainmeter uses Michelson optical fiber interferometers wrapped around elliptical rings, which are embedded in epoxy inside a stainless-steel tube. The urethane was selected so the stiffness of the urethane strainmeter would be similar to that of soil, whereas the stiffness of the elliptical ring strainmeter was much greater than soil.

The elliptical ring strainmeter is 11 cm in diameter and it was deployed by pushing into a 10 cm diameter pilot hole using a small drilling rig. It was deployed 10 meters away from the pumping well and the top of the strainmeter is 4.2 m deep. The strainmeter is 1.2 m long so the sensors are between 4.2 and 5 m deep.

Unlike the urethane strainmeter, the elliptical ring strainmeter was not calibrated prior to deployment. This is because the apparatus to create strain in the three directions of the strain sensors was unavailable. Moreover, the orientation of the horizontal strain sensors could not be determined during deployment. As a result, data from the strainmeter were uncalibrated and unoriented. One of the goals of the field testing was to evaluate the feasibility of calibrating and orienting the strainmeter.

Pumping test

Two pumping tests were conducted over a period of two days. The first pumping test lasted one hour. Water was pumped from the aquifer at a constant rate of 3.2 gallon-per-minute. Three monitoring wells were used: SWL-4, SWL-5 and SWL-7, they are located 20.9, 6.7 and 9.1 m away from the pumping well, respectively. Three transducers were set to collect pressure

data every 30 seconds and put in the monitoring well 3 m below the depth to water. A fourth transducer was used to collect barometric pressure. The second pumping test lasted two hours. The depths to water in the monitoring wells were the same as before the first test indicating a 100% recovery from the pumping test done the day before. The pumping rate was measured every 20 minutes with a 5-gallon bucket. The pumping rate was constant for two hours at 3.2 gpm.

Result

Strain and pressure data were measured during the two pumping tests at the Clemson Bull Farm. The pressure was used to evaluate the behavior of the aquifer during pumping and to compare to the strain data.

Pressure data

The day after the second pumping test, the pressure data from all four transducers were collected. The pressure values before pumping and after recovery were deleted and the barometric pressure was subtracted from the pressures in the wells. The pressure data was converted to drawdown values by subtracting the initial head value from the rest of the head values.

The drawdown rate increases rapidly after the pump is turned on and but then rate of increase slows for most of the pumping time (Figure 51). The drawdowns drop when recovery starts at 60 minutes and 120 minutes. The largest drawdown was 1.2 ft (0.37 m) and it occurred at SWL-5, the closest monitoring well. The maximum drawdown at SWL-7 was 0.2 ft (0.06m). The drawdown measured in SWL-4 was less than 0.06 ft (0.2m) and variations were small, erratic and unrelated to times when the pump was on. Drawdown at SWL-4 appears to be less

than the resolution of the transducers (± 0.0014 m) so the data appear to be noise. This is reasonable because SWL-4 is considerably further (r= 20.9 m) from the pumping well than the other two wells (r = 9.1 and r= 6.7 m).

The drawdown rate at SWL-5 starts at 0.04 ft/min (0.012m/min) during the 1-hour pumping test and it then decreases continuously. Before turning off the pump, the drawdown rate is 0.006 ft/min (0.002 m/min). A similar decrease occurs during the 2-hour pumping test. At the beginning of the pumping test, the drawdown rate is 0.03 ft/min (0.008 m/min). By the end of the pumping the rate is 0.003 ft/min (0.001 m/min). The drawdown rate at SWL-4 and SWL-7 are significantly lower at the beginning of the tests than the rate for SWL-5.

The aquifer properties were estimated using a Levenberg-Marquardt parameter estimation algorithm to fit an appropriate forward model to the data from the pumping test. The aquifer at the site is unconfined, the radial extent is large and the well screen essentially penetrates the entire aquifer. These constraints are satisfied using the Neuman (1974) solution for a constant rate pumping test. The parameter estimation process was implemented in AqtesolvPro. This solution assumes that the aquifer is unconfined, homogeneous and anisotropic. The pumping well penetrates the entire aquifer and storage in the well is neglected. At the Clemson Bull Farm Site, the 18.3 m long screen of the pumping well intercepts most of the 20m long saturated zone of the unconfined saprolite aquifer. Each drawdown was fit to a type curve (Figure 51) and the solution gives an estimate of the properties of the aquifer (Table 4).

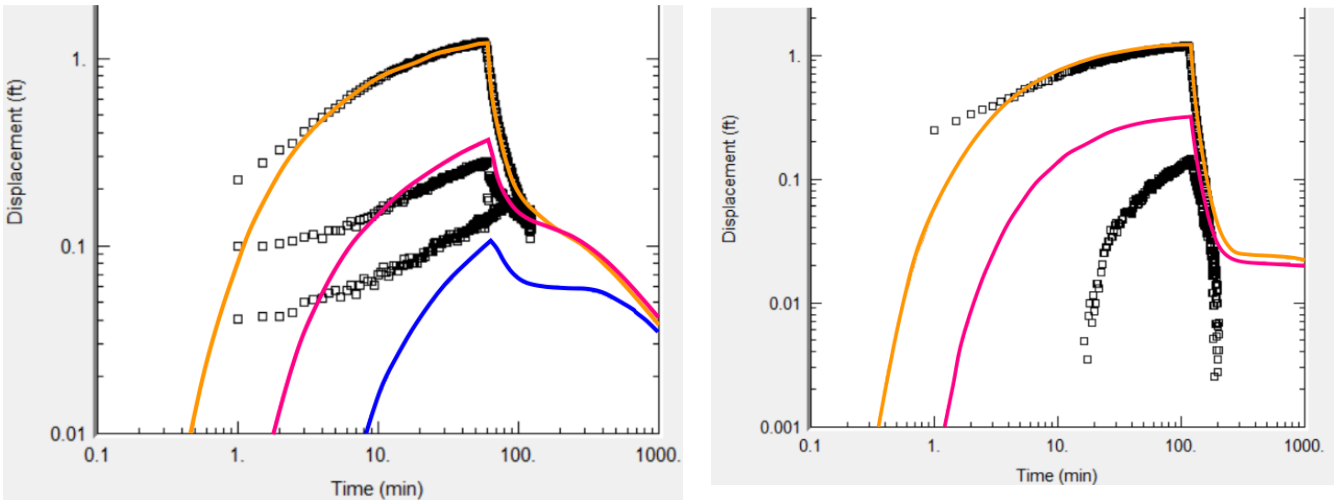

Figure 51. Neuman type curve overlaying drawdown (displacement) data in the monitoring wells for a 1h pumping test (left) and a 2h pumping test (right). The greatest drawdown is observed at SWL-5(orange).

Table 4. Average aquifer parameters and standard error in parentheses estimated from the constant rate pumping tests using the Neuman (1974) solution and parameter estimation methods implemented in AqtesolvPro.	
Transmissivity, T [m^2/s]	8.2×10^{-5} ($\pm 0.81 \times 10^{-5}$)
Storativity (S)	7.2×10^{-4} ($\pm 0.32 \times 10^{-4}$)
Specific Yield (S_y)	0.05 ($\pm 3.75 \times 10^{-4}$)
Hydraulic conductivity, K = T/b [m/s]	4.1×10^{-6} m/s
Hydraulic diffusivity, Dh = T/S	0.11 m^2/s
Hydraulic conductivity ratio (Kz/Kr)	0.89 ($\pm$ 0.16)

Strain data

Strain was measured in the vadose zone using a strainmeter composed with four Michelson interferometers, each measuring a strain from a different direction (Figure 52, Figure 53). The instrument is a cylinder, 1.2 m long and 0.11 m in diameter. The sensing elements of the interferometer are oriented either along the axis of the cylinder (channel VSZ) or along different directions normal to the axis (VS2, VS3, VS4). Channel VS3 is oriented 45° in a clockwise direction looking down from VS2, and channel VS4 is oriented 45° from VS3 and 90° from VS2.

The output of the interrogator is in units of radians of optical phase, which is typically converted to strain using a calibration matrix. Many strainmeters similar to the one used in this test can measure Earth tides, and the Earth tide signal is used for calibration. However, the strainmeter deployed is unable to resolve tides, so it has not yet been calibrated and the basic phase data are used instead. It is expected that the strain is proportional to the optical phase so plots of the optical phase (e.g. Figure 52, Figure 53) are expected to resemble plots of strain. As a result, the phase data from the strainmeter will be referred to as apparent strain until calibration can be completed.

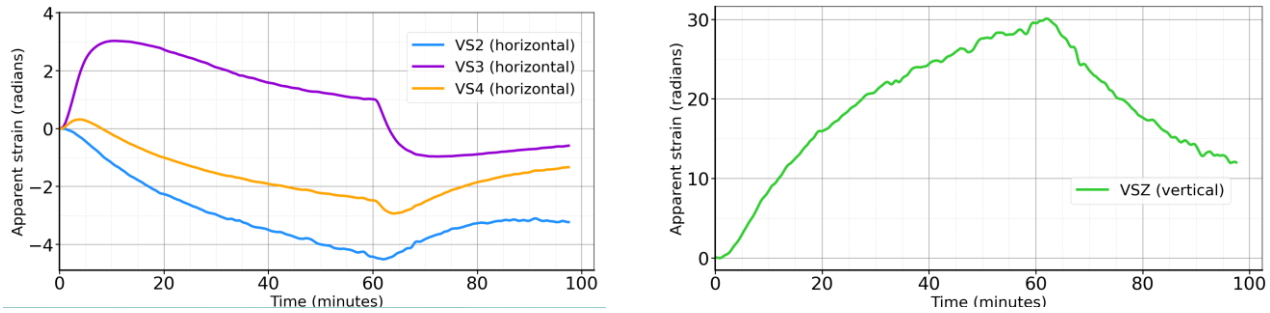

Figure 52. Apparent horizontal and vertical strains measured as a function of time in the vadose zone during a 1-hour constant rate pumping test. The pumping starts at t=0 min. Apparent strain is given as radians of optical phase measured by the strainmeter, which will be converted to actual strain after calibration

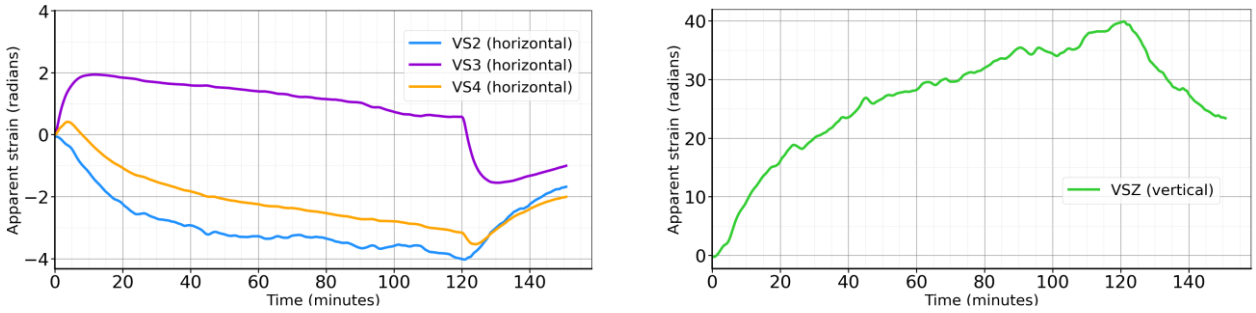

Figure 53. Apparent horizontal and vertical strains measured as a function of time in the vadose zone during a 2-hour constant rate pumping test. The pumping starts at t=0 min. Apparent strain is given as radians of optical phase measured by the strainmeter, which will be converted to actual strain after calibration.

The apparent vertical strains time series (in green in Figure 52 and Figure 53) are similar to the pattern at the drawdown at SWL-5. The strain increases to 30 radians after pumping for 1 hour and to 40 radians after pumping for 2 hours indicating tension in the vertical direction as the water is pumped out of the aquifer.

The trends of the apparent horizontal strains are consistent among the different pumping tests. VS2 decreases to -4 radians during pumping, and it recovers after that. The VS2 time series resembles of VSZ with a change in sign (Figure 52, Figure 53). The VS3 time series increases at the start of pumping and reaches a maximum of 2 to 3 radians approximately 10 minutes later, and then it slowly decreases but remains positive while the pump is on. When the pump is turned off, the VS3 time series drop and become negative indicating compression. The VS4 dataset also increases initially, but the rate is slower than at VS3, and it reaches a peak at 0.4 radians and then decreases and changes sign after approximately 8 minutes of pumping.

The results indicate that apparent strains are entirely compressive at VS2 and entirely tensile at VS3 during pumping, and the apparent strain switches from tensile at the beginning to compressive for most of the test at VS4. The vertical strain is tensile during pumping, and in general, the signs of apparent strains reverse during recovery after the pump is turned off.

Four more pumping tests were conducted to study the consistency of the strain measurements (Figure 54). The apparent strains were calibrated to show the actual strains caused by water displacement using the numerical model presented below. The average strain was calculated using data from the 6 pumping tests for t = 0 min to t = 60 min. The average strain during recovery was calculated using the 1h pumping test data only as the numerical model was built to represent strain during a 1h pumping test. The variations at the end of the pumping tests are different for each direction. The strains measured at VS2 and VZ show the biggest variations with 3 με and 2.5 με, the standard deviations associated with those dataset are ± 0.54 and ± 2.4. The VS3 time series change by 1 με at t = 60 min and the standard deviation is ± 0.33. The strains measured by VS4 present the smallest variation with a maximum change of 0.5 με at t = 60 min, the standard deviation of 0.13 is also the smallest. Strains measured by the direct-push strainmeter at the Clemson Bull Farm are consistent over time as shown by those measurements.

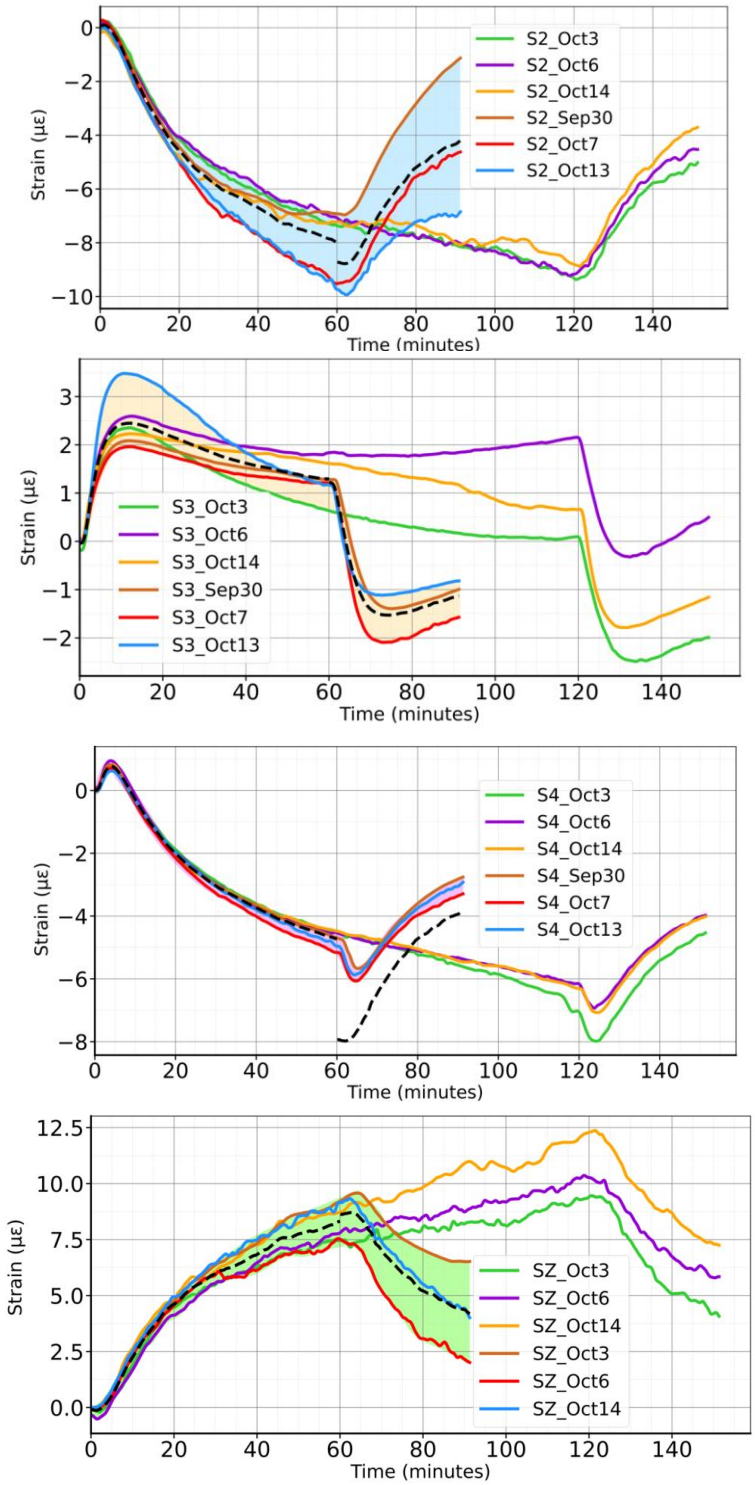

Figure 54. Horizontal (S2, S3, S4) and vertical (SZ) strains measured as a function of time in the vadose zone during 6 pumping tests. Pumping starts at t=0 min. Three tests were 1h pumping tests, the pump was turned off at t= 60min. The pump was turned off at t = 120 min for the other tests. Average strains during pumping and during recovery (black, dashed line) were calculated and a range of strain values during a one hour pumping test was determined (colored area).

SIMULATIONS

Data from the field tests differ from results from previous tests using tensor strainmeters where the signs of the horizontal strains were opposite those at the vertical strains. For example, injection tests at the North Avant Field (OK) created horizontal tensile strains and vertical compressive strains (Murdoch et al., 2021). One of the goals of the field tests was to evaluate the feasibility of interpreting data from a strainmeter that has been pushed in, and the preliminary results indicate that the basic response is fundamentally different from other strainmeters, which were grouted.

A simulation of the well test was developed to represent the field site in an effort to evaluate the observed strain signal. The primary goal of the simulation was to explain the observed strain time series and to understand why it differed from previous field data. Another goal was to evaluate the feasibility of calibrating the optical phase change to strain.

Conceptual model

The simulation is based on a conceptual model that represents the Clemson Bull Farm site described in Chapter Two. It assumes an aquifer and vadose zone 20 m thick and of essentially infinite lateral extent. The three monitoring wells and the direct push strainmeter were included along with a pumping well with wellbore storage.

Numerical model

A finite element model was set up using geometry and properties from the conceptual model of the Clemson Bull Farm Site. The model was set up and analyzed using COMSOL Multiphysics 6.0.

Geometry and properties

The geometry of the model was formulated in 2D axisymmetric coordinates consisting of two zones representing (1) the saturated saprolite and (2) the unsaturated saprolite in the vadose zone. Each zone is 10 m thick and they extend from r = 0.076 m to r = 10,000 m. The inner radius is the wall of the wellbore, and the outer boundary was large so it has no effect on the processes in the vicinity of the wells. The properties for the two zones are summarized in Table 5. Those values were chosen for the field site based on previous field studies.

Table 5. Material and Fluid Properties used in the numerical model

Saturated Saprolite	Elastic modulus, E	0.5×10^8	Pa
	Poisson's ratio, ν	0.3	
	Porosity	0.3	
	viscosity	0.001	Pa*s
	Density, ρ	2,000	kg/m^3
Vadose zone	Elastic modulus, E	10^8	Pa
	Poisson's ratio, ν	0.3	
	Porosity	0.3	
	viscosity	0.001	Pa*s
	Density, ρ	2,000	kg/m^3

Physics

The simulation assumes the saturated zone deforms as a fully coupled poroelastic material, and the vadose zone deforms as an elastic material that is coupled mechanically to the underlying saturated zone. It is assumed that the pumping tests were brief enough so any changes in fluid pressure in the vadose zone resulting from the pumping tests could be ignored.

The simulation assumes the saprolite and the saturated zone deform as a linear elastic solid. Conservation of momentum requires

$$\nabla \cdot \sigma = 0 \tag{10}$$

where σ is the total stress tensor. Quasi-static conditions are assumed, and body forces are ignored. The stresses are related to strains through Hooke's Law as

$$\begin{aligned}
\sigma_{xx} &= 2G\varepsilon_{xx} + \lambda\varepsilon_{kk}\sigma_{ij} \\
\sigma_{yy} &= 2G\varepsilon_{yy} + \lambda\varepsilon_{kk} \\
\sigma_{zz} &= 2G\varepsilon_{zz} + \lambda\varepsilon_{kk} \\
\sigma_{xy} &= 2G\varepsilon_{xy} \\
\sigma_{xz} &= 2G\varepsilon_{xz} \\
\sigma_{zy} &= 2G\varepsilon_{zy}
\end{aligned} \tag{11}$$

which can be written in a more compact form using index notation

$$\sigma_{ij} = 2G\varepsilon_{ij} + \lambda\varepsilon_{kk}\delta_{ij} - \alpha P\delta_{ij} \tag{12}$$

where δ_{ij} is the dirac delta and *G* is the shear modulus, and λ is Lame's constant. These constants are related to Young's Modulus, *E*, and Poisson's ratio, ν, using

$$\begin{aligned}
\lambda &= \frac{E\nu}{(1+\nu)(1-2\nu)} \\
G &= \frac{E}{2(1+\nu)}
\end{aligned} \tag{13}$$

The strains in the saprolite are defined as displacement gradients, so the normal strains are

$$\begin{aligned} \varepsilon_{xx} &= \frac{\partial u_d}{\partial x} \\ \varepsilon_{yy} &= \frac{\partial v_d}{\partial y} \\ \varepsilon_{zz} &= \frac{\partial w_d}{\partial z} \end{aligned} \tag{14}$$

and shear strains are

$$\begin{aligned} \varepsilon_{xy} &= \frac{1}{2}\left(\frac{\partial u_d}{\partial y} + \frac{\partial v_d}{\partial x} \right) \\ \varepsilon_{yz} &= \frac{1}{2}\left(\frac{\partial v_d}{\partial z} + \frac{\partial w_d}{\partial y} \right) \\ \varepsilon_{zx} &= \frac{1}{2}\left(\frac{\partial w_d}{\partial x} + \frac{\partial u_d}{\partial z} \right) \end{aligned} \tag{15}$$

where the displacement vector is

$$\mathbf{u} = u_d \mathbf{i}_x + v_d \mathbf{i}_y + w_d \mathbf{i}_z \tag{16}$$

The volumetric strain is given by

$$\varepsilon_{kk} = \varepsilon_{11} + \varepsilon_{22} + \varepsilon_{33} \tag{17}$$

The fluid flow in the saprolite was modeled assuming conservation of mass

$$0 = \nabla(\rho_w q) + \rho_w \alpha_b \frac{\partial \varepsilon_{kk}}{\partial t} + \frac{\rho_w \phi}{K_f} \frac{\partial p}{\partial t} \tag{9}$$

where ρ_w is the density of water, q is the volumetric flux vector of water, ϕ is porosity, K_f is the bulk modulus of water and p is the pore pressure.

Darcy's Law gives

$$q = -\frac{k}{\mu}(\nabla \mathrm{p} + \rho_w g \nabla z) \quad (10)$$

where k is permeability, μ is fluid viscosity and g is gravitational acceleration.

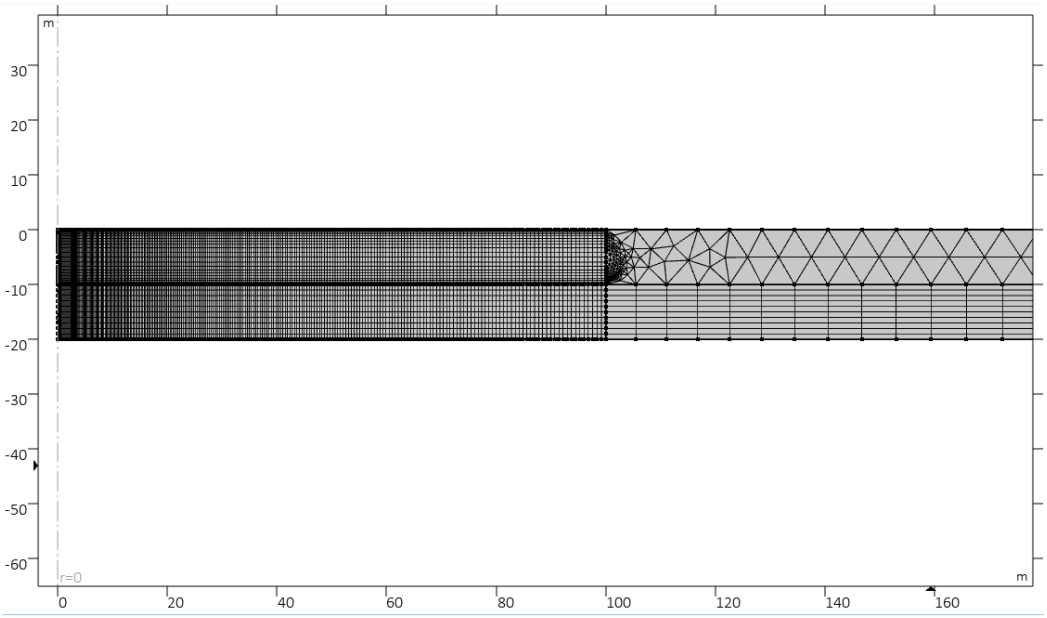

Figure 55. Distribution of the mesh elements.

Boundary conditions were defined for fluid flow and stresses on the solid. The upper limit of the model is bounded by no-flow and stress-free conditions to represent the ground surface. The saprolite is underlain by an unfractured gneiss layer with a permeability much less and elastic modulus much greater than the saprolite. The gneiss was represented with a no-flow and a roller boundary (zero normal displacement). The outer lateral boundary has constant heads and roller conditions. The well was represented as a boundary where the hydraulic head is uniformly distributed and varies in time. This was implemented using an ordinary differential equation to represent wellbore storage using standard methods. A constant pumping rate of 3 gpm was applied to the wellbore, and both removed water from storage in the wellbore and caused flow in from the aquifer.

Mesh

The mesh consisted of 12,643 triangular elements of an average quality of 0.96. A fine mesh was built for the area of interest (0-100 m radially) with a maximum element size of 0.5 m. Beyond the area of interest, a coarser triangular mesh was used with a maximum element size of 15.9 m (Figure 55).

Results

A simulation was conducted by assuming pumping at 3 gpm for 60 minutes followed by 60 minutes of recovery. The simulation was executed five times using different values of intrinsic permeability, ranging from 1 x 10^{-13} to 5 x 10^{-13} m^2.

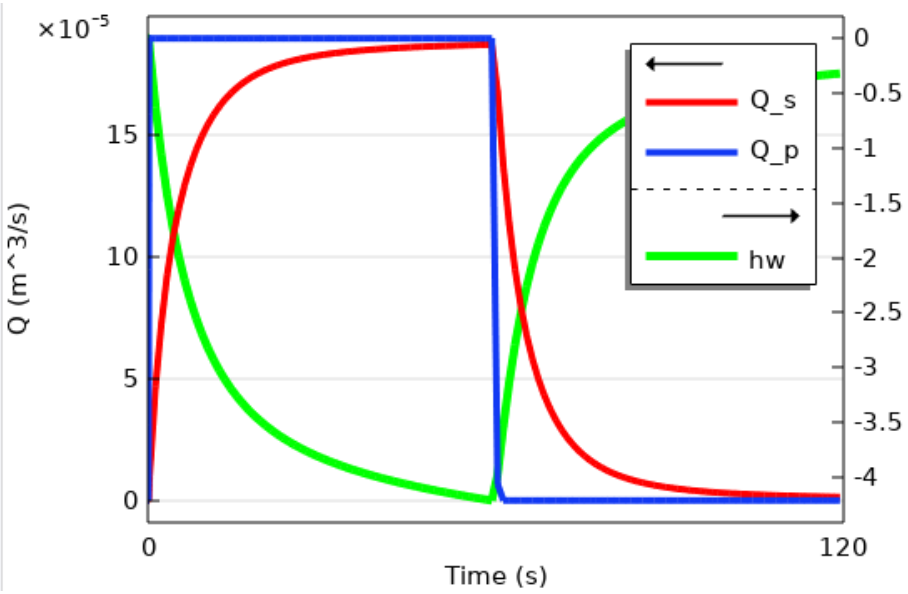

Figure 56. Flow rate from the pump (Q_p) and into the well (Q_s) and the hydraulic head in the well (h_w) during the constant rate pumping tests showing effects of wellbore storage.

With an intrinsic permeability of 3 x 10^{-13} m^2, the flow rate at the well changed as a rapid, but smooth step imposed by the boundary conditions, but the flow rate from the aquifer into the well ramped up over the first 30 to 40 minutes and reached the applied rate at the end of the pumping period (Figure 56). Water removed from wellbore storage accounts for the difference

between the flowrate out of and into the well. The hydraulic head in the well decreased with time during pumping and dropped by more than 4 m at the end of pumping. The head recovered to approximately 0.4 m of the initial head one hour after pumping stopped (Figure 56).

The pressure change in the aquifer caused by pumping propagates radially outward from the well and its advance is characterized by the 0.01 m drawdown contour. This contour is a few meters from the well after 1 minute of pumping and is approximately 10 meters from the well after 30 minutes (Figure 57).

The pressure change in the aquifer causes strain in the overlying vadose zone, and principal strains are radial, ε_{RR}, circumferential, $\varepsilon_{\phi\phi}$, and vertical, ε_{ZZ}. The distribution of radial strain is characterized by a cone-shaped zone of compressive (negative) ε_{RR} surrounded by a zone of tensile strain (Figure 57). The radial strain is zero along the inwardly inclined band where the inner zone of compression crosses over to the outer tensile zone (red line in Figure 57). The bottom of the band is near the well and the *cross-over band* is inclined roughly at a 45° angle so the upper shallow end of the band is approximately at r = 10 m from the well soon after pumping starts (e.g 1 minute in Figure 57). The compressive zone expands outward with time along with the pressure, and this causes the cross-over band to move radially outward. For example, the reference point at r = 10 m in Figure 57 is a few meters beyond the cross-over band at t = 1 min, but it is only about 1 m beyond the band at t = 30 min, and the cross-over band is several m beyond the reference point at t = 60 min. This behavior shows that ε_{RR} would change sign and go from tensile to compressive strain between 30 and 60 minutes of pumping.

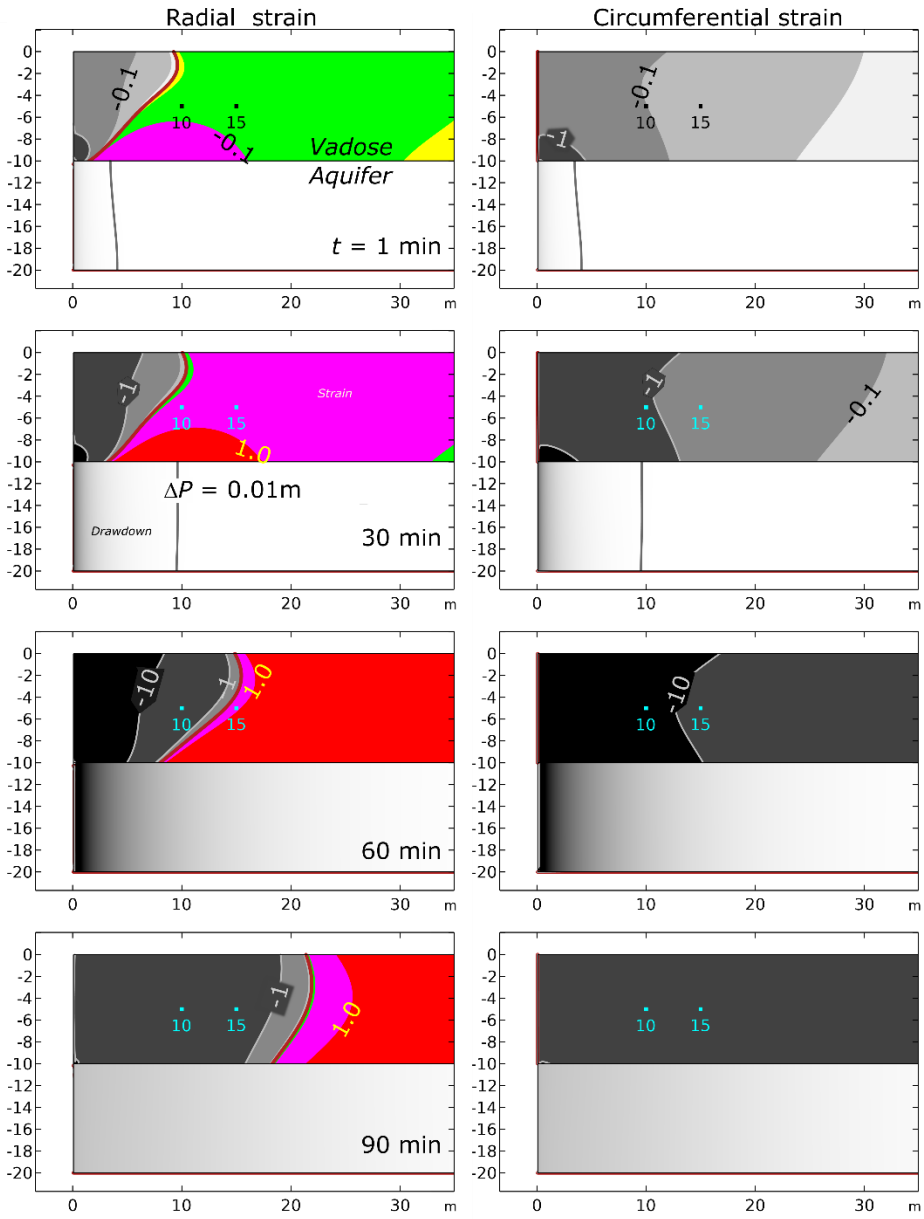

Figure 57. Radial and circumferential strains in the vadose zone (upper rectangle in each panel) and drawdowns in the aquifer (grey tone in lower rectangles) at different times during 60-minute-long pumping test. Colors are positive (tensile) strains, grey tones are negative (compressive strains). Bottom panels are during recovery. Dots labeled “10” are at the location of the strainmeter (r = 10m, z = -5m), dots labeled “15” are at the assumed effective location of the strainmeter.

The strainmeter measures three strains at different orientations separated by 45°. The details of the time series of the three strains will vary depending on their orientation, but they will be bounded by the magnitudes of the principal strains, ε_{RR} and $\varepsilon_{\phi\phi}$. The principal strains were calculated at the location of the strainmeter, r = 10 m, z = 4m, and ε_{RR} was positive briefly at the beginning of pumping but went negative quickly and was negative during most of the test (Figure 59). This is consistent with the cross-sections where the reference point at r = 10 m is in a region of positive strains only early in the test. Based on the results in Figure 52 and Figure 53 it was apparent that a point at a larger radial distance would be in the region of positive strains longer, so it was assumed that the effective location of the point was at r = 15 m, z = -5 m (the other reference point in Figure 57).

The hydraulic diffusivity controls how rapidly the drawdown propagates outward from the well, and this will affect the strain time series. A series of simulations was conducted using permeability values ranging from 1 x 10^{-13} to 5 x 10^{-13} m^2 to evaluate this effect (Figure 60). The results for the case on the low end of the range indicate that ε_{RR} increases throughout the test, but the data indicate that VS2 increases and reaches a maximum and then decreases (Figure 52). This effect only occurs in aquifers with permeabilities greater than 3 x 10^{-13} m^2. The times series of ε_{RR} for k = 5 x 10^{-13} m^2 decreases more rapidly than the observed data (Figure 52). This suggests that the data can bound the permeability to between 3 and 5 x 10^{-13} m^2. For comparison, the permeability estimated using the constant rate pumping test was 3.7 x 10^{-13} m^2.

Strains at r = 15 m and z = -5 m from the simulations using k = 4 x 10^{-13} m^2 were used to evaluate the observed strains. The three strains separated by 45° were estimated using tensor rotation and compared to the observed strains (Figure 58). As an example, the strains determined using an angle of 98° between VS2 and the radial direction predict the strain time series b in

Figure 59 that are similar to the observed data (Figure 52). The numerical strain data for VS2 decreases to -8 με when pumping starts and increases when the pump is stopped. The same phenomenon is seen in the observed data for VS2 but the minimum is -4.5 radians. The numerical strain for VS3 is positive during the entire pumping test. It increases to around 2 με for the first 20 minutes then slowly decreases to 1.5 με and drops below zero at 65 minutes. This trend is also seen in the observed data for VS3. It increases to 3 radians at the beginning of pumping, reaching its maximum value at t = 10 min. It then progressively decreases to 1 radian during the rest of pumping. A sudden drop below 0 radian happens after the pumping was turned off at 62 minutes. The observed VS4 strain data looks similar to the numerical VS4 data. However, the numerical strain decreases to -5 με while the observed strain minimum value is -3 radians. Both minimums are reached at t = 65 min.

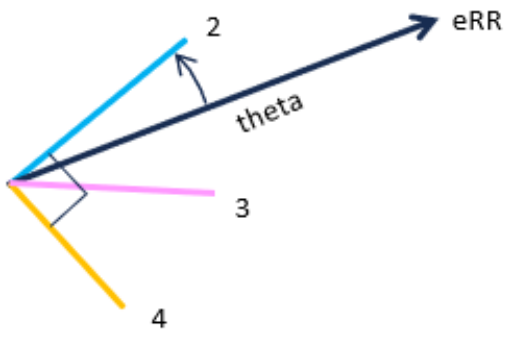

Figure 58. Orientations of the three horizontal strains, VS2, VS3, VS4 relative to the principal radial strain. Theta is the angle between the line from the pumping well to the strainmeter and the direction of VS2. VS3 is 45^{o} from VS2.

(a)

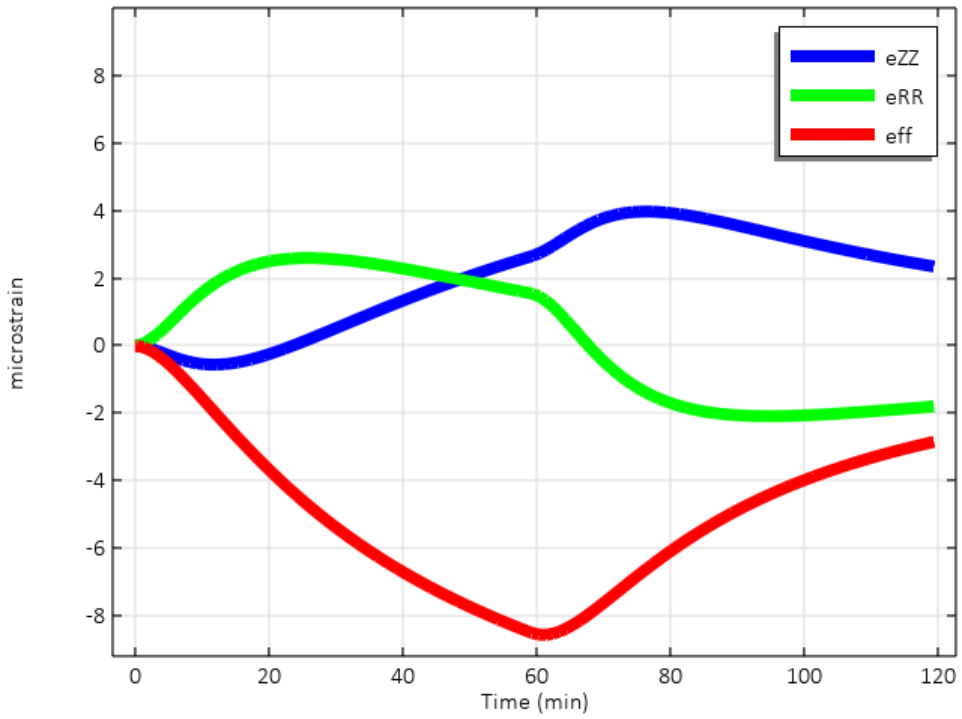

(b)

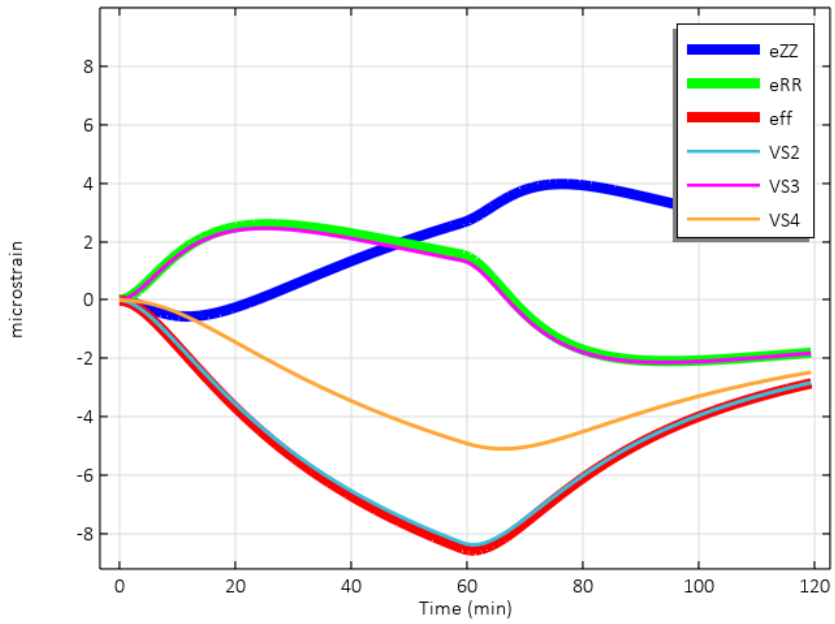

Figure 59. Three principal components of strain at r = 10m and z = -5.5m. The two horizontal strains are nearly always negative, contrary to the field data. (b) Three principal components of strain (thick lines) and non-principal horizontal normal strains at $\alpha = 75^{o}$ (thin lines).

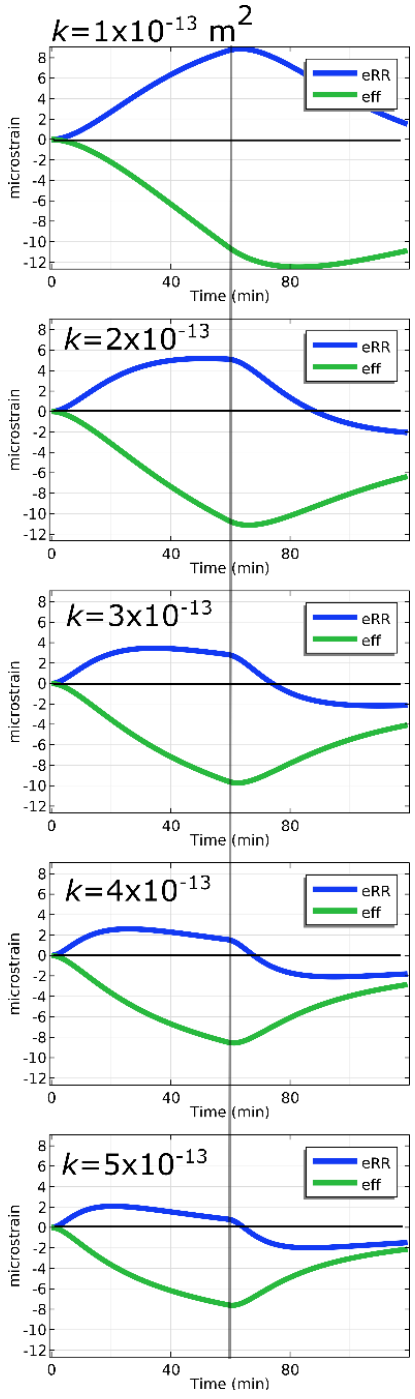

Figure 60. Principal strains simulated using different values of permeability in the aquifer at r = 15m, z = -5m.

The average strains in each direction were calculated using the data from 6 pumping tests (Figure 54). The average strain data were used to find a calibration factor to convert the optical phase to strain for each direction by comparing the average field data (Figure 54) to the results from the simulations (Figure 59 and Figure 60). The orientation of the strainmeter relative to a line between the strainmeter and the well was also determined. The calibration factors and orientation were estimated by manually adjusting values and evaluating the goodness of fit between the data and the simulations.

The results indicate the simulations are remarkably similar to the field data after calibration (Figure 60). The calibration factors for horizontal strains are in the range of 1 and 2 $\mu\varepsilon/\phi$, and the factor is approximately an order of magnitude less for the vertical strain component (Table 6). The orientation factor was estimated to be $\theta = 98^{o}$, where θ is defined in Figure 58. The azimuth of a line from the pumping well to the strainmeter is approximately 330^{o}, according to the site map in Figure 6. It follows that the azimuth of VS2 is approximately 232^{o}, and azimuths of all the components are given in Table 6. Calibration factors determined to convert optical phase change, and the azimuth of each component measured by the strainmeter.

Table 6. Calibration factors determined to convert optical phase change, and the azimuth of each component measured by the strainmeter.

	$\mu\varepsilon/\varphi$	Azimuth
VS2	2.2	232
VS3	1.15	277
VS4	2	322
VZ	0.31	--

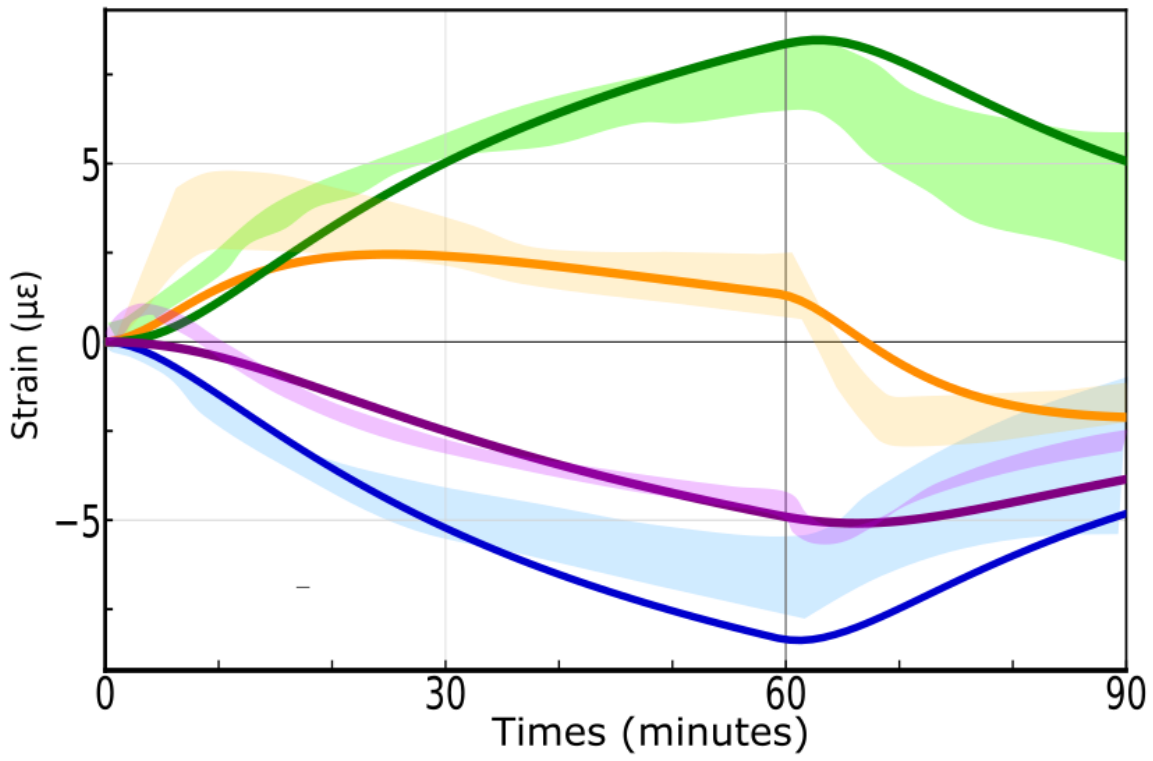

Figure 61. Three non-principal horizontal strain components at r = 10 m and z = -5.5 m with α = 98° (lines, green = VZ, orange = VS3, purple = VS4, blue = VS2) and the ranges of calibrated horizontal strains (colored area) measured by the strainmeter in the vadose zone during a 1-hour constant rate pumping test

Chapter Five: DISCUSSION

This research demonstrates that it is feasible to characterize multiple components of strain at high temperatures and in unconsolidated materials using optical fiber sensors. This advances the capabilities to measure strain in geothermal reservoirs, or in unconsolidated material overlying these reservoirs. Changes in fluid pressure or temperature as a result of hydraulic fracturing, or heat production from the reservoir will cause strains that can be used to characterize material properties that affect reservoir performance. This research also demonstrates that it is feasible to create an instrument that can measure strains at geothermal reservoir temperature and this information has the potential to improve reservoir performance.

SPLIT-SLEEVE STRAINMETER

This work showed that a split-sleeve strainmeter can measure deformation caused by an applied load for 58 days at 200°C and 230°C. This establishes the ability to measure strain above the *required* and *desired* temperature goals. The laboratory test described in Chapter Three has continued and the temperature was increased to 255°C. The split-sleeve strainmeter has responded to applied loads for 70 days, and a total of 128 days above 200°C. The temperature will be increased in an effort to evaluate the upper temperature limit, and it is still feasible that it could reach the *optimum* goal of 300°C. Regardless of the final outcome, current results indicate that the composite packaging developed for the split-sleeve strainmeter is capable of functioning at reservoir temperatures for extended periods.

The sensor system used in the split-sleeve strainmeter experiments described in Chapter Three differs from the one that would be needed to meet the strain magnitude goal of 1 nε. The FBGs used in the split-sleeve strainmeter can resolve approximately 0.1 με, which is sufficient

for many applications. For example, FBGs could likely resolve strains caused by hydraulic fractures within 100 m of the fracture, according to Figure 9. However, high resolutions will be needed for more general applications. The Mach-Zehnder interferometer described in Chapter Four is capable of meeting the strain resolution goals, so including a MZI in the split-sleeve strainmeters is on the path toward field implementation. Creating a MZI that will function at high temperatures will require optical couplers that can perform at those temperatures. The 2x2 and 3x3 couplers that were used in the MZI described in Chapter Four were based on acrylate-coated fiber, which is rated for temperatures less than 80°C. However, optical couplers created with polyimide fiber rated for high-temperature services may create a MZI that can function in geothermal reservoirs. This is one option for creating a split-sleeve strainmeter that can meet both the temperature and strain performance goals.

Another option for meeting performance goals is to use the high-temperature split-sleeve packaging described in Chapter Three with optical fiber interrogated using a DAS interrogator. Coils of polyimide-coated optical fiber could be embedded in the split-sleeve and interrogated using phase-OTDR methods. This would require more complex calibration procedures, but it would avoid risks of using optical couplers at elevated temperatures. The seven splices required to join the couplers into a MZI (Figure 3), and the couplers themselves will be more likely than unmodified optical fiber to fail at high temperatures.

In this sense, the system described in Chapter Three is a package for securing optical fiber to a casing at elevated temperatures. This package could be used with a variety of different optical fiber sensors for a variety of different applications.

DIRECT-PUSH STRAINMETER

Many applications, including some overlying geothermal reservoirs, require deploying strainmeters in unconsolidated formations, and this research has made significant contributions toward those applications. Chapter Four describes the first combination of FBGs and MZI sensors cast in urethane resin with Young's modulus similar to soil. It was shown how the FBGs can be used to characterize the relationship between applied pressure and strain, and to calibrate the optical phase of the MZI to strain. Results in Chapter Four (Figure 46 and Figure 47) demonstrate the feasibility of calibrating a MZI using data from FBGs. This addresses a long-standing calibration problem that will be utilized in future applications.

Matching the elastic modulus of a strainmeter to that of the enveloping soil would improve the sensitivity compared to using a strainmeter in a steel tube, which is much stiffer than soil. This motivated the approach of casting the strainmeter from urethane resin with a Young's modulus similar to soil. It was shown that it is feasible to create a strainmeter using this approach, but practical constraints remain unresolved. The effective elastic modulus (applied pressure/circumferential strain) of early prototype strainmeters cast from urethane resin with an axial hole was in the range of 66 MPa, which is similar to soil. However, the optical fiber in this device broke during deployment, apparently because the low modulus resulted in large deformations. A variation on the design that embedded a 3/4 -inch threaded steel rod in the casting had been successfully deployed without breaking the optical fiber, so this design was used when building the urethane strainmeter with FBGs and MZI sensors. Data from calibration experiments in a pressure chamber indicate an effective modulus of 9,800 MPa, which is 100 stiffer than soil Simulations indicate that the steel rod is responsible for the additional stiffness. The optical fibers associated with the FBG and MZI sensors broke during handling, so the device

was never tested in the field. Two other strainmeters with a similar design were successfully deployed without breaking the fiber, so it is thought that it could have been successfully deployed. However, the large effective modulus caused by the reinforcing bar indicates that design modifications will be needed to meet the goal of matching the soil modulus.

The results shown in Chapter Four indicate that modulus matching may be unnecessary to obtain meaningful measurements in soil. The effective modulus of the strainmeter used to generate the data in Figure 54 is likely in the range of several 10s of GPa, which is two to three orders or magnitude more than the enveloping saprolite. This large contrast will cause the strain measured by the strainmeter to be less than the strain that would have occurred in the soil in the absence of the strainmeter. This problem can be addressed by in-situ calibration, which requires correlating a known strain to the output of the strainmeter. Other applications have used calculated earth tide strains for this purpose, but earth tides were not measured by the instrument used for this work. Results in Figure 61 demonstrate that it can be feasible to calibrate a tensor strainmeter using strains calculated from a pumping test. The data are sensitive to the calibration factor relating phase to strain, and the shapes of the time series are sensitive to the orientation of the strainmeter.

The results indicate that it can be feasible to calibrate a tensor strainmeter using data from a pumping, but this approach has some drawbacks. It requires that the Youngs modulus of the aquifer and vadose zone is known independently, and it assumes the aquifer is homogenous and isotropic. Interestingly, though, the permeability of the aquifer could be estimated from the shapes of the principal strains, and it was independent of calibration (e.g Figure 60).

The simulation results that fit the observed horizontal strain data are from a radial distance 5 m beyond the actual location of the strainmeter. The shapes of the simulated

horizontal strains from the actual location are distinctly different from the field data, so the alternative distance was used. One possible explanation is that the high contrast in modulus between the strainmeter and the soil perturbed the strain field, essentially by compressing the strain cross-over band further inward than it would have been if the strainmeter was absent. A 3D analysis of the strain will be required to evaluate this possibility, so for now it remains untested.

Despite the uncertainty regarding location, the shape of the simulated strain data was sensitive to the intrinsic permeability of the aquifer. A parameter sweep was able to bound the permeability to between 3 and 4 x 10^{-13} m^2, whereas independent estimates of permeability from a pumping test yielded 3.7 x 10^{-13} m^2. These results are based on shapes of the principal strains required to match the field data and are independent of calibration for both the strain magnitude and the orientation of the strainmeter, the result was obtained prior to calibration.

This was the first attempt at using a strainmeter deployed using direct-push and the results of repeat tests are consistent to within less than 20 percent. Moreover, uncalibrated results were used to estimate permeability, and simulations were used for the first time to calibrate the instrument. These findings indicate that this method of deploying a strainmeter can provide important scientific insights that are similar to strainmeters that are grouted in place. Importantly, though, the strainmeter deployed by direct push can be recovered and reused, whereas strainmeters that are grouted in place are permanent and cannot be reused elsewhere.

Chapter Six: CONCLUSION

The objectives of this research are to evaluate the feasibility of characterizing strains in geologic media at elevated temperatures and unconsolidated materials in order to improve applications of strain data in geothermal settings. A split-sleeve strainmeter design was developed using high-temperature composite material and tested by clamping it onto a pipe, heating it to 200°C and 230°C and applying repetitive loading for two months. Four strain sensors embedded in the strainmeter measured different components of bending of the pipe. The strainmeter responded to strain consistently throughout the testing period with strains from different locations and orientations that differed in magnitude and sign, The axial strain sensor closest to an actuator was in tension when load was applied and the opposite side experienced compression. The observed deformations were confirmed by comparing the measured strain data to the results of a numerical model. The strainmeter has continued to perform as designed for another three months at a temperature of 255°C, and the test is ongoing. These results indicate that the split-sleeve packaging developed for this research is a viable design for a strainmeter that can function at temperatures similar to geothermal reservoirs.

A novel method of deploying strainmeters by pushing them into unconsolidated material was evaluated using both a new and an existing design. The new design is created by embedding optical fiber sensors in a urethane casting with a Shore 80 A hardness. The Young's modulus of the urethane casting is similar to that of saprolite at the Clemson Bull Farm field site. The strainmeter included co-located fiber Bragg grating (FBG) sensors and a Mach-Zehnder interferometer (MZI) oriented circumferentially. Lab tests in a pressure chamber demonstrated that strain measurements from the FBGs correlate with optical phase data from the MZI, providing a novel calibration method for the MZI. The effective modulus (ratio of pressure over

strain) is 66 MPa for a cylindrical casting with an open axial hole mounted on a threaded rod, whereas it is 9,800 MPa when the threaded rod is embedded in the casting. Young's modulus of saprolite at the field site is 50 to 100 MPa, so the effective modulus of the strainmeter with the open axial hole is similar to that of saprolite, but embedding the rod in the casting creates an instrument that is significantly stiffer than saprolite.

A tensor strainmeter that measures strain in three radial and one vertical directions using Michelson interferometers was deployed by direct push at the field site and used to measure strain during six constant-rate pumping tests. This instrument was designed to be grouted in rock, but it was repurposed for this experiment. It is contained in a steel tube and was much stiffer than the soil, which could have affected its performance, but it was also much stronger than the urethane casting and therefore it was less vulnerable to damage during deployment. Transducers in three monitoring wells measured drawdown during the pumping tests.

Strain data from the six pumping tests (three tests with 1 hr of pumping and three tests with 2 hrs of pumping) are generally repeatable. One of the horizontal strains was compressive during pumping, and one was tensile, whereas the third one was initially tensile but then it decreased and changed sign becoming compressive after pumping for approximately 10 minutes. A numerical simulation of the pumping tests using a poroelastic model predicts strain time series that are sensitive to permeability, location, orientation and other factors. The shapes of the strain time series field data are distinctive and constrain the permeability to 3 and 4 x 10^{-13} m^2 using a manual fitting procedure. Drawdown data were used with the Neuman (1974) solution to estimate a permeability of 3.7 x 10^{-13} m^2 (+/- 0.4 x 10^{-13} m^2), providing independent validation of the permeability estimate from the strain data. The strainmeter was uncalibrated and unoriented, so the simulations were used to estimate calibration factors and orientation. The simulated strains

are sensitive to orientation of the strainmeter and they bound the orientation to within a few degrees using manual fitting.

These results demonstrate that data useful for characterizing aquifers can be measured using a strainmeter that is deployed temporarily using direct push in the vadose zone above an aquifer. This is significant because it opens the door to the deployment of reusable strainmeters in the vadose zone to characterize underlying aquifers or reservoirs. This could advance understanding of geothermal reservoirs, but it will also have a variety of other applications in hydrogeology, energy production, geotechnical characterization, waste storage, and related technologies.

REFERENCES

Aoyama K., Mogi T., Suzuki K., Sasaki J., Yamaya Y. (2022). Magnetotelluric study on a vapor-dominated geothermal reservoir in the Matsukawa area, Japan. In *Geothermics* (Vol. 101). https://doi.org/10.1016/j.geothermics.2022.102362.

Arfken, G. B., Weber, H. J., & Harris, F. E. (2013). Integral Transforms. In *Mathematical Methods for Physicists*. 963–1046. Elsevier. https://doi.org/10.1016/B978-0-12-384654-9.00020-7

Assad, M. E. H., Aryanfar, Y., Radman, S., Yousef, B., & Pakatchian, M. (2021). Energy and exergy analyses of single flash geothermal power plant at optimum separator temperature. In *International Journal of Low-Carbon Technologies* (Vol. 16, Issue 3), 873–881. https://doi.org/10.1093/ijlct/ctab014

Bertholds, A., & Dandliker, R. (1987). Deformation of Single-Mode Optical Fibers Under Static Longitudinal Stress. In Journal of Lightwave Technology (Issue 7).

Bourne-Webb, P., Burlon, S., Javed, S., Kürten, S., & Loveridge, F. (2016). Analysis and design methods for energy geostructures. In *Renewable and Sustainable Energy Reviews* (Vol. 65). 402–419. Elsevier Ltd. https://doi.org/10.1016/j.rser.2016.06.046

Breede, K., Dzebisashvili, K., Liu, X., & Falcone, G. (2013). A systematic review of enhanced (or engineered) geothermal systems: past, present and future. In *Geothermal Energy* (Vol. 1, Issue 1). SpringerOpen. https://doi.org/10.1186/2195-9706-1-4

Campanella, C. E., Cuccovillo, A., Campanella, C., Yurt, A., & Passaro, V. M. N. (2018). Fibre Bragg Grating based strain sensors: Review of technology and applications. In *Sensors (Switzerland)* (Vol. 18, Issue 9). MDPI AG. https://doi.org/10.3390/s18093115

Chang, J., Niu, H., & Wu, D. (2017). High performance polyimide fibers. In *Structure and Properties of High-Performance Fibers*, 301–323. Elsevier Inc. https://doi.org/10.1016/B978-0-08-100550-7.00012-7

Cverna, F., & ASM International. (2002).ASM Ready Reference: Thermal Properties of Metals (Materials Data Series). Materials Park, Ohio: ASM International.

Department of Energy. (2019). GeoVision: Harnessing the Heat Beneath Our Feet. http://www.osti.gov/scitechonlineordering:http://www.ntis.gov/help/ordermethods.aspx

Detournay, E. (2016). Mechanics of Hydraulic Fractures. In *Annual Review of Fluid Mechanics* (Vol. 48). 311–339. https://doi.org/10.1146/annurev-fluid-010814-014736

Dewolf, S., Wyatt, F. K., Zumberge, M. A., & Hatfield, W. (2015). Improved vertical optical fiber borehole strainmeter design for measuring Earth strain. In *Review of Scientific Instruments* (Vol. 86, Issue 11). https://doi.org/10.1063/1.4935923

DiPippo, R. (2013). Geothermal double-flash plant with interstage reheating: An updated and expanded thermal and exergetic analysis and optimization. In *Geothermics* (Vol. 48), 121–131. https://doi.org/10.1016/j.geothermics.2013.07.006

EGI. (2018). Frontier Observatory for Research in Geothermal Energy-Phase 2B.

Energy Information Administration, U. (2022). *Monthly Energy Review – November 2022*. www.eia.gov/mer

Feraboli, P., Gasco, F., Wade, B., Maier, S., Kwan, R., Masini, A., Deoto, L., & Reggiani, M. (2011). *LAMBORGHINI "FORGED COMPOSITE ® " TECHNOLOGY FOR THE SUSPENSION ARMS OF THE SESTO ELEMENTO*.

Galantino C., Beyers S., Anderson C., Tester J. (2020). Optimizing Cornell's future geothermal district heating performance through systems engineering and simulation. In *Energy and Buildings* (Vol. 230). https://doi.org/10.1016/j.enbuild.2020.110529

Gandy, D. (2007). Carbon Steel Handbook. www.epri.com

Gallup, D. L. (2009). Production engineering in geothermal technology: A review. In *Geothermics* (Vol. 38, Issue 3). 326–334. https://doi.org/10.1016/j.geothermics.2009.03.001

Hariharan, P. (1992). Basics of interferometry. Academic Press.

Hariharan, P. (2007). Basics of INTERFEROMETRY (Second Edition). Academic Press.

Held, S., Genter, A., Kohl, T., Kölbel, T., Sausse, J., & Schoenball, M. (2014). Economic evaluation of geothermal reservoir performance through modeling the complexity of the operating EGS in Soultz-sous-Forêts. In *Geothermics* (Vol 51). 270–280. https://doi.org/10.1016/j.geothermics.2014.01.016

Huebner, M. T., Hatcher, R. D., & Merschat, A. J. (2017). Confirmation of the southwest continuation of the cat square terrane, southern appalachian inner piedmont, with implications for middle paleozoic collisional orogenesis. In *American Journal of Science* (Vol. 317, Issue 2), 95–176. Yale University. https://doi.org/10.2475/02.2017.01

IEA Geothermal. (2022). *2021 Annual Report*.

Intergovernmental Panel on Climate Change. Working Group III, & Edenhofer, O. (2014). Climate change 2014 : mitigation of climate change : Working Group III contribution to the Fifth Assessment Report of the Intergovernmental Panel on Climate Change.

Janani, R., Majumder, D., Scrimshire, A., Stone, A., Wakelin, E., Jones, A. H., Wheeler, N. v., Brooks, W., & Bingham, P. A. (2023). From acrylates to silicones: A review of common optical fibre coatings used for normal to harsh environments. In *Progress in Organic Coatings* (Vol. 180). Elsevier B.V. https://doi.org/10.1016/j.porgcoat.2023.107557

Jiménez-García, J. C., Ruiz, A., Pacheco-Reyes, A., & Rivera, W. (2023). A Comprehensive Review of Organic Rankine Cycles. In *Processes* (Vol. 11, Issue 7). Multidisciplinary Digital Publishing Institute (MDPI). https://doi.org/10.3390/pr11071982

Jung, R. (2013). EGS — Goodbye or back to the future. In *ISRM International Conference for Effective and Sustainable Hydraulic Fracturing 2013*, 95–121. https://doi.org/10.5772/56458

Kersey, A, Marrone, M, and Davis, M. (1991). Polarization-Independent Interferometric Fiber Optic Sensor. In *Optical Fiber Communication* (Vol. 4). 1991 OSA Technical Digest Series (Optica Publishing Group).

Larson, K. (2019). Can you estimate Modulus from Durometer Hardness for silicones? *Dow White Paper*.

Lee, B. (2003). Review of the present status of optical fiber sensors. *Optical Fiber Technology*, *9*(2), 57–79. https://doi.org/10.1016/S1068-5200(02)00527-8

Lee, S. H., & Ghassemi, A. (2022). *Numerical Simulation of Fluid Circulation in Hydraulically Fractured Utah FORGE Wells*.

Moore, J., Mclennan, J., Allis, R., Pankow, K., Simmons, S., Podgorney, R., Wannamaker, P., Bartley, J., Jones, C., & Rickard, W. (2019). The Utah Frontier Observatory for Research in Geothermal Energy (FORGE): An International Laboratory for Enhanced Geothermal System Technology Development. In *PROCEEDINGS*.

Moore, J. (2020). Utah FORGE: Phase 3 Year 1 Annual Report. *Energy and Geoscience Institute at the University of Utah.* https://gdr.openei.org/submissions/1409.

Moss, R. J., & Moss, G. E. (1990). Handbook of Ground Water Development. *Roscoe Moss Company*.

Murdoch, L. C. (1995). Forms of hydraulic fractures created during a field test in overconsolidated glacial drift. In *Quarterly Journal of Engineering Geology* (Vol. 28), 23–35.

Murdoch, L. C., DeWolf, S., Germanovich, L. N., Moysey, S. M., Hanna, A. C., Roudini, S., & Moak, R. (2022). Using the Shallow Strain Tensor to Characterize a Deep Geologic Reservoir. In *ESS Open Archive*. https://essopenarchive.org/doi/full/10.1002/essoar.10511849.1

Murdoch, L. C., Freeman, C. E., Germanovich, L. N., Thrash, C., & Dewolf, S. (2015). Using in situ vertical displacements to characterize changes in moisture load. In *Water Resources Research* (Vol.51, Issue 8), 5998–6016. https://doi.org/10.1002/2015WR017335

Murdoch, L. C., Germanovich, L. N., DeWolf, S. J., Moysey, S. M. J., Hanna, A. C., Kim, S., & Duncan, R. G. (2020). Feasibility of using in situ deformation to monitor CO2 storage. In *International Journal of Greenhouse Gas Control* (Vol; 93). https://doi.org/10.1016/j.ijggc.2019.102853

Murdoch, L., Dewolf, S., Germanovich, L., Hanna, A., Moak, R., & Moysey, S. (2019). Characterizing and interpreting the in-situ strain tensor during CO2 injection. https://doi.org/10.2172/1529100.

Murdoch, L. C., Germanovich, L. N., Roudini, S., DeWolf, S. J., Hua, L., & Moak, R. W. (2021). A Type-Curve Approach for Evaluating Aquifer Properties by Interpreting Shallow Strain Measured During Well Tests. In *Water Resources Research* (Vol. 57, Issue 9). https://doi.org/10.1029/2021WR029613

Murdoch, L. C., Richardson, J. R., Tan, Q., Malin, S. C., & Fairbanks, C. (2006). Forms and sand transport in shallow hydraulic fractures in residual soil. In *Canadian Geotechnical Journal*, (Vol. 43, Issue 10), 1061–1073. https://doi.org/10.1139/T06-063

Norbeck, J. H., & Latimer, T. M. (2023). Commercial-Scale Demonstration of a First-of-a-Kind Enhanced Geothermal System.

Olasolo, P., Juárez, M. C., Morales, M. P., Damico, S., & Liarte, I. A. (2016). Enhanced geothermal systems (EGS): A review. In *Renewable and Sustainable Energy Reviews* (Vol. 56), 133–144. Elsevier Ltd. https://doi.org/10.1016/j.rser.2015.11.031

Podgorney, R., Finnila, A., Simmons, S., & McLennan, J. (2021). A reference thermal-hydrologic-mechanical native state model of the utah FORGE enhanced geothermal site. In *Energies*, (Vol. 14, Issue 16). https://doi.org/10.3390/en14164758.

Qi, H., Boyce, M. (2005). Stress-Strain behavior of thermoplastic polyurethanes. In *Mechanics of Materials,* (Vol. 37, Issue 8), 817-839. http://doi.org/10.1016/j.mechmat.2004.08.001.

Sheem, S. K. (1981). Optical fiber interferometers with [3×3] directional couplers: Analysis. In *Journal of Applied Physics* (Vol. 52, Issue 6), 3865–3872. https://doi.org/10.1063/1.329853.

Tester, J., Anderson, B., Batchelor, A., Blackwell, D., DiPippo, R., Drake, E., Garnish, J., Livesay, B., Moore, M., Nichols, K., Petty, S., Toksoz, M. N., & Veatch, R. J. (2006). The Future of Geothermal Energy: Impact of Enhanced Geothermal Systems (EGS) on the United States in the 21st Century. http://www1.eere.energy.gov/geothermal/egs_technology.html

Tester, J. W., Anderson, B. J., Batchelor, A. S., Blackwell, D. D., Dipippo, R., Drake, E. M., Garnish, J., Livesay, B., Moore, M. C., Nichols, K., Petty, S., Nafi Toksoz, M., Veatch, R. W., Baria, R., Augustine, C., Murphy, E., Negraru, P., & Richards, M. (2007). Impact of enhanced geothermal systems on US energy supply in the twenty-first century. In *Philosophical Transactions of the Royal Society A: Mathematical, Physical and Engineering Sciences* (Vol 365, Issue 1853), 1057–1094. https://doi.org/10.1098/rsta.2006.1964

Xing, P., Damjanac, B., Radakovic-Guzina, Z., Finnila, A., Podgorney, R., Moore, J., & Mclennan, J. (2021). Numerical Simulation of Injection Tests at Utah FORGE Site. In *PROCEEDINGS* (Vol. 46).

Zarrouk S., Moon H. (2014). Efficiency of geothermal power plants: A worldwide review. In *Geothermics* (Vol 51), 142-153. https://doi.org/10.1016/j.geothermics.2013.11.001

Zhai, Z., & Sharma, M. M. (2005). A New Approach to Modeling Hydraulic Fractures in Unconsolidated sands. In *SPE Annual Technical Conference and Exhibition.* https://doi.org/10.2118/96246-MS.

Zhang, H., Cong, B., Zhang, F., Qi, Y., & Hu, T. (2021). Simultaneous measurement of refractive index and temperature by Mach–Zehnder cascaded with FBG sensor based on multi-core microfiber. In *Optics Communications* (Vol. 493). https://doi.org/10.1016/j.optcom.2021.126985

Ziółkowski P., Hyrzyński R., Lemański M., Kraszewski B., Bykuć S., Głuch S., Sowiżdżał A., Pająk L., Wachowicz-Pyzik A., Badur J. (2021). Different design aspects of an Organic Rankine Cycle turbine for electricity production using a geothermal binary power plant. In *Energy Conversion and Management* (Vol. 246). https://doi.org/10.1016/j.enconman.2021.114672.

Zumberge M, Berger, J, Dzieciuch, M, and Parker, R. (2004). Resolving quadrature fringes in real time. In *Applied Optics* (Vol. 43, Issue 4), 771-775. https://doi.org/10.1364/AO.43.000771.

Zumberge, M. A., DeWolf, S., Wyatt, F. K., Agnew, D. C., Elliott, D., & Hatfield, W. (2013). Results from a borehole optical fiber interferometer for recording Earth strain. In *Fifth European Workshop on Optical Fibre Sensors, 8794,* 87940. https://doi.org/10.1117/12.2025896

APPENDIX

APPENDIX A: PYTHON CODE FOR LOADING TEST STUDY

```
import numpy as np
import matplotlib.pyplot as plt
from matplotlib.ticker import AutoMinorLocator

def getAndInterpData(file,time_interval,column_of_interest):
    data = np.loadtxt(file)
    t_given = data[:,0]
    sensor = data[:,column_of_interest]
    t = np.arange(np.min(t_given),np.max(t_given),time_interval)
    sig = np.interp(t,t_given,sensor)

    return t, sig

def getStencil(t,sig,startInd,endInd):
    stencil = sig[startInd:endInd]
    t_stencil = t[startInd:endInd]
    mean_stencil = np.mean(stencil)
    stencil = stencil - mean_stencil # delete baseline signal

    return t_stencil, stencil, mean_stencil

def getMatchSig(maxConvInd,ts,t,sig):
    si = maxConvInd
    ei = maxConvInd+len(ts)
    t_match = t[si:ei]
    match_sig = sig[si:ei]

    return t_match, match_sig


if __name__ == "__main__":
    filename = "Strain_825_828_unfinished.txt"
    #newStartingPoint = 47340 #index 45100/(new_dt*60*60)
    new_dt =  2.292e-6 #DAYS
    columnNumber = 1

    #LOAD AND INTERPOLATE THE DATA
    time,FBG = getAndInterpData(filename,new_dt,columnNumber)
    #time = time[newStartingPoint:]
    time = time - time[0]
    FBG = FBG#[newStartingPoint:]

    # ## Plot data
    # fig1 = plt.figure("Strain Data")
    # ax1 = fig1.add_subplot(111)
    # ax1.plot(time,FBG,'k',label= "FBG 1")
    # ##Format the graph area
    # ax1.set_xlabel("Time (days)", fontsize = 30)
    # ax1.set_ylabel ("Strain (\u03BC\u03B5)", fontsize = 30)
    # ax1.legend(bbox_to_anchor=(0.75, 1.15), loc='upper left', borderaxespad=0,fontsize=40,markerscale=5)
    # ax1.spines["left"].set_linewidth(3)
    # ax1.spines["bottom"].set_linewidth(3)
```

```
# ax1.spines["right"].set_linewidth(1.2)
# ax1.spines["top"].set_linewidth(1.2)
# ax1.set_xlim(xmin=0)
# ax1.tick_params(axis='both', which='major', labelsize=25, width = 2, length = 8)

# ax1.grid(which='major', color='grey', linewidth=1)
# ax1.minorticks_on()
# ax1.tick_params(which='minor', bottom=False, left=False)
# ax1.grid(which='minor', color='lightgrey', linestyle='--', linewidth=0.5)
# ax1.yaxis.set_minor_locator(AutoMinorLocator(2))
# ax1.xaxis.set_minor_locator(AutoMinorLocator(5))


## STENCIL
Stencil_file ='DATA_StencilFBG1_new.txt'
new_dt_2 = new_dt*24 #DO THE INTERPOLATION IN THE SAME UNITS AS INPUT FILE
ts,stencil = getAndInterpData(Stencil_file,new_dt_2,1)
ts = ts/24 #CONVERT BACK TO DAYS
avgStencil = np.mean(stencil)
stencil = stencil-avgStencil


## Plot stencil
# fig2 = plt.figure("Stencil")
# ax2 = fig2.add_subplot(111)
# indices = np.arange(0,len(ts),1)
# ax2.plot(indices,stencil,'slategrey',linewidth='3', label="FBG 1")
# ###Format the graph area
# ax2.set_xlabel("Indices", fontsize = 30)
# ax2.set_ylabel ("Strain (\u03BC\u03B5)", fontsize = 30)
# ax2.legend(bbox_to_anchor=(0.75, 1.15), loc='upper left', borderaxespad=0,fontsize=40,markerscale=5)
# ax2.spines["left"].set_linewidth(3)
# ax2.spines["bottom"].set_linewidth(3)
# ax2.spines["right"].set_linewidth(1.2)
# ax2.spines["top"].set_linewidth(1.2)
# ax2.set_xlim(xmin=0)
# ax2.tick_params(axis='both', which='major', labelsize=25, width = 2, length = 8)
# ax2.grid(which='major', color='grey', linewidth=1)
# ax2.minorticks_on()
# ax2.tick_params(which='minor', bottom=False, left=False)
# ax2.grid(which='minor', color='lightgrey', linestyle='--', linewidth=0.5)
# ax2.yaxis.set_minor_locator(AutoMinorLocator(2))
# ax2.xaxis.set_minor_locator(AutoMinorLocator(5))
# ax2.yaxis.set_major_locator(plt.MaxNLocator(4))

## CONVOLUTION
convData = np.convolve(FBG,stencil[::-1], mode='valid') #[::-1] mirrior it to cancel it out in the convolution

# ## Convolution plot reading
firstPeak_ind = 8772  ## TO CHANGE AT EACH DOC
indStep = 18600 #to jump to next match (approximate)
searchWidthInd = 3000 #10 min window #to help find the next match

nTrials = 48 #number of loading tests in the text file - VERIFY WITH DATA PLOT
#search loop willbug if nTrials does not match with actual number of loading tests
```

```
    search = np.arange(firstPeak_ind,firstPeak_ind+nTrials*indStep,indStep)  #define the search range in the
convolution
    peaks = np.zeros(nTrials) #create a spot to store the indexes of the convolution peaks

   #RANDOM PLOT TO ENSURE firstPeak_ind is corect.
    #Check the orange and dashed vertical lines in the next plot.
    #in the next plot the orange lines should be close to the peaks of the convolution^2

    # fig3 = plt.figure(12312)
    # ax3 = fig3.add_subplot(111)
    # ax3.plot(convData**2)

    #%%

    #FINDING INDICES OF THE MATCHES - finding all the indexes where the convolution is at max value aka
finding where the loading cycles are in the signal data
    # #MATCHING FILTERS (GOOGLE SIGNAL PROCESSING)

    for i in range(0,len(search)): #we defined search as a range in the convolution going from peaks to peaks

        startIndSearch = search[i]-searchWidthInd
        endIndSearch = search[i]+searchWidthInd

        if startIndSearch<0:
            startIndSearch = 0

        if endIndSearch>len(convData):
            endIndSearch = len(convData)

        peaks[i] = startIndSearch + np.argmax(convData[startIndSearch:endIndSearch]) #storing the x axis index value
(time) of the peaks detected

    #%%
    ##PLOT to EXPLAIN
    #convDataSame = np.convolve(FBG,stencil[::-1], mode='valid')
    fig4 = plt.figure("Plots to explain")
    ax = fig4.add_subplot(311)
    ax2 = fig4.add_subplot(312)
    ax3 = fig4.add_subplot(313,sharex=ax2)
    ax.plot(ts,stencil) # Stencil plot
    ax2.plot(time,FBG,'k',label= "FBG 1") # Data plot
    indexPoints = np.arange(0,len(convData),1)
    ax3.plot(indexPoints*new_dt,convData**2,'tab:blue') #Convolution plot
    #ax3.plot(time,np.log10(convDataSame**2))
    for i in range(0,len(peaks)):
        #tempAmp = convData[int(peaks[i]+len(stencil)/2)]**2
        ax3.plot([peaks[i]*new_dt,peaks[i]*new_dt],[0,6e9],'k--',linewidth=2) #peak found/selected
        ax3.plot([search[i]*new_dt,search[i]*new_dt],[0,6e9],'tab:orange') # starting point of search window
    ax3.set_xlim([0,3.5])
    ax3.set_ylim([0,5e8]) # Need to change y axis max value when change stencil/FBG

    ax3.set_xlabel("Time (days)", fontsize = 30)
    ax2.set_ylabel ("Strain (\u03BC\u03B5)", fontsize = 30)
    ax.set_ylabel ("Strain (\u03BC\u03B5)", fontsize = 30)
    ax2.legend(bbox_to_anchor=(0.75, 2.7), loc='upper left', borderaxespad=0,fontsize=40,markerscale=5)
    ax2.spines["left"].set_linewidth(3)
```

```
    ax2.spines["bottom"].set_linewidth(3)
    ax2.spines["right"].set_linewidth(1.2)
    ax2.spines["top"].set_linewidth(1.2)
    ax.spines["left"].set_linewidth(3)
    ax.spines["bottom"].set_linewidth(3)
    ax.spines["right"].set_linewidth(1.2)
    ax.spines["top"].set_linewidth(1.2)
    ax3.spines["left"].set_linewidth(3)
    ax3.spines["bottom"].set_linewidth(3)
    ax3.spines["right"].set_linewidth(1.2)
    ax3.spines["top"].set_linewidth(1.2)
    ax2.set_xlim(xmin=0)
    ax.set_xlim(xmin=0)
    ax.tick_params(axis='both', which='major', labelsize=25, width = 2, length = 8)
    ax2.tick_params(axis='both', which='major', labelsize=25, width = 2, length = 8)
    ax3.tick_params(axis='both', which='major', labelsize=25, width = 2, length = 8)

    ax.grid(which='major', color='grey', linewidth=1)
    ax.minorticks_on()
    ax.tick_params(which='minor', bottom=False, left=False)
    ax.grid(which='minor', color='lightgrey', linestyle='--', linewidth=0.5)
    ax.yaxis.set_minor_locator(AutoMinorLocator(2))
    ax.xaxis.set_minor_locator(AutoMinorLocator(5))
    ax.yaxis.set_major_locator(plt.MaxNLocator(4))
    ax2.grid(which='major', color='grey', linewidth=1)
    ax2.minorticks_on()
    ax2.tick_params(which='minor', bottom=False, left=False)
    ax2.grid(which='minor', color='lightgrey', linestyle='--', linewidth=0.5)
    ax2.yaxis.set_minor_locator(AutoMinorLocator(2))
    ax2.xaxis.set_minor_locator(AutoMinorLocator(5))
    ax2.yaxis.set_major_locator(plt.MaxNLocator(4))
    ax3.grid(which='major', color='grey', linewidth=1)
    ax3.minorticks_on()
    ax3.tick_params(which='minor', bottom=False, left=False)
    ax3.grid(which='minor', color='lightgrey', linestyle='--', linewidth=0.5)
    ax3.yaxis.set_minor_locator(AutoMinorLocator(2))
    ax3.xaxis.set_minor_locator(AutoMinorLocator(5))
    ax3.yaxis.set_major_locator(plt.MaxNLocator(4))

    #%%
    #NEGATIVE INDICES BASED ON THE STENCIL
    # pick = false, wont run, pick = True, will run
    ## To find the intervals for the averages, only need to run it ONCE
    pick = False
    if pick:
        convDataSame = np.convolve(FBG,stencil[::-1], mode='same')
        fig = plt.figure(3242342323432)
        fig.set_size_inches([25.64,  2.12])
        ax = fig.add_subplot(111)
        ax.plot(stencil)
        vals = plt.ginput(18,120)
        vals = np.round(vals).astype(int)
#%%
# Stencil files are all the same length so those intervals won't need to change

    # n_winA = [[29,57],[128,160],[234,258],[332,365],[436,462],[536,563],[636,666],
```

```
#          [735,763],[835,865]]
# p_winA = [[79,110],[179,216],[277,312],[379,414],[480,516],[581,612],[686,712],
#          [786,817],[883,919]]

# n_winB = [[937,965],[1038,1067],[1140,1169],[1239,1269],[1340,1369],[1442,1475],
#          [1543,1572],[1644,1671],[1743,1772]]
# p_winB = [[884,914],[985,1017],[1088,1120],[1188,1219],[1292,1321],[1391,1420],[1490,1522],
#           [1594,1624],[1693,1725]]

picksTrials_A = np.array([])
picksTrials_B = np.array([])
picksTrials_C = np.array([])
picksTrials_D = np.array([])

stdTrials_A = np.array([])
stdTrials_B = np.array([])
stdTrials_C = np.array([])
stdTrials_D = np.array([])


amplitudeA = np.array([]) # change in strain due to loading A  = amplitude created by loading
amplitudeB = np.array([]) # change in strain due to loading B

stdTrials_ampliA = np.array([])
stdTrials_ampliB = np.array([])

# Variables to do some back tracing.
time_of_matches = np.array([])
index_of_matches = np.array([])


fig5 = plt.figure(56165185616)
ax5 = fig5.add_subplot(111)

# Be careful of time units
for j in range(0,len(peaks)):

    maxInd = int(peaks[j]) #assuming valid
    t_match, match_sig = getMatchSig(maxInd,ts,time,FBG)

    ax5.plot(t_match-time[int(peaks[j])],match_sig,label=str(time[int(peaks[j])]))

    si = maxInd
    ei = maxInd+len(ts)

    fig6 = plt.figure(j)
    ax6 = fig6.add_subplot(111)
    ax6.plot(t_match,match_sig,'k',linewidth=2)
    ax6.plot(t_match,stencil+avgStencil,'k--',alpha=0.5)
    ax6.set_xlabel("Time (hours)", fontsize = 30)
    ax6.set_ylabel ("Strain (\u03BC\u03B5)", fontsize = 30)
    ax6.spines["left"].set_linewidth(3)
    ax6.spines["bottom"].set_linewidth(3)
    ax6.spines["right"].set_linewidth(1.2)
    ax6.spines["top"].set_linewidth(1.2)
    ax6.tick_params(axis='both', which='major', labelsize=25, width = 2, length = 8)
```

```
    ax6.grid(which='major', color='grey', linewidth=1)
    ax6.minorticks_on()
    ax6.tick_params(which='minor', bottom=False, left=False)
    ax6.grid(which='minor', color='lightgrey', linestyle='--', linewidth=0.5)
    ax6.yaxis.set_minor_locator(AutoMinorLocator(2))
    ax6.xaxis.set_minor_locator(AutoMinorLocator(5))


    for i in range(0,len(n_winA)):


        time_of_matches = np.append(time_of_matches,peaks[j]*new_dt)
        index_of_matches = np.append(index_of_matches,peaks[j])

        # getting the mean values of the change in strain due to loading (getting the mean amplitude value) for each
loading so 9 means per hour
        tempA = np.mean(match_sig[p_winA[i][0]:p_winA[i][1]]) #GREEN
        tempB = np.mean(match_sig[p_winB[i][0]:p_winB[i][1]])
        tempC = np.mean(match_sig[n_winA[i][0]:n_winA[i][1]])
        tempD =  np.mean(match_sig[n_winB[i][0]:n_winB[i][1]])

        # Change in strain means - 9 means per hour
        amplitudeA = np.append(amplitudeA,tempA - tempC)
        amplitudeB = np.append(amplitudeB,tempB - tempD)

        # SD of the mean amplitude
        # stdTrials_ampliA = np.append(stdTrials_ampliA, np.std(match_sig[p_winA[i][0]:p_winA[i][1]]-
match_sig[n_winA[i][0]:n_winA[i][1]]))
        # stdTrials_ampliB = np.append(stdTrials_ampliB, np.std(match_sig[p_winB[i][0]:p_winB[i][1]] -
match_sig[n_winB[i][0]:n_winB[i][1]]))

        # Means of the strain in each window picked
        picksTrials_A = np.append(picksTrials_A,tempA) #tempA = amplitude of p_winA
        picksTrials_B = np.append(picksTrials_B,tempB) #tempB = amplitude of p_winB
        picksTrials_C = np.append(picksTrials_C,tempC) #temp = amplitude of n_winA
        picksTrials_D = np.append(picksTrials_D,tempD) #tempB = amplitude of n_winB

        #SD of the means for each window picks
        stdTrials_A = np.append(stdTrials_A,np.std(match_sig[p_winA[i][0]:p_winA[i][1]]))
        stdTrials_B = np.append(stdTrials_B,np.std(match_sig[p_winB[i][0]:p_winB[i][1]]))
        stdTrials_C = np.append(stdTrials_C,np.std(match_sig[n_winA[i][0]:n_winA[i][1]]))
        stdTrials_D = np.append(stdTrials_D,np.std(match_sig[n_winB[i][0]:n_winB[i][1]]))


        ax6.plot([t_match[p_winA[i][0]],t_match[p_winA[i][1]]],[tempA,tempA],'tab:green',linewidth=4)
        ax6.plot([t_match[n_winA[i][0]],t_match[n_winA[i][1]]],[tempC,tempC],'tab:orange',linewidth=4)
        ax6.plot([t_match[p_winB[i][0]],t_match[p_winB[i][1]]],[tempB,tempB],'tab:red',linewidth=4)
        ax6.plot([t_match[n_winB[i][0]],t_match[n_winB[i][1]]],[tempD,tempD],'tab:cyan',linewidth=4)


  ax5.legend()
  #WRITE YOUR FILES

  dat2write = np.column_stack([index_of_matches,time_of_matches,
                      amplitudeA,amplitudeB,#stdTrials_ampliA,stdTrials_ampliB
                      picksTrials_A,stdTrials_A,
```

```
                    picksTrials_B,stdTrials_B,
                    picksTrials_C,stdTrials_C,
                    picksTrials_D,stdTrials_D
                    ])

   np.savetxt('Averages_and_sd_FBG_perloadapplied',dat2write,fmt='%15.5f',header = "Index of matches / Time of matches / A mean / B mean")

#%%
## Cell to average all means per load so only get 1 mean per hour and sd
## Cell to average mean per hour to mean per 6h and calculate standard deviation of that

data = np.loadtxt('Averages_and_sd_FBG_perloadapplied') # insert name of text file

index = data[:,0]
meanA = data[:,2]
meanB = data[:,3]

avgA = np.array([])
avgB = np.array([])
stdevA = np.array([])
stdevB = np.array([])


avgA = np.mean(meanA.reshape(-1,9),axis=1)
avgB = np.mean(meanB.reshape(-1,9),axis=1)
stdevA = np.std(meanA.reshape(-1,9),axis=1)
stdevB = np.std(meanB.reshape(-1,9),axis=1)
time = np.arange(649,697,1)
doc_creation = np.column_stack([time,avgA,stdevA,avgB,stdevB])
np.savetxt('Averages_sd_230FBG1_825_828',doc_creation,fmt='%15.5f', header = 'Time (h) / A average / A stdev / B average / B stdev')

APPENDIX B: PYTHON CODE FOR PLOTTING DATA
import numpy as np
import matplotlib.pyplot as plt
import pandas as pd
from matplotlib.ticker import AutoMinorLocator

#%% LOOKING AT THE STRAIN RAW DATA

'Strain Data'

data = np.loadtxt('Strain_821_825.txt') # insert name of text file

time = data[:,0]-data[0,0]
FBG1 = data[:,1]#(data[:,0]-data[0,0])*24   #
FBG2 = data[:,2]
FBG3 = data[:,3]
FBG4 = data[:,4]
#
# Strain_milestone = np.column_stack([time,FBG1,FBG2,FBG3,FBG4])
# np.savetxt('DATA_StencilFBG1_flatAloading1.txt',Strain_milestone,fmt='%15.10f')


# ###Plot the data as is
```

```
fig = plt.figure('Raw data plot')
ax = fig.add_subplot(111)
# sensor_1 = ax.scatter(time,FBG1,s=30,marker='+',color='black',label="FBG 1 (axial)")
# sensor_2 =ax.scatter(time,FBG2,s=30,marker='+',color='deepskyblue',label="FBG 2 (axial)")
# sensor_3 =ax.scatter(time,FBG3,s=30,marker='+',color='limegreen',label="FBG 3 (axial)")
# sensor_4 =ax.scatter(time,FBG4,s=30,marker='+',color='orange',label="FBG 4 (circumferential)")
sensor_1 = ax.plot(time,FBG1,color='black',label="FBG 1 (axial)")
sensor_2 =ax.plot(time,FBG2,color='deepskyblue',label="FBG 2 (axial)")
sensor_3 =ax.plot(time,FBG3,color='limegreen',label="FBG 3 (axial)")
sensor_4 =ax.plot(time,FBG4,color='orange',label="FBG 4 (circumferential)")
# ###Format the graph area
ax.set_xlabel("Time (days)", fontsize = 30)
ax.set_ylabel ("Strain (\u03BC\u03B5)", fontsize = 30)
#ax.set_title ("Time series of the raw data", fontsize = 10)
ax.legend(bbox_to_anchor=(0.70, 0.55), loc='lower left', borderaxespad=0,fontsize=20,markerscale=5)
ax.spines["left"].set_linewidth(3)
ax.spines["bottom"].set_linewidth(3)
ax.spines["right"].set_linewidth(1.2)
ax.spines["top"].set_linewidth(1.2)
#ax.set_xlim(xmin=0)
#ax.set_ylim(ymin=0)
ax.set_xlim(0,35)
#ax.set_ylim(3000,4200)
ax.tick_params(axis='both', which='major', labelsize=25, width = 2, length = 8)

ax.grid(which='major', color='grey', linewidth=1)
ax.minorticks_on()
ax.tick_params(which='minor', bottom=False, left=False)
ax.grid(which='minor', color='lightgrey', linestyle='--', linewidth=0.5)
ax.yaxis.set_minor_locator(AutoMinorLocator(2))
ax.xaxis.set_minor_locator(AutoMinorLocator(5))


# ###Plot loading cycles
# fig2 = plt.figure('Zoom in on loading cycles')
# ax1 = fig2.add_subplot(221)
# ax2 = fig2.add_subplot(222)
# ax3 = fig2.add_subplot(223)
# ax4 = fig2.add_subplot(224)

# sensor_1 = ax1.scatter(time,FBG1,s=30,marker='+',color='black',label="FBG 1")
# sensor_2 =ax2.scatter(time,FBG2,s=30,marker='+',color='deepskyblue',label="FBG 2")
# sensor_3 =ax3.scatter(time,FBG3,s=30,marker='+',color='limegreen',label="FBG 3")
# sensor_4 =ax4.scatter(time,FBG4,s=30,marker='+',color='orange',label="FBG 4 ")

# # # ##Format the graph area
# ax1.set_ylabel ("Strain (\u03BC\u03B5)", fontsize = 30)
# #ax1.set_title ("Temperature vs Strain measured by FBG1", fontsize = 10)

# ax1.spines["left"].set_linewidth(3)
# ax1.spines["bottom"].set_linewidth(3)
# ax1.spines["right"].set_linewidth(1.2)
# ax1.spines["top"].set_linewidth(1.2)

# ax1.tick_params(axis='both', which='major', labelsize=20, width = 2, length = 8)
# ax1.grid(which='major', color='grey', linewidth=1)
```

```
# ax1.minorticks_on()
# ax1.tick_params(which='minor', bottom=False, left=False)
# ax1.grid(which='minor', color='lightgrey', linestyle='--', linewidth=0.5)
# #ax1.set_ylim(ymin=0)
# ax1.set_xlim(0,0.14)
# # ax1.set_ylim(ymin=-25)
# #ytick_loc1 = [5,0,-5,-10,-15]
# #ax1.set_yticks(ytick_loc1)
# ax1.yaxis.set_minor_locator(AutoMinorLocator(2))
# ax1.xaxis.set_minor_locator(AutoMinorLocator(2))

# #ax2.set_title ("Temperature vs Strain measured by FBG2", fontsize = 10)
# ax2.spines["left"].set_linewidth(3)
# ax2.spines["bottom"].set_linewidth(3)
# ax2.spines["right"].set_linewidth(1.2)
# ax2.spines["top"].set_linewidth(1.2)

# ax2.tick_params(axis='both', which='major', labelsize=20, width = 2, length = 8)
# ax2.grid(which='major', color='grey', linewidth=1)
# ax2.minorticks_on()
# ax2.tick_params(which='minor', bottom=False, left=False)
# ax2.grid(which='minor', color='lightgrey', linestyle='--', linewidth=0.5)
# #ytick_loc2 = [25,15,5,0,-5,-15,-25]
# #ax2.set_yticks(ytick_loc2)
# #ax2.set_ylim(ymin=0)
# # ax2.set_ylim(ymin=-15)
# ax2.set_xlim(0,0.14)
# ax2.yaxis.set_minor_locator(AutoMinorLocator(2))
# ax2.xaxis.set_minor_locator(AutoMinorLocator(2))

# ax3.set_xlabel("Temperature (\u00B0C)", fontsize = 30)
# ax3.set_ylabel ("Strain (\u03BC\u03B5)", fontsize = 30)
# #ax3.set_title ("Temperature vs Strain measured by FBG3", fontsize = 10)
# ax3.spines["left"].set_linewidth(3)
# ax3.spines["bottom"].set_linewidth(3)
# ax3.spines["right"].set_linewidth(1.2)
# ax3.spines["top"].set_linewidth(1.2)
# ax3.tick_params(axis='both', which='major', labelsize=20, width = 2, length = 8)

# ax3.grid(which='major', color='grey', linewidth=1)
# ax3.minorticks_on()
# ax3.tick_params(which='minor', bottom=False, left=False)
# ax3.grid(which='minor', color='lightgrey', linestyle='--', linewidth=0.5)
# #ax3.set_yticks(ytick_loc2)
# #ax3.set_ylim(ymin=0)
# ax3.set_xlim(0,0.14)
# # ax3.set_ylim(ymax=25)
# ax3.yaxis.set_minor_locator(AutoMinorLocator(2))
# ax3.xaxis.set_minor_locator(AutoMinorLocator(2))


# ax4.set_xlabel("Temperature (\u00B0C)", fontsize = 30)
# #ax4.set_title ("Temperature vs Strain measured by FBG4", fontsize = 10)
# ax4.spines["left"].set_linewidth(3)
# ax4.spines["bottom"].set_linewidth(3)
# ax4.spines["right"].set_linewidth(1.2)
```

```
# ax4.spines["top"].set_linewidth(1.2)
# ax4.tick_params(axis='both', which='major', labelsize=20, width = 2, length = 8)

# ax4.grid(which='major', color='grey', linewidth=1)
# ax4.minorticks_on()
# ax4.tick_params(which='minor', bottom=False, left=False)
# ax4.grid(which='minor', color='lightgrey', linestyle='--', linewidth=0.5)
# #ax4.set_yticks(ytick_loc1)
# #ax4.set_ylim(ymin=0)
# # ax4.set_ylim(ymin=-22)
# ax4.set_xlim(0,0.14)
# ax4.yaxis.set_minor_locator(AutoMinorLocator(2))
# ax4.xaxis.set_minor_locator(AutoMinorLocator(2))

#%% LOOKING AT THE TEMPERATURE RAW DATA

'Temperature data'

temperature_data = np.loadtxt('DATA_temp_724to828.txt') # insert name of text file

temptime = (temperature_data[:,0]-temperature_data[0,0]) #(data[:,0]-data[0,0])*24
tempsensor1 = temperature_data[:,1]
tempsensor2 = temperature_data[:,2]
tempsensor3 = temperature_data[:,3]
# tempsensor4 = temperature_data[:,4]


##Plot the data
fig1 = plt.figure('Raw temperature data plot')
axtemp = fig1.add_subplot(111)
# sensor_1 = axtemp.scatter(temptime,tempsensor1,s=30,marker='o',color='black',label="Sensor 3")
# sensor_2 =axtemp.scatter(temptime,tempsensor2,s=30,marker='o',color='deepskyblue',label="Sensor 2")
# sensor_3 =axtemp.scatter(temptime,tempsensor3,s=30,marker='o',color='limegreen',label="Sensor 1")
# sensor_4 =axtemp.scatter(temptime/3600,tempsensor4,s=10,marker='+',color='orange',label="Sensor 4")

sensor_1 = axtemp.plot(temptime,tempsensor1,color='black',label="Sensor 3")
sensor_2 =axtemp.plot(temptime,tempsensor2,color='deepskyblue',label="Sensor 2")
sensor_3 =axtemp.plot(temptime,tempsensor3,color='limegreen',label="Sensor 1")

##Format the graph area
axtemp.set_xlabel("Time (days)", fontsize = 30)
axtemp.set_ylabel ("Temperature (\u00B0C)", fontsize = 30)
#axtemp.set_title ("Time series of the raw data", fontsize = 10)
axtemp.legend(bbox_to_anchor=(0.75, 0.1), loc='lower left', borderaxespad=0,fontsize=40,markerscale=5)
axtemp.spines["left"].set_linewidth(3)
axtemp.spines["bottom"].set_linewidth(3)
axtemp.spines["right"].set_linewidth(1.2)
axtemp.spines["top"].set_linewidth(1.2)
axtemp.set_xlim(xmin=0)
axtemp.set_xlim(xmax=34)
axtemp.tick_params(axis='both', which='major', labelsize=25, width = 2, length = 8)

axtemp.grid(which='major', color='grey', linewidth=1)
axtemp.minorticks_on()
axtemp.tick_params(which='minor', bottom=False, left=False)
axtemp.grid(which='minor', color='lightgrey', linestyle='--', linewidth=0.5)
```

```
axtemp.yaxis.set_minor_locator(AutoMinorLocator(2))
axtemp.xaxis.set_minor_locator(AutoMinorLocator(5))
```